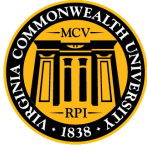

Virginia Commonwealth University
VCU Scholars Compass

Theses and Dissertations Graduate School

2022

LOW INSERTION-LOSS NANOPHOTONIC MODULATORS THROUGH EPSILON-NEAR-ZERO MATERIAL-BASED PLASMON-ASSISTED APPROACH FOR INTEGRATED PHOTONICS

Mohammad Ariful Hoque Sojib
Virginia Commonwealth University

Follow this and additional works at: https://scholarscompass.vcu.edu/etd

Part of the Electromagnetics and Photonics Commons, Electronic Devices and Semiconductor Manufacturing Commons, and the Other Electrical and Computer Engineering Commons

© The Author

Downloaded from
https://scholarscompass.vcu.edu/etd/7141

This Thesis is brought to you for free and open access by the Graduate School at VCU Scholars Compass. It has been accepted for inclusion in Theses and Dissertations by an authorized administrator of VCU Scholars Compass. For more information, please contact libcompass@vcu.edu.

LOW INSERTION-LOSS NANOPHOTONIC MODULATORS THROUGH EPSILON-NEAR-ZERO MATERIAL-BASED PLASMON-ASSISTED APPROACH FOR INTEGRATED PHOTONICS

A Thesis submitted in partial fulfillment of the requirements for the degree of Master of Science at Virginia Commonwealth University

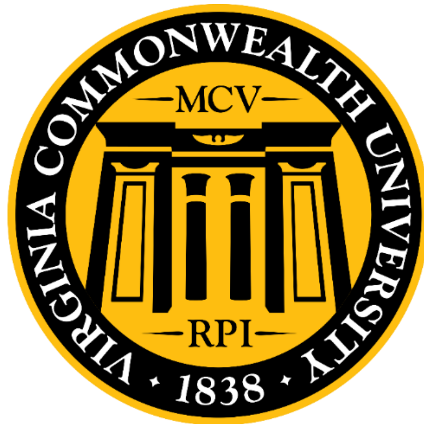

By

Mohammad Ariful Hoque Sojib

Bachelor of Science in Electrical and Electronic Engineering

Chittagong University of Engineering and Technology

Chittagong, Bangladesh

Supervisor: Dr. Nathaniel Kinsey

Associate Professor

Department of Electrical and Computer Engineering

Virginia Commonwealth University

Richmond, Virginia

December 2022

ACKNOWLEDGMENTS

I am grateful to the almighty Allah for allowing me to pursue higher study. I am grateful to Dr. Nathaniel Kinsey for his support, guidance, constructive critiques, and positivity that helped me gain skills to achieve the research goals. I would like to thank Dr. Vitaliy Avrutin, Dhruv Fomra, and Sampritty Saha for having fruitful discussions on research topics. I would like to thank the rest of the team for all kinds of input throughout this research journey. I am grateful and indebted to my family especially, to my mother for her endless support, encouragement, and positivity in day-to-day life during my graduate study while living far away from home. I would also like to thank the following funding agencies for all of their support:

National Science Foundation (1808928, ECCS EPMD Program, USA)

Air force Office of Scientific Research, USA (FA9550-1-18-0151)

Table of Contents

Table of Contents ..... **iii**

List of Figures ..... **vi**

List of Tables ..... **xi**

Abstract ..... **xii**

1. Introduction **1**

2. Background **4**

2.1. E-K Diagram 4

2.2. Density of States and Fermi Function 8

2.3. Doping of Semiconductor 11

2.4. Metal-Oxide/Insulator-Semiconductor (MOS/MIS) 13

2.5. Analysis of Carrier transport in an MIS gate structure 17

2.6. Lorentz Oscillator Model 22

2.7. Epsilon Near Zero Materials for photonic applications 25

2.8. Methods of Electro-optic/absorption Modulator 28

2.8.1. Pockels and Kerr Effect 29

2.8.2. Plasma Dispersion Effect 32

2.9. Performance Metrics 35

2.9.1. Extinction Ratio 35

2.9.2. Insertion Loss 35

2.9.3. Electro-Optic and Optical Bandwidth 36

2.9.4. Energy Consumption 37

2.9.5. Footprint 38

2.10. Mode Analysis of Rib and Slot Waveguide for EAM 39

3. Introduction and Optimization of EAM **44**

3.1 Introduction to Modulator Design 44

3.2: MOS Optimization 45

3.2.1 Selection of Oxide 46

3.2.1. Optimization of Carrier Concentration in ITO 48

3.2.2. Results and Discussion 50
3.3. Optimization of Electro-Absorption Modulator.. 52
3.3.1. 2D Carrier Distribution in MOS 53
3.3.2. Performance Analysis of a 2D Cross-Sectional EAM.. 54
3.3.3. Introduction to Surface-to-Volume Ratio 56
3.3.4. Performance Comparison between Rib and Slot Configuration 57
3.3.5. Performance of Multi-Slot Configuration 61
3.3.6. Tradeoffs associated with Surface-to-Volume Ratio.. 62
4. Material Growth and Characterization for the Optimized EAM 65
4.1. Basics of Atomic Layer Deposition 65
4.2. Basics of Spectroscopic Ellipsometry 69
4.2.1. Cauchy Model for Transparent Film 72
4.2.2. B-spline Model for Metals.. 73
4.3. Sample Preparation for Material Growth 75
4.4. ALD Growth of HfO_2 and HfAlO alloy 75
4.5. ALD Growth of Al-doped ZnO.. 79
4.6. ALD Growth of TiN for Metallic Contact 85
4.7. p-type Doping of Si 91
Conclusion and Future Prospect: 93
Appendices 95
Appendix I:... 95
Appendix II: 97
Appendix III: 99
Appendix IV:... 101
References 102
Publications 118
Journal 118
Conferences... 118
Patent 119
List of Major Abbreviations 120

List of Variables and Constants **121**
Vitae **122**

List of Figures

Fig. 2.1: (a) The overlapping radial probability function of two electrons in two adjacent hydrogen atoms. (b) Splitting of discrete energy level for state $n = 1$ (c) Splitting of discrete energy levels for a crystal with more than one electronic orbit. (d) interaction of 3s and 3p state give rise to hybridized sp^3 electronic states in Si [24]. 4

Fig. 2.2: A one-dimensional arrangement of atoms within a crystal is represented by a one-dimensional periodic potential function in a Kronig-Penny model [24]. 6

Fig. 2.3: (a) The plot showing the *f(αa)* (solid blue line) and the shaded region indicating the allowed values of *αa* for real values of wave number *k*. (b) *E* vs *k* diagram derived from (a) showing allowed states and forbidden energy gap within a crystal [24]. 7

Fig. 2.4: (a) The E vs k diagram for a reduced k space [24]. (b) Simple representation of CB, VB, and E_g. 8

Fig. 2.5: Schematic band diagram, Density of States, Fermi-Dirac distribution, and Carrier concentration for (a) intrinsic, (b) n-type, and (c) p-type semiconductors at thermal equilibrium [27]. 9

Fig. 2.6: (a) 2D representation of single crystal intrinsic Si atoms, (b) Si doped with boron atom, and (c) corresponding ionization of boron atom and the creation of hole within the crystal [24] 11

Fig. 2.7: A typical Metal-Insulator-Semiconductor (MIS) gate structure (a) schematic showing individual components and (b) equivalent energy band diagram [27]. 13

Fig. 2.8: Energy band Diagrams of ideal MIS structure depicting three different scenarios (a) Accumulation, (b) Depletion, and (c) Inversion [27] 14

Fig. 2.9: Block charge diagram of a MIS gate with *p*-type semiconductor for the simple depiction of three conditions namely (a) Accumulation, (b) Depletion, and (c) Inversion [26] 15

Fig. 2.10: Carrier density distribution the near the interface between SiO_2/Si in a perpendicular direction according to (a) Classical DD model, (b) Quantum correction included DG method [35] 21

Fig. 2.11: Electron density profile within a Si inversion layer incorporated in a MOS structure derived from SP and DG method at two different voltages [32] 21

Fig. 2.12: Complex relative dielectric constant and the corresponding real and imaginary part of refractive index derived for a Lorentz oscillator [36]. 24
Fig. 2.13: (a) Real and (b) imaginary part of the permittivity of three ENZ materials................ 27
Fig. 2.14: Schematic showing basic design flow of implanting an EOM [49]. 28
Fig. 2.15: (a) Application of a voltage across the optic axis (n_e) of a $LiNbO_3$ crystal (b). Schematic showing integrated phase modulator [50]. 30
Fig. 2.16: (a) A MZI intensity modulator with the inclusion of phase modulator in one of the arms (b) Change in the transmission upon application of an applied voltage shown in (a). The voltage V_π required for a π phase shift and thus switching normalized transmission between 0 and 1 is shown [50]. 31
Fig. 2.17: Cross-sectional image of typical plasma dispersion-based Si optical modulators applying three different schemes such as (a) carrier accumulation using MOS configuration (b) carrier injection using p-i-n configuration, (c) carrier depletion using a lightly doped p-n junction [58]. 32
Fig. 2.18: Schematics for the illustration of (a) light propagates from one medium to another medium with distinct refractive indices. (b) Critical angle at the interface that causes light to traverse along the interface with $\theta_2 = 90^0$. (c) Total Internal Reflection of light for $\theta_1 > \theta_C$........ 39
Fig. 2.19: Schematic showing two types of waveguide configuration (a) Ridge and (b) Rib [2]. 40
Fig. 2.20: Schematic showing conventional slot and strip loaded Si waveguide. A conventional strip waveguide configuration is also shown to point out geometrical differences. The respective refractive indices of constituent materials are also shown [70]. 41
Fig. 2.21: FEM analysis to find TE and TM modes in strip and slot waveguides with operating wavelength of 1.55 µm, substrate and cladding refractive indices of 3.48 and 1.44 respectively [70]. 43
Fig. 3.1. Schematic of (a) Rib and (b) Slot configurations of EAM. For multi-slots N_{Pillar} is the number of Si pillars in the middle of two Si rails. $N_{Pillar} = 0$ corresponds to single slot configuration while $N_{Pillar} = 1,2,3$ correspond to 2, 3 and 4-slot configurations of EAM [65,74]......................... 44

Fig. 3.2. (a) 1D schematic of the capacitor structure [65] (b) Comparison between break down voltage (red bar) and the voltage across the oxides (green bar) to achieve ENZ condition for three different oxides. 47
Fig. 3.3. (a) Distribution of gate voltage across various section of capacitor structure. Voltage drops across Oxide, ITO, and p-type Si. (b) Energy band diagram of the optimized MOS structure at a gate voltage of -4.7 V. The oxide has been defined as a "charge conservation" layer [65]. . 49
Fig. 3.4. (a-b) Electron and Hole concentration within ITO and p-type Si as a function of gate voltage. The bulk hole carrier concentration within p-type Si is $1\times10^{17}cm^{-3}$ (c-d) Real and Imaginary part of permittivity within ITO as a function of gate voltage and ITO thickness [65].51
Fig. 3.5. Schematic of cross-sectional view of rib-based Si waveguide with MOS structure (a) in the X-Y plane to determine 2D carrier distribution. The false colors indicating individual layers are marked in fig. (b) in the X-Z plane to evaluate performance metrics and FOM. 52
Fig. 3.6. 2D carrier distribution in the optimized ITO/HfO_2/p-Si MOS configuration. The corresponding color bars (unit in cm^{-3}) and the orientation of the MOS are also shown. 53
Fig. 3.7. Cross sectional analysis of the EAM with *w* = 240 nm (a) The X-component of the EM filed propagating in the Z direction. The air and PML layer have been indicted. (b) Time average power flow into the Z direction at 5V applied voltage. 54
Fig. 3.8. Cross sectional analysis of the EAM with wide range of waveguide width (a) FOM as a function of waveguide width. (b) Device length and Insertion loss showing relatively poor performance of rib-based configuration... 56
Fig. 3.9. ER (dB/µm) (black) and IL for 6dB modulation (red) for (a) rib and (b) single slot configuration respectively. The slot width is 40 nm [65]. 58
Fig. 3.10. ER (dB/µm) and IL (dB/µm) for single slot configuration as a function of slot width shows increasing loss with increasing slot width containing ITO. The rail width is fixed and equal to 200 nm for single slot configuration [65]. 59
Fig. 3.11. (a) Comparison of multi-slots configurations with respect to ER (dB/µm) and 6 dB IL (b) FOM (ER/IL) as a function of the total ENZ surface area to TCO volume ratio shows improved performance from single to multi-slot configurations [65].. 61

Fig. 3.12. (a) The speed and energy consumption of the slot waveguide designs, illustrating a trade-off in terms of device operation speed and energy consumption. (b) ER and IL and (c) Speed and Energy consumption for 1-slot configuration respectively as a function of the top ITO contact thickness, outlining an approach to mitigate these issues if constraints on IL and driving voltage are relaxed. The 15 nm device was biased at -4.7 V while the other structures were biased at -5.0 V, required to achieve a comparable peak accumulation density within the slot region. The slot width remains same for all cases [65]. 63
Fig. 4.1: (a) Schematic showing cyclic nature of ALD growth process involving two precursors "A" and "B" for the growth of the film "A-B". (b) Cross-sectional SEM image showing excellent conformal growth of Al_2O_3 on a high-aspect ratio Si trench [89]. 66
Fig. 4.2: (a) Growth of Al_2O_3 using ALD with TMA and H_2O as the precursors for Al and O_2 respectively analogous to "A" and "B" in fig. 4.1 (a) [92] (b) A so-called temperature window for an ALD process [93]. 68
Fig. 4.3: (a) Schematic depicting ellipsometry measurement technique at oblique incident. The polarization of incident beams changes upon the reflection off the sample surfaces/interfaces. (b) Schematic showing multiple reflections and refractions at the interfaces [95]. 70
Fig. 4.4: A sample ellipsometry measurement at oblique incidences showing data in terms of Ψ and Δ [95]. 71
Fig. 4.5: Basic flow diagram for spectroscopic ellipsometry for the extraction of physical parameters [95] 72
Fig. 4.6: (a) Formation of a B-spline curve with basis functions through degree 0 to 3. (b) Implementation of Kramers-Kronig consistency in B-spline by imposing positive value of controlling points for a smooth transition near the band edge absorption of a material [97]. 74
Fig. 4.7: Schematic showing the precursor pulses and the corresponding periods of the individual section of the ALD growth process for HfAlO. 77
Fig. 4.8: (a) SE data in terms of Ψ and Δ for the sample S3 at a 50^0 angle of incidence. The respective data from the model is also shown (b) Refractive index (real part, n only) of grown samples showing the decreasing trend of n with increasing trend of Al content. The imaginary part of the refractive indices (*k*) for each oxide is close to zero (not shown in the figure). 78

Fig. 4.9: Schematic showing the precursor pulses and the corresponding periods of the individual section of the ALD growth process for Al-ZnO. 80

Fig. 4.10: For the AZO films grown on Si substrate (a) SE reflection data at oblique incidence for the sample S2 (b) Optical constants of the films derived from modeling the film as Gen-Osc layer. The black dotted line points out the ENZ at ~1550 nm for the sample S2. 82

Fig. 4.11: For the AZO films grown on SiO_2 substrate (a) SE measurement data acquired at an oblique incidence of 60^0 (b) Optical constants of the films derived from modeling the film as Gen-Osc layer. The black dotted line points out the ENZ at ~1472 nm. 83

Fig. 4.12: For the AZO films grown on SiO_2 substrate (a-c) Surface plots showing the uniformity of the film in terms of thickness, resistivity, and scattering time respectively. 84

Fig. 4.13: Schematic representation of a single cycle for the ALD growth of TiN. 87

Fig. 4.14: For the films grown in the fourth trial (a) SE reflection data (b) Transmission intensity for films on Sapphire and glass (c) Derived permittivity from the B-spline model. (d) FOM showing the peak at ~2.4 for the film grown on c-plane Sapphire substrate. 88

Fig. 4.15: For the final grown optically thick TiN film (a) Derived permittivities from the B-spline model. (b) FOM showing the peak at ~2.51 for the film grown on c-plane Sapphire substrate... 90

Fig. S1. (a) Effective mode index and the Ex-component of electric field at 0V. The dotted closed line highlights interfaces of ITO/HfO_2/p-Si to show (b) Field confinement at the interface of ITO/HfO_2 at -4.7V. (c) $|E_x|$ at 0V and -4.7V [65]. 96

Fig. S2. Verification of the DG effective mass of electrons in ITO by comparing electron concentrations derived from DG and SP method for two different voltages. The density gradient effective mass has been set as $m_0/3$ where m_0 is the rest mass of free electron. For SP method, the effective mass of electron in ITO has been set as $0.35m_0$ [65]. 98

List of Tables

Table 2.1. Performance summary of the state-of-the-art modulators reported in the literature ... 38

Table 4.1: Set temperatures for the growth of HfO_2 and HfAlO alloys 77

Table 4.2: Summary of the parameters applied to oxide growth processes and the derived values from the Cauchy model... 78

Table 4.3: Set temperatures for the ALD growth of Al-doped ZnO... 81

Table 4.4: Set temperatures for the ALD growth of TiN.. 87

Table 4.5: Set temperatures for chamber baking 87

Table 4.6: Summary of the results from the B-spline model.. 89

Table 4.7: Sample preparation for the doping process 91

Table 4.8: Doping processes in the furnace.. 92

Table S1. Material parameters for the semiconductor and optical analysis 95

Table S2. Performance summary and comparison of the proposed EAM with the state-of-the-art modulators reported in the literature... 101

Abstract

LOW INSERTION-LOSS NANOPHOTONIC MODULATORS THROUGH EPSILON-NEAR-ZERO MATERIAL-BASED PLASMON-ASSISTED APPROACH FOR INTEGRATED PHOTONICS

By Mohammad Ariful Hoque Sojib

A Thesis submitted in partial fulfillment of the requirements for the degree of Master of Science at Virginia Commonwealth University

Virginia Commonwealth University, 2022.

Major Director: Nathaniel Kinsey, Ph.D.
Associate Professor
Department of Electrical and Computer Engineering

Electro-optic/absorption Modulators (EOM/EAMs) encode high-frequency electrical signals into optical signals. With the requirement of large packing density, device miniaturization is possible by confining light in a sub-wavelength dimension by utilizing the plasmonic phenomenon. In plasmon, energy gets transferred from light to the form of oscillation of free electrons on a surface of a metal at an interface between the metal and a dielectric. Plasmonic provides increased light-matter interaction (LMI) and thus making the light more sensitive to local refractive index change. Plasmonic-based integrated nanophotonic modulators use conventional metals on top or in the vicinity of the active modulating region that facilitates hybrid plasmonic photonic mode. This is beneficial to achieve a relatively large extinction ratio (ER) but the light has to constantly experience the lossy nature of plasmon, even when no modulation is needed, coming from the

ohmic loss due to the oscillation of free electrons on the surface of the metal. This incurs an undesirable off-state loss also known as insertion loss (IL). Despite promising features in terms of size, bandwidths, speed, and complementary metal oxide semiconductor (CMOS) compatibility, they have this one key limiting factor of large IL which limits their practical potential. To combat this, this research aims to reduce IL while achieving an appreciable 6 dB ER by utilizing an epsilon-near-zero (ENZ) enhanced plasmon-assisted approach. ENZ is the phenomenon when the real part of the permittivity becomes close to zero facilitating electromagnetic field confinement meeting the requirement of the boundary condition that is the continuity of the normal component of the electric field displacement. To reduce IL we replace the metal typically found in EAM designs reported in the literature from the top or in the vicinity of modulating region by indium doped tin oxide (ITO), a material from the transparent conducting oxide (TCO) family. ITO has been incorporated into a metal-oxide-semiconductor (MOS) and it functions both as a gate electrode and the tunable material necessary for biasing and light modulation respectively. The research studies rib, single, and multi-slot configurations of EAM design and introduce surface-to-volume ratio (SVR) as a figure of merit (FOM) to evaluate the corresponding performance metrics. Through the lens of SVR, this research reports a 4-slot-based EAM with an ER of 2.62 dB/μm and IL of 0.3 dB/μm operating at ~1 GHz and a single slot design with ER of 1.4 dB/μm and IL of 0.25 dB/μm operating at ~20 GHz. Furthermore, the analysis imposes realistic fabrication constraints, and material properties, and illustrates trade-offs in the performance that must be carefully optimized for a given scenario. Besides the research investigates optical and electrical properties of constituent materials through techniques such as atomic layer deposition (ALD) for depositing

thin films, spectroscopic ellipsometry (SE), and Hall measurements for optical and electrical characterization respectively.

1. Introduction

The invention of semiconductor technologies and optical communication through optical fiber has revolutionized our capability and the speed at which we process information. This has been possible mainly due to the scaling of semiconductor components (*e.g., scaling of transistors down to 35 nm channel length*) following Moor's law. However further scaling of such components put significant issues to solve such as short-channel effects, gate leakage current, and increasing power density [1]. Moreover, data consumption has been showing an exponential trend in recent years and will continue to do so due to the advent of new technologies such as social media, cloud computing, video streaming, and AI, requiring zettabytes (1 zettabyte = 1 billion of terabytes) of data consumption worldwide [2,3]. This will require new faster devices for information transfer and processing. The coexistence of new demand for faster information devices and the challenges towards solving issues related to semiconductor technologies has brought nanophotonics as a promising platform. One of the avenues where nanophotonics find its applications is in the design of Electro-absorption Modulators (EAMs).

EAM/EOM encodes high-speed electronic signals onto optical signals [4]. They are an integral component in silicon photonic integrated circuits (PICs) for intra-chip (on-chip) and inter-chip optical interconnects for applications in areas such as optical fiber communication in data centers [5,6], photonic neural networks [7], biomedical sensing, and long-range light detection and ranging (LiDAR) [8]. The high demand for modulators with ever-increasing performance has driven a need for efficient designs of EAM in terms of the figure of merits (FOM) factors such as high extinction ratio (ER), low insertion loss (IL), small footprint, and high speed [9]. Different

schemes that have been reported for the realization of EAM include high-Q photonic ring resonators [10–12], photonic crystal cavities [13–15], as well as plasmonic and hybrid plasmonic-photonic devices. In plasmonic and hybrid plasmonic-photonic devices [16–21], one common aspect is the existence of the metal contact on top of or in the vicinity of the active modulating region that partially pulls the electromagnetic field out of the guiding layer. This gives rise to the plasmonic nature of the device wherein energy is transferred to surface plasmon oscillations [22]. This plasmonic nature is beneficial as it facilitates deep sub-wavelength confinement of light and thus increased light-matter interaction (LMI) enabling improved sensitivity to a dynamic layer, a small device footprint, and dense device integration. However, this phenomenon inevitably results in increased ohmic losses even at the devices off-state when no modulation is required as the light should always interact with the metal. While plasmonic modulators are therefore able to achieve strong modulation, small size, and energy-efficient operation, they suffer from being lossy, with insertion loss values in the range of ~3 – 10 dB, and in some cases even more [17,19]. Ultimately, this limits the practicality of such devices.

There is a need to explore the potential to reduce the loss associated with plasmonic devices, and one avenue is the plasmon-assisted technique. Recently, a plasmon-assisted modulator based on a metal-insulator-metal (MIM) ring resonator has been demonstrated to show a 6 dB reduction (4x) in IL when compared to a non-resonant push-pull Mach Zehnder (MZ) plasmonic device. In this approach, the plasmonic section is selectively used or bypassed to reduce insertion loss by selectively passing light through the plasmonic section only at the device's off (in resonance) state [23].

This research aims to transition this approach to a non-resonant device by utilizing free-carrier modulation to generate an ENZ layer within an otherwise purely dielectric environment and evaluate the trade-offs in the design technique. In particular, by replacing the metal contact typically found in a conventional plasmonic or hybrid plasmonic EAM with a heavily doped layer of ITO ($N = 1 \times 10^{20}$ cm^{-3}). However, the base carrier concentration is not sufficient to exhibit a metallic response at the operating wavelength of 1.55 µm under the zero-biasing condition (*i.e., off or high-transmission state*). Thus, the light experiences non-metallic layers for minimal IL. Modulation is achieved through the application of a bias, which generates an ENZ layer through carrier accumulation and localizes the electric field within the lossy ENZ layer for strong modulation. Using this approach we study the performance of rib, slot, and multi-slot waveguides using realistic material/fabrication constraints as well as non-idealities (*e.g., contact voltage drop, dielectric breakdown, carrier accumulation via quantum models*). Through the lens of ENZ surface-to-TCO volume ratio, we illustrate the potential for a 4-slot based EAM with an ER of 2.62 dB/µm and IL 0.3 dB/µm operating at ~1 GHz and a single slot design with ER of 1.4 dB/µm and IL of 0.25 dB/ µm operating at ~20 GHz. Furthermore, the research will illustrate the trade-offs in the performance that must be carefully optimized for a given scenario and point toward the need to improve the mobilities of conformal ENZ materials to push the frontier of device performance. Besides theoretical analysis, this research also investigates the optical and electrical properties of constituent materials in the proposed scheme of EAM leaving behind some scopes that could be further investigated.

2. Background

2.1. E-K Diagram

While two hydrogen atoms are initially far apart, the electron in each atom will not interact with each other. But as the two atoms are brought closer and closer, they will interact, and thus their radial probability function, $p(r)$ will overlap as shown in Figure 2.1(a) [24]. The Pauli exclusion principle states that the joining of atoms to form a system (*i.e., crystal*) does not alter the total number of quantum states. So, the interaction will result in the discrete quantized energy level splitting into two discrete energy levels as schematically shown in Figure 2.1(b) [24] Similarly,

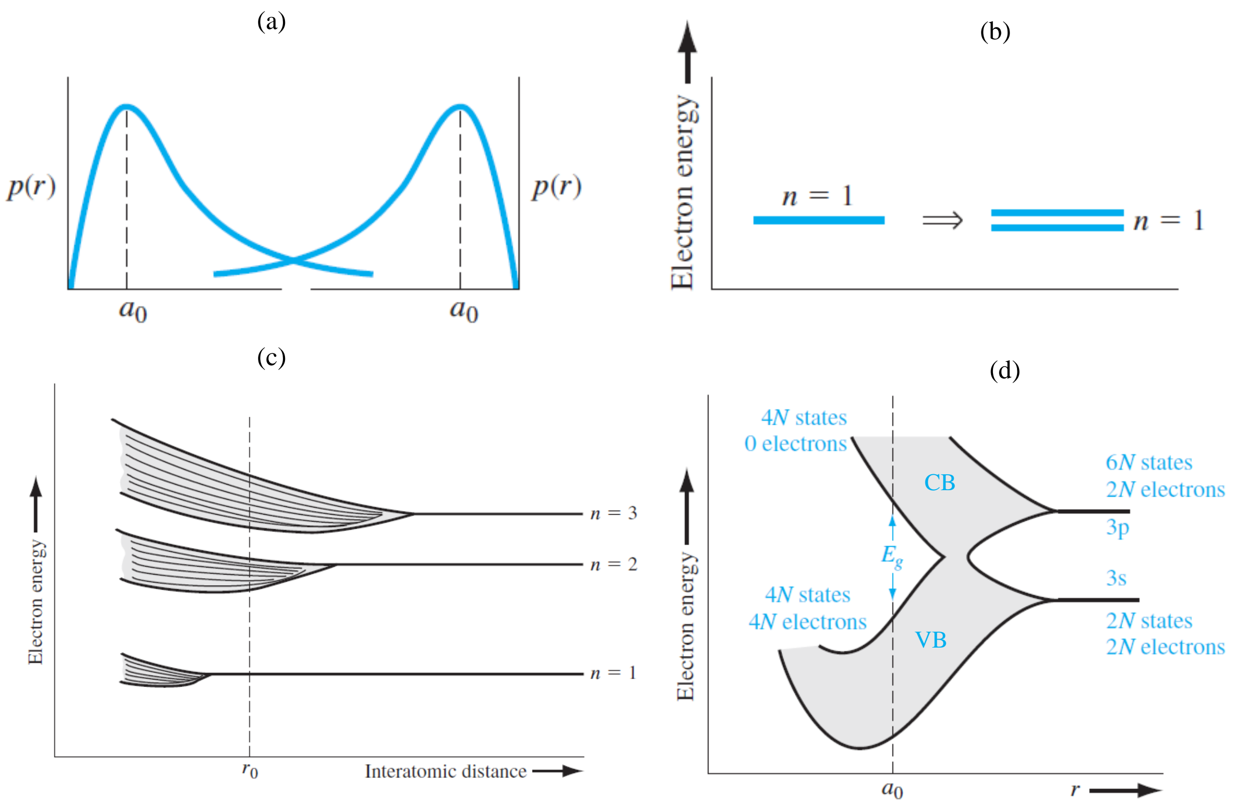

Fig. 2.1: (a) The overlapping radial probability function of two electrons in two adjacent hydrogen atoms. (b) Splitting of discrete energy level for state $n = 1$ (c) Splitting of discrete energy levels for a crystal with more than one electronic orbit. (d) interaction of 3s and 3p state give rise to hybridized sp^3 electronic states in Si [24].

for a series of hydrogen atoms, there will be a range of discrete energy levels for electrons in the crystal to satisfy the same Pauli exclusion principle. Just like hydrogen atoms each with only one electron orbit, atoms with more than one electron orbit, there will be a band of discrete levels of energies for each electron orbit. For example, Figure 2.1(c) shows the schematic for the splitting of three energy states into the allowed band of energies. Here r_0 is the equilibrium interatomic distance at which the forces (attraction and repulsion) between atoms find a balance [25]. As an example, Si has 14 electrons out of which 10 electrons are firmly bonded and closer to its nucleus. Its electronic structure is $[Ne]3s^2 3p^2$. The outer four electrons are loosely bounded to the nucleus and participate in chemical reactions [26]. As the interatomic distance decreases, the 3s and 3p states interact, overlap, and form hybridized sp^3 electrons. As a result, four quantum states per atom are generated in the lower and upper levels as shown in Figure 2.1(d) [24,25]. Here N denotes the number of Si atoms in the crystal and $a_0 = r_0$. These levels are also referred to as valence (VB) and conduction band (CB) respectively. All electrons will be in the VB at absolute zero degrees and thus will be full while the CB will remain empty. The gap between the VB and CB is also known as forbidden energy or simply band gap (E_g). For example, Si has a bandgap of ~ 1.12 eV [26].

As many atoms are brought close together, they may coalesce into periodic arrangements or a crystal structure. For a 1D crystal system where the atoms are closely packed, the quantum behavior of electrons is described by the Kronig-Penny model [24]. This model represents the 1D crystal as periodic potential as shown in Figure 2.2. The motion of electrons confined within a single-crystal system ($E<V_0$) can be derived by solving the Schrödinger wave equation [24,27].

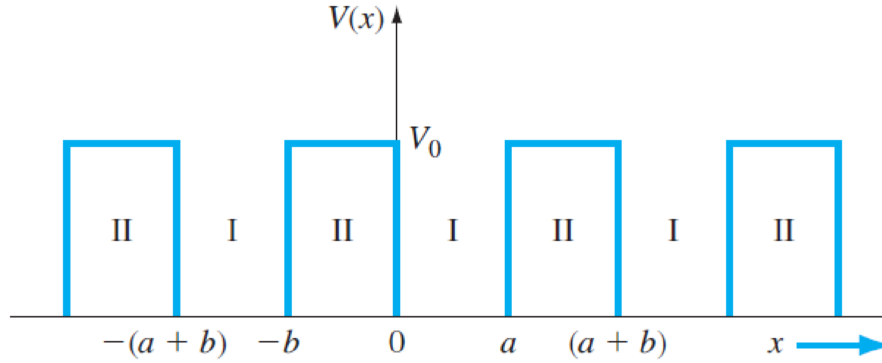

Fig. 2.2: A one-dimensional arrangement of atoms within a crystal is represented by a one-dimensional periodic potential function in a Kronig-Penny model [24].

The solution is derived with the help of the Bloch theorem [24,25,28]. The theorem is one of the most important theorems basic to band structure [27]. The theorem states that for all electrons within a periodically varying potential function, the total solution to the wave equation could be derived by considering the product of time-independent and time-dependent solutions as expressed by Equation 2.1.

$$\Psi(x,t)=\psi(x)\phi(t)=u(x)e^{jkx}.e^{j(kx-(E/\hbar)t)} \qquad 2.1$$

Here, k is a constant of motion. $u(x)$ is a periodic function with a period $(a+b)$, where the a and b are the lattice constants that represent the distance between atoms. E is total energy. The relation between total energy E and parameter k and the potential barrier V_0 is given by Equation 2.2.

$$P'\frac{\sin\alpha a}{\alpha a}+\cos\alpha a=\cos ka \qquad 2.2$$

where, $P'=\frac{mV_0ba}{\hbar^2}$ and the parameter $\alpha=\sqrt{\frac{2mE}{\hbar^2}}$

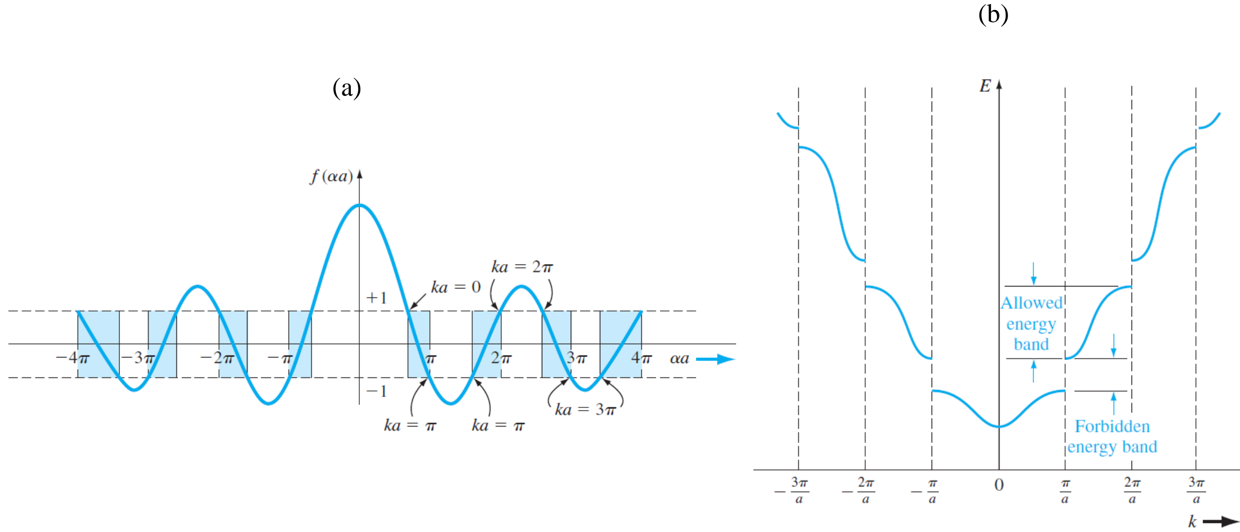

Fig. 2.3: (a) The plot showing the $f(\alpha a)$ (solid blue line) and the shaded region indicating the allowed values of αa for real values of wave number k. (b) E vs k diagram derived from (a) showing allowed states and forbidden energy gap within a crystal [24].

Equation 2.2 is not a direct solution but provides conditions at which the Schrödinger wave equation will have a solution. Figure 2.3(a) shows the plot of the left side (blue solid line) as a function of αa and the right side (cosine function, shaded areas bounded by +1 and -1) of Equation 2.2. As α^2 is related to E, a plot of E of the particle as a function of the real values of wave number can be generated from Figure 2.3(a) as shown in Figure 2.3(b). Figure 2.3(b) shows the allowed and forbidden energy bands. On the right side of Equation 2.2, the cosine function is periodic. Thus, a displacement of a portion of Figure 2.3(b) by 2π could be applied while still satisfying Equation 2.2. Figure 2.4(a) shows the resulting reduced E-k diagram contained within the defined range $-\pi/a < k < \pi/a$ [24]. The band gap in a material is also simply represented as two separate straight lines separated by band gap energy E_g as shown in Figure 2.4(b) [26]. The E_c and E_v represent CB and VB respectively.

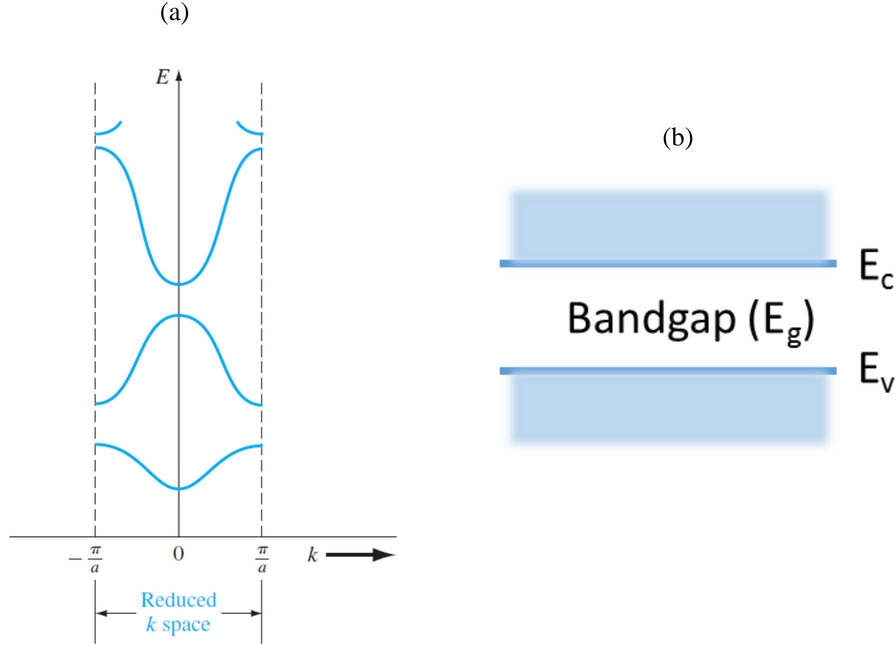

Fig. 2.4: (a) The E vs k diagram for a reduced k space [24]. (b) Simple representation of CB, VB, and E_g.

2.2. Density of States and Fermi Function

As discussed in the preceding section, both CB and VB could possess a range of discrete energy levels also known as Density of States (DOS). DOS for CB and VB is expressed by Equation 2.3(a,b) given the condition that the energies (E) are not too far from the band edges [26].

$$g_c(E) = \frac{m_n^* \sqrt{2m_n^*(E - E_c)}}{\pi^2 \hbar^3} \; where, E \geq E_c \tag{2.3(a)}$$

$$g_v(E) = \frac{m_p^* \sqrt{2m_p^*(E_v - E)}}{\pi^2 \hbar^3} \; where, E \leq E_v \tag{2.3(b)}$$

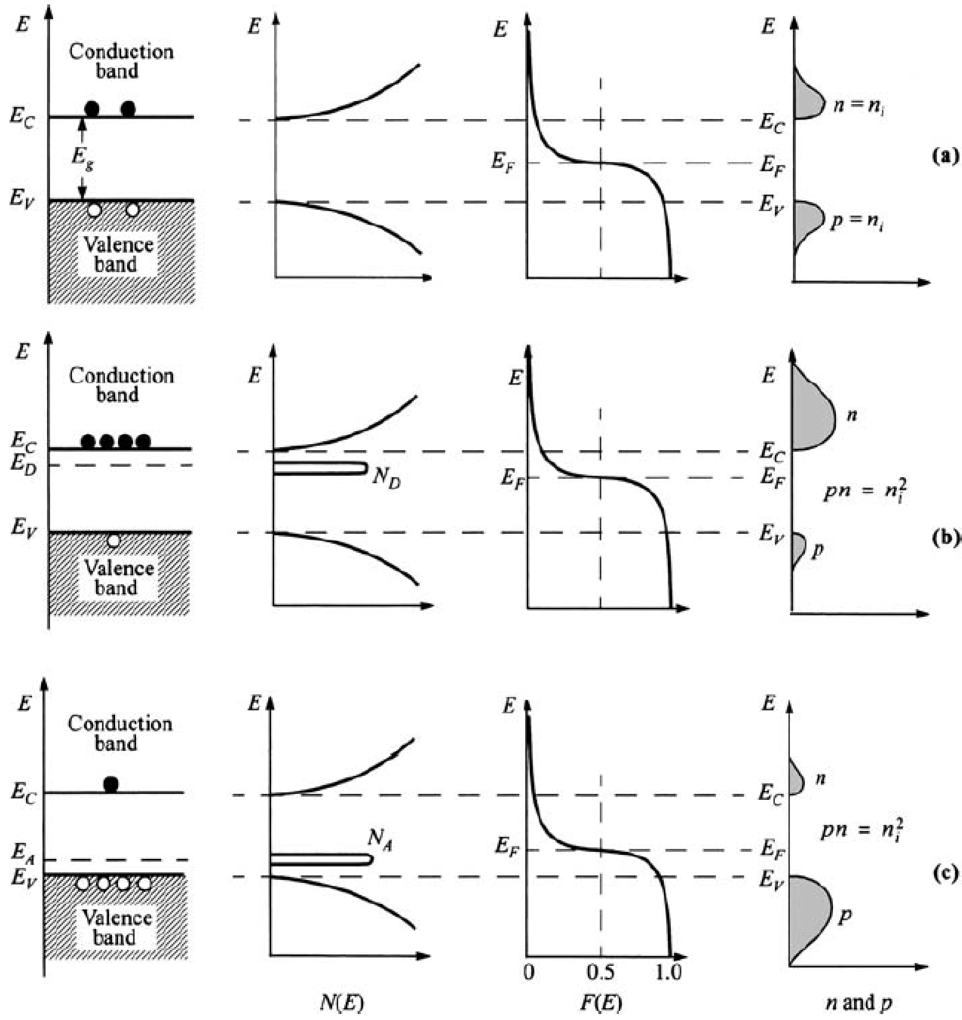

Fig. 2.5: Schematic band diagram, Density of States, Fermi-Dirac distribution, and Carrier concentration for (a) intrinsic, (b) n-type, and (c) p-type semiconductors at thermal equilibrium [27].

Although DOS indicates how many states exist at a given energy *E*, it cannot quantify how many of them are filled. To describe this, a function known as the Fermi function, *f(E)* is used that specifies the probability that an available state at an energy *E* will be occupied by an electron under equilibrium conditions. The function is expressed by Equation 2.4.

$$f(E) = \frac{1}{1 + e^{(E - E_F)/KT}} \tag{2.4}$$

where, E_F = Fermi energy or Fermi level, K = Boltzmann constant, T = Temperature.

The product of DOS and the Fermi function helps to determine carrier concentrations (electrons or holes) in the CB and VB. For example, $g_C(E)f(E)$ and $g_V[1-f(E)]$ manifest electron and hole concentration in the CB and VB respectively. Carrier concentrations for three different positions of Fermi energy with corresponding diagram, Fermi Function, and DOS are shown in Figure 2.5. From the figure, the Fermi level defines the doping level of a material. When E_F lies near or above E_C, electron concentration outweighs the hole concentration and thus the material is *n*-type (electrons being the majority and holes being the minority carriers). When E_F lies near or exactly at the mid-gap level, there is a balance in the concentration of electrons and holes in the CB and VB respectively, resulting in an intrinsic material (the equivalent carrier concentration is also referred to as intrinsic carrier concentration, $n_i = n_0 = p_0$ [24]). By intrinsic, a material is referred to as possessing no impurity atoms and no lattice defects in the crystal (*e.g., pure Si*). On the other hand, if E_F lies near or below the E_V then the material has more holes than electrons (holes being the majority and electrons being the minority carriers) resulting in the material *p*-type. For a semiconductor, the electron (n) and hole (p) concentrations are expressed as Equation 2.5 (a,b) [26].

$$n = N_C e^{(E_F - E_C)/KT} \tag{2.5(a)}$$

$$p = N_V e^{(E_V - E_F)/KT} \tag{2.5(b)}$$

Where N_c and N_v denote the effective density of states in the CB and VB respectively. Note that the Fermi function is not a physical material property. It helps to understand the doping level and

carrier concentration in a semiconductor and can then be altered by external perturbation (such as an applied voltage or by changing the temperature).

2.3. Doping of Semiconductor

When an ideal semiconductor material is grown, it contains only the constituent materials necessary to form the compound, such as Si atoms or Ga and As atoms for GaAs. The resulting Fermi level for this material would be that of the intrinsic material. To shift the Fermi level to either add electrons or holes, the Fermi level should be adjusted. This can be done statically by doping the material with donor or acceptor atoms.

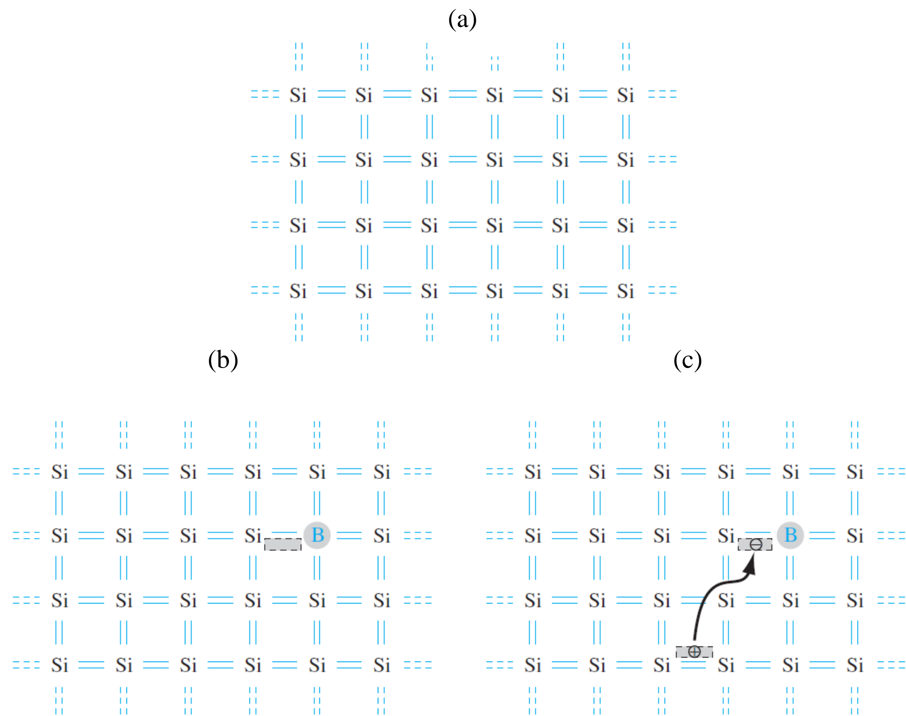

Fig. 2.6: (a) 2D representation of single crystal intrinsic Si atoms, (b) Si doped with boron atom, and (c) corresponding ionization of boron atom and the creation of hole within the crystal [24]

To further extend the concept of doping and its effect on the Fermi level, Figure 2.6(a) shows two-dimensional single-crystal pure Si atoms bounded together due to covalent bonding. There is no net charge in the crystal *i.e.,* it is intrinsic. If a foreign material from group III (*e.g., Boron*) is introduced, it will act as a substitutional impurity to silicon. Boron has three valence electrons with which each B atom will form three covalent bonds with the three adjacent Si atoms. However, Si has four valence electrons, and there will be an empty position in the covalent bonding with the fourth Si atom as shown in Figure 2.6(b). This empty position can be considered a hole. At absolute 0K, no valence electrons within the crystal will have sufficient energy to fill this hole. However, a valence electron could gain sufficient thermal energy at an elevated temperature (*e.g., in-room temperature*) to fill that hole before creating a hole at its original position at the VB as shown in Figure 2.6(c). The boron atom will now be negatively ionized. This scenario could be seen as a flow of a hole within the crystal or in other words a current flow.

An appreciable number of holes could be generated in the VB with the introduction of a high concentration of B atoms in the crystal. Consequently, the probability of finding a hole, $[1- f(E)]$ increases as more holes are generated in the VB. According to Equation 2.5(b), this causes the Fermi-level E_f to move closer to and even below the VB edge resulting in increasing hole concentration (p) in the crystal making the crystal preponderant with holes or simply p-type. A similar situation for donor atoms from group V (*e.g., P for Si*) can be introduced to generate excess electrons and thus an n-type material. In this research, Si has been incorporated into the EAM design to act as both the guiding layer for light and the ground contact (only a top 10 nm layer) for the appropriate biasing necessary for the desired light modulation. The resistivity of pure Si is in the order of mega-ohm which could significantly affect EAM device performances, especially the

operating speed as it is inversely proportional to the resistance. That is why Si sheet resistivity has been investigated by doping it with a boron dopant which will be discussed in chapter 4.7.

2.4. Metal-Oxide/Insulator-Semiconductor (MOS/MIS)

A Metal-Insulator-Semiconductor (MIS) or Metal-Oxide-Semiconductor (MOS) gate structure that houses the tunable material is an indispensable component of an Electro-Absorption Modulator (EAM). A typical MIS or MOS structure contains a thin oxide (*e.g., SiO_2, Al_2O_3, HfO_2, etc.*), with thickness, d typically in the order of 5 nm to 1µm, sandwiched in between a metal and a semiconductor [26]. The typical metals that are used include aluminum, gold, etc. [29], whereas Si is a perfect example of a semiconductor. Figure 2.7 (a,b) shows a schematic and the equivalent Energy Band Diagram (EBD) of an MIS structure under no biasing condition [27].

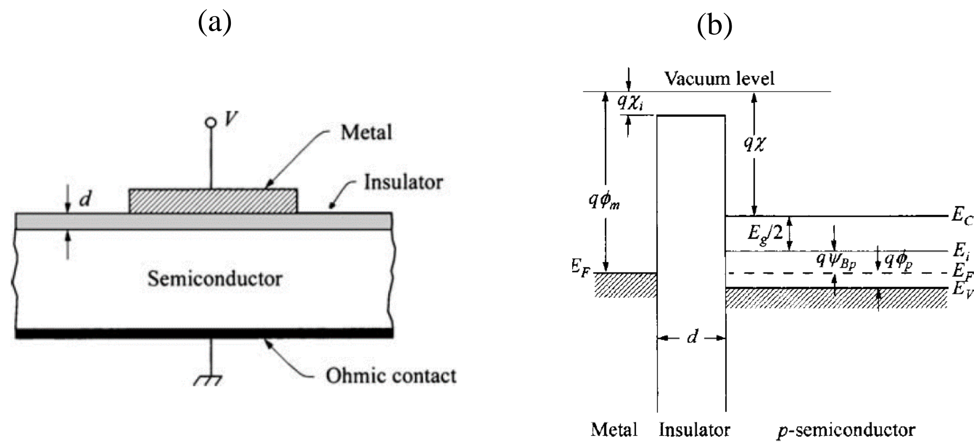

Fig. 2.7: A typical Metal-Insulator-Semiconductor (MIS) gate structure (a) schematic showing individual components and (b) equivalent energy band diagram [27].

In Figure 2.7 (b), the semiconductor is presented with a finite band gap ($E_g = E_c$-E_v) (*e.g., ~1.12 eV for Si*), mid-band gap energy (E_i), and the Fermi level (E_F) indicating the doping type of the semiconductor (*e.g., undoped, p-type or n-type*). For example, in the figure, the semiconductor is *p*-type as the Fermi level is lower than the mid-band gap energy. On the other hand, the metal gate is only represented with a Fermi level since VB and CB overlap in a conventional metal (*e.g.,*

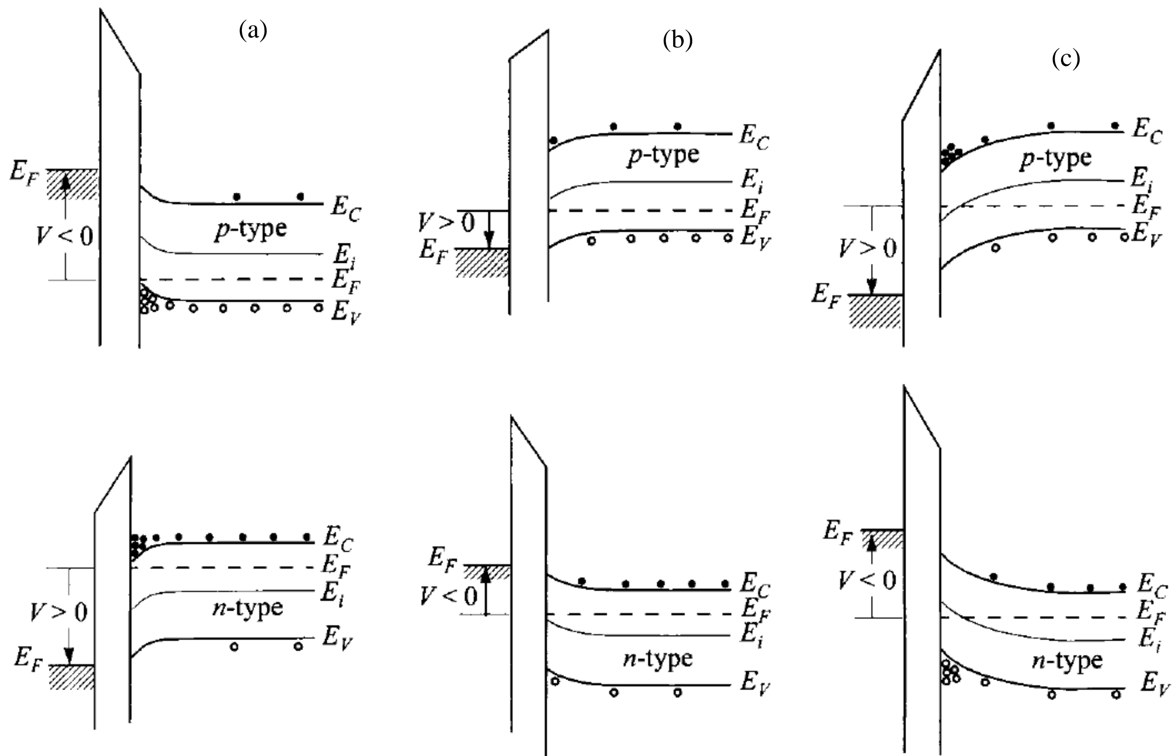

Fig. 2.8: Energy band Diagrams of ideal MIS structure depicting three different scenarios (a) Accumulation, (b) Depletion, and (c) Inversion [27]

gold). The Fermi level in metal and semiconductor aligns since no electric field exists across the structure under the zero-biasing condition. The Φ_m is defined as the metal's work function which is the energy difference between the Fermi and the vacuum level. The vacuum level is the minimum energy (or surface energy barrier) that an electron must possess to free itself from a

material. Unlike metal, the surface energy barrier for an electron in a semiconductor is quantified by the energy difference between the vacuum level and CB, E_c, also known as electron affinity, χ. For a semiconductor, E_c is used instead of E_F because the Fermi level is not constant and varies as a function of variable parameters, for example, the level of doping, and band bending near the interface with oxide. The oxide is represented as a wide band gap since it hinders charges to flow through it in an ideal condition of having no defect. Figure 2.8 shows the EBD of an MIS gate structure under different biasing conditions. The top and bottom figures are for *p*-type and *n*-type semiconductor substrates respectively.

For a *p*-type substrate, under a negative gate voltage, $V<0$, the metal Fermi level shifts up. It causes a negative sloping of the energy bands in both oxide and semiconductor. The energy difference between E_F and E_v reduces near the oxide/semiconductor interface resulting in hole accumulation at the interface within the semiconductor. Figure 2.9(a) pictorially shows the charges within metal and semiconductor near the corresponding interfaces with oxide. This type of simple representation for charge distribution is referred to as a block charge diagram. At this condition the total areas under the negatively and the positively charged carriers within the metal and semiconductor respectively are equal. The condition at which the majority carrier concentration is

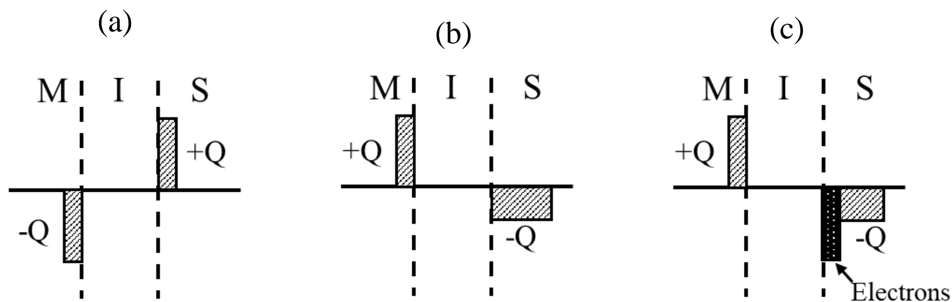

Fig. 2.9: Block charge diagram of a MIS gate with *p*-type semiconductor for the simple depiction of three conditions namely (a) Accumulation, (b) Depletion, and (c) Inversion [26]

greater at or near the interface than in the bulk of the semiconductor is referred to as accumulation. The Fermi level remains flat (Figure 2.8) in both the metal and semiconductor since no current flows under the zero-biasing condition ($dE_F/dx = 0$). When a small positive gate voltage less than a threshold voltage (V_T) such that $V_T > V_g > 0$ is applied, the metal Fermi level lowers down. It causes a positive sloping of the band structures in both oxide and semiconductor resulting in the depletion of the majority carriers (holes) near the oxide/semiconductor interface. This is referred to as depletion as pictorially shown in Figure 2.9(b). At a higher positive gate voltage, the bands within the semiconductor bend even more downward. The mid-gap level, E_i near the interface crosses over the Fermi level, causing an accumulation of minority carriers (electrons). This phenomenon at which the minority carrier concentration is greater than the majority carriers (holes) near the interface within the semiconductor is referred to as inversion (Figure 2.9(c)). The three scenarios can also be seen in the case of an n-type semiconductor, of course, the polarity of applied gate voltages flips as shown in the bottom part of Figure 2.8. In this research, an MIS is an indispensable component for the realization of EAM consisting of ITO/HfO_2/p-Si where the ITO and p-type Si act as metal contact and semiconductor respectively. The carrier transport within metal and semiconductor under the biasing condition can be analyzed by several methods and will be discussed in the following section while the optimization of which will be discussed in chapter 3.2.

2.5. Analysis of Carrier transport in an MIS gate structure

In an MIS gate structure, under biasing conditions, the transport of charge carriers in a semiconductor can be analyzed by several methods such as Drift-Diffusion (DD), Schrödinger-Poisson (SP), and Density Gradient (DG) Method [27,30,31]. These methods fundamentally differ from each other based on how each method treats the carriers within a semiconductor device.

In the DD method, "Drift" refers to the transport of charge carriers driven by an electric field while "Diffusion" indicates the transport of charge carriers due to the carrier concentration gradient. The electric field *E (V/m)* is defined from the laws of electrostatics as given by Equation 2.6(a,b):

$$\nabla \cdot (\varepsilon E) = \rho = q(p - n + N_d^+ - N_a^-) \qquad 2.6(a)$$

$$E = -\nabla V \qquad 2.6(b)$$

Here, ε is the permittivity (F/m), ρ is the charge density (C/m^3), and V is the electric potential (V). p, n are hole and electron concentration and N_d^+, N_a^- are ionized donors and acceptors respectively (1/m^3). q is the elementary charge in coulomb. The p and n are calculated from the current continuity equation as given in Equation 2.7(a,b).

$$\frac{\partial n}{\partial t} = \frac{-\nabla \cdot J_n}{-q} - \mathrm{Re}_n + G\mathrm{e}_n \qquad 2.7(a)$$

$$\frac{\partial p}{\partial t} = \frac{-\nabla \cdot J_p}{-q} - \mathrm{Re}_p + G\mathrm{e}_p \qquad 2.7(b)$$

Where, J_n and J_p are the electron and hole current densities (A/m^2), $Re_{n\ or\ p}$ and $Ge_{n\ or\ p}$ refer to recombination and generation rates for carriers (electrons or holes). The electron and hole current densities in Equation 2.7(a,b) can be expressed by Equation 2.8(a,b)

$$J_n = qn\mu_n \nabla E_{fn} + qn((E_c - E_{fn})\mu_n + Q_n)\nabla T / T \quad 2.8(a)$$

$$J_p = qp\mu_p \nabla E_{fp} - qp((E_v - E_{fp})\mu_p + Q_p)\nabla T / T \quad 2.8(b)$$

Here μ_n and μ_p are the electron and hole mobilities (m^2/V/s), E_c and E_v are the conduction and valence band edges (V), Q_n and Q_p are the electron and hole nonequilibrium contributions to the thermal diffusion coefficient (m^2/s), and T is the temperature (T). With the help of EBD, the conduction and valence band edges (E_c and E_v) can be expressed in terms of electric potential (V), electron affinity (χ), and band gap (E_g) as given in Equation 2.9(a,b).

$$E_c = -V - \chi \quad 2.9(a)$$

$$E_v = E_c - E_g \quad 2.9(b)$$

As the semiconductor devices get smaller and smaller, considering quantum confinement becomes more and more important, especially for an MIS with an ultrathin dielectric oxide (thickness < 5 nm) [32]. DG and SP consider quantum phenomena as opposed to the DD method. Both the DD and DG theory obeys the electrostatics and current conservation laws. According to the DD theory, the n and p are defined in terms of quasi-Fermi levels (E_{fn} and E_{fp} respectively) as given in Equation 2.10(a,b).

$$n = N_c F_{1/2}\left(\frac{E_{fn} - E_c}{K_B T / q}\right) \quad 2.10(a)$$

$$p = N_v F_{1/2}\left(\frac{-E_{fp} + E_v}{K_B T / q}\right) \quad 2.10(b)$$

where $N_{c\ or\ v}$ indicates the corresponding DOS in CB and VB respectively. $F_{1/2}$ is the Fermi-Dirac integral, and the K_B is the Boltzmann constant. On the other hand, according to the DG theory, the equation of states of a carrier (electron/hole) gas depends not only on its density but also on its density gradient and the theory does so by including a quantum potential term (V_n^{DG} and V_p^{DG} corresponding to electrons and holes respectively) in Equations 2.10(a,b) and the modified equations are given in Equation 2.11(a,b)

$$n = N_c F_{1/2}\left(\frac{E_{fn} - E_c + V_n^{DG}}{K_B T / q}\right) \quad 2.11(a)$$

$$p = N_v F_{1/2}\left(\frac{-E_{fp} + E_v + V_p^{DG}}{K_B T / q}\right) \quad 2.11(b)$$

The quantum potentials are defined in terms of DG coefficients, b_n and b_p (Vm^2), and expressed by Equation 2.12(a,b).

$$\nabla \cdot (b_n \nabla \sqrt{n}) \equiv \frac{\sqrt{n}}{2} V_n^{DG} \quad 2.12(a)$$

$$\nabla \cdot (b_p \nabla \sqrt{p}) \equiv \frac{\sqrt{p}}{2} V_p^{DG} \quad 2.12(b)$$

The DG coefficients measure the strength of the gradient effect in the carrier gas and are defined in terms of the inverse of the DG effective mass, (m_n^* and m_p^* (Kg) for electrons and holes respectively) as expressed by Equation 2.13(a,b) [33].

$$b_n = \frac{\hbar^2}{4rq}[m_n^*]^{-1} \qquad 2.13(a)$$

$$b_p = \frac{\hbar^2}{4rq}[m_p^*]^{-1} \qquad 2.13(b)$$

Here *r* is a dimensionless parameter. The usual practice to determine the carrier profile is to fix the value of *r* while changing the value of $m^*_{n\ or\ p}$ and compare the results with the solutions obtained from solving the Schrödinger and Poisson (SP) equations under the same conditions (*e.g., bias, doping level, oxide thickness*). However, the product of $m^*_{n\ or\ p}$ and *r* is almost one under all conditions [32,34].

Figure 2.10 (a,b) shows carrier density distribution perpendicular to a SiO_2/Si interface [35] derived using the classical DD and quantum correction included DG method respectively. Both approaches satisfy the requirement of boundary condition, $j_z\ (x,z) = 0$. The DD approach does so by considering a maximum carrier density at the interface due to which drift and diffusion current cancel each other as shown in Figure 2.10(a). On the other hand, the DG method only corrects either one term, effectively the drift one in classical current to guarantee a vanishing current perpendicular to the interface at z=0 as shown in Figure 2.10(b) [35].

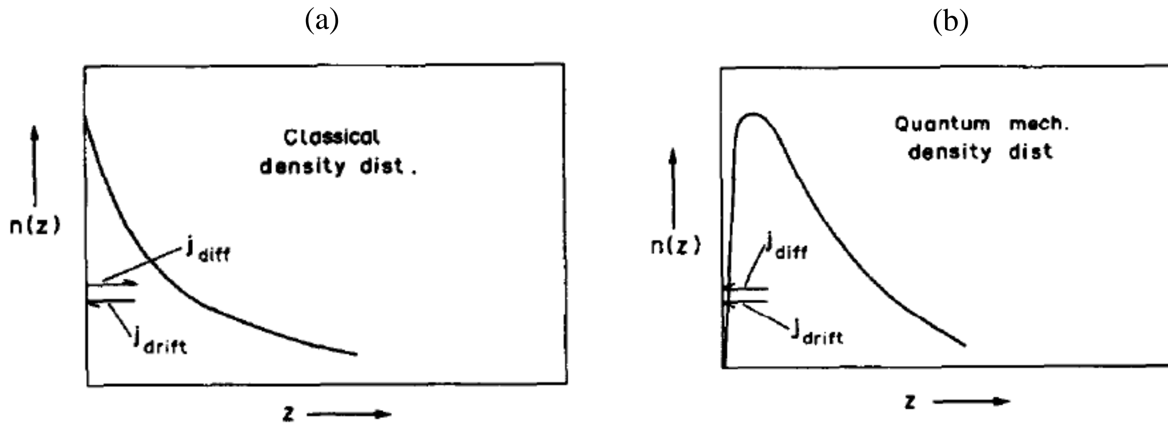

Fig. 2.10: Carrier density distribution the near the interface between SiO_2/Si in a perpendicular direction according to (a) Classical DD model, (b) Quantum correction included DG method [35]

Both SP and DG consider the quantum effect, but the DG outperforms the former for shallow wells and for simulating the density deep inside a semiconductor unless SP analysis includes a large number of sub-bands. Besides the DG theory is promising since it is reported as computationally efficient and fits naturally into the framework of conventional device simulations [32]. Figure 2.11

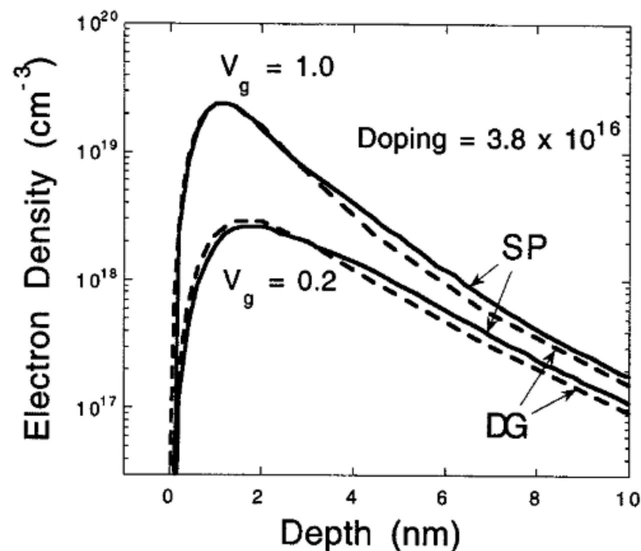

Fig. 2.11: Electron density profile within a Si inversion layer incorporated in a MOS structure derived from SP and DG method at two different voltages [32]

shows the electron distribution in a Si inversion layer from a MOS structure. The profile predicted by the DG matches well with what has been predicted by the more rigorous SP approach. In this research, the DG method has been used applying quantum confinement to analyze the MIS that houses the active tuning material ITO. ITO facilitates free carrier accumulation under appropriate biasing conditions giving rise to increased LMI followed by the Drude-Lorentz oscillator model that will be discussed in the following section.

2.6. Lorentz Oscillator Model

Light-Matter Interaction (LMI) involves the interaction between an electromagnetic field (*i.e., light*) and constituent atoms within a material (*i.e., crystal*). For simplicity, let us assume that a light wave acts as a driving force that causes electrons bound to a nucleus of a single atom within a crystal to oscillate. Besides, the oscillation results in a dipole moment as electrons get displaced from their equilibrium position and thus the atom possesses a single resonant frequency ω_0. As a result, the oscillating dipole radiates electromagnetic waves. This dipole phenomenon is also known as the Lorentz oscillator [36]. The displacement x of the electrons is expressed by an equation of motion as given in Equation 2.14.

$$m_0 \frac{d^2 x}{dt^2} + m_0 \gamma \frac{dx}{dt} + m_0 \omega_0^2 x = -eE \qquad 2.14$$

Here, m_0 is electron mass and E is alternating light wave field. The terms on the left-hand side represent the acceleration, the damping, and the restoring force respectively while the single term on the right-hand side represents the driving force due to the alternating nature of the light wave.

The parameter, γ that represents the damping of the oscillation. This manifests the fact that the oscillation is associated with losses of energy due to collisional processes that occur within a crystal. For example, this could happen when an oscillating dipole interacts with a phonon (*i.e., the vibration of atoms*) within a crystal generated from thermal excitation. For a single atom, the dipole moment is expressed as $p = -eq$ where e is the electron charge. However, on a macroscopic scale, this leads to a volumetric polarization, simply dipole moment per unit volume. If N is the number of atoms per unit volume, the resonant polarization can be derived and expressed as shown in Equation 2.15

$$P_{resonant} = \frac{Ne^2}{m_0} \frac{1}{(\omega_0^2 - \omega^2 - i\gamma\omega)} E \qquad 2.15$$

Equation 2.15 indicates that the polarization is small unless the driving frequency ω of the light wave is close to the resonant frequency of the atoms. This leads to classifying the polarization of atoms as namely non-resonant background and resonant polarization. The electric field displacement D due to the light alternating wave E and the polarizations of atoms is expressed by Equation 2.16.

$$D = \varepsilon_0 E + \varepsilon_0 \chi E + P_{resonant} \qquad 2.16$$

where the second term on the right-hand side represents the non-resonant background, χ is the susceptibility of the material and ε_0 is vacuum permittivity and a constant. By combining equations 2.15 and 2.16, the complex relative dielectric constant (*i.e., permittivity*) of the material can be derived as given in Equation 2.17.

$$\varepsilon_r(\omega) = \varepsilon_\infty + \frac{Ne^2}{\varepsilon_0 m_0} \frac{1}{(\omega_0^2 - \omega^2 - i\gamma\omega)} \tag{2.17}$$

Here ε_∞ is the high-frequency permittivity. Figure 2.12 shows the frequency dependence of the real and imaginary part of the complex dielectric constant and refractive index for an oscillator with $\omega_0 = 100THz$, $\gamma = 5THz$, $\varepsilon_\infty = 1 + \chi = 10$, and the dielectric constant to static electric fields (*i.e.,* ε_{st} at $\omega = 0$) equal to 12.1.

From the figure, one important phenomenon that is useful for implementing an EAM is the ability to achieve a real permittivity value of near zero, also known as epsilon-near-zero (ENZ), and will be discussed in the next section. Unlike bound electrons, free electrons in certain crystals (*e.g., metal and highly doped semiconductors*) do not experience any restoring force. As a result,

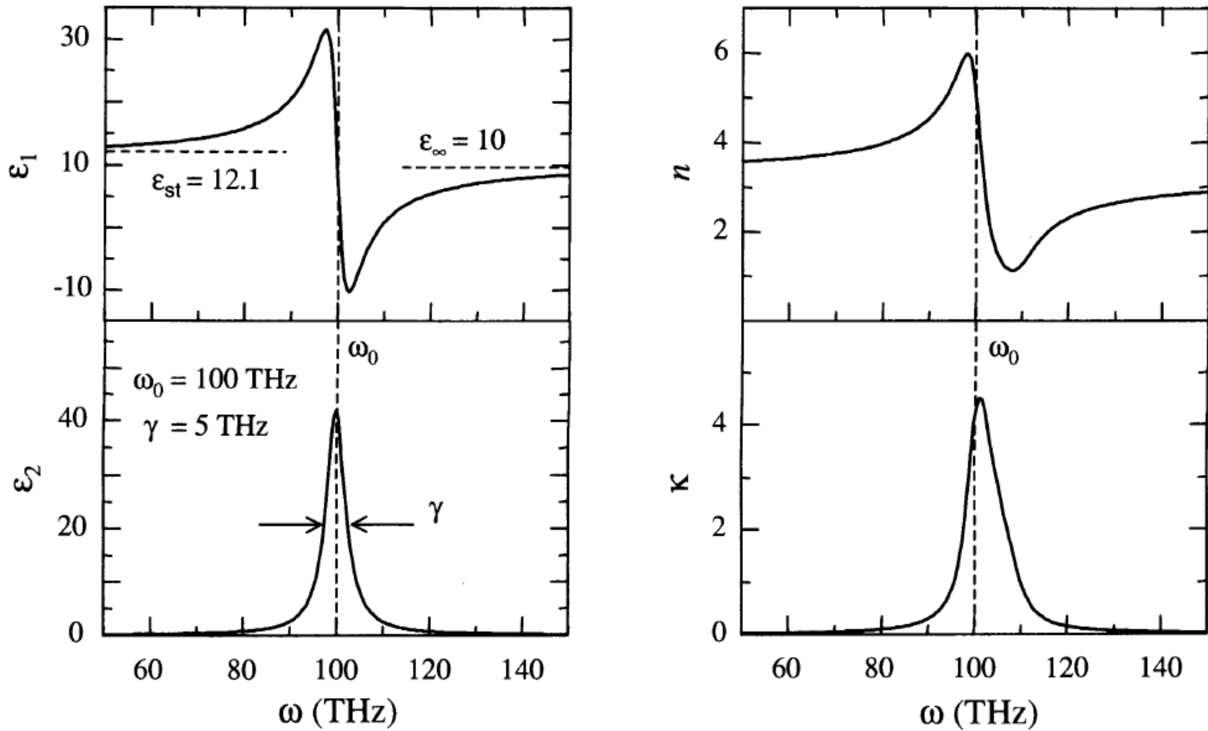

Fig. 2.12: Complex relative dielectric constant and the corresponding real and imaginary part of refractive index derived for a Lorentz oscillator [36].

electrons lack natural resonant frequency ($\omega_0 = 0$). Thus, the Lorentz oscillator model could be modified to model free electrons in such crystals by excluding the third term on the left-hand side of Equation 2.14. This free electron model is also known as the Drude model and expresses the metal permittivity as given in Equation 2.18.

$$\varepsilon_r(\omega) = \varepsilon_\infty - \frac{\omega_p^2}{(\omega^2 + i\gamma\omega)} = \varepsilon_\infty - \frac{\omega_p^2}{(\omega^2 + \gamma^2)} + i\frac{\omega_p^2\gamma}{(\omega^2 + \gamma^2)\omega} \qquad 2.18$$

Here, $\omega_p = \sqrt{Ne^2/m^*\varepsilon_0}$ is referred to as plasma frequency. Effective mass, m^* has been used as opposed to the free electron mass, m_0 to impose the dependency of the former on the band structure of a certain crystal. m* is inversely proportional to the curvature of the band structure. So, m^* will change depending on the distribution of electrons population in a non-parabolic band structure.

2.7. Epsilon Near Zero Materials for photonic applications

In the previous section, the macroscopic polarization or permittivity of a material containing free electrons (*e.g., metals, doped semiconductors*) due to LMI has been expressed by the Drude oscillator model in Equation 2.18. The right-hand side of the expression contains two terms. One important aspect of the expression is when the two terms get equal or nearly equal. For example, by varying the doping level and thus the value of *N* within the expression of plasma frequency in the range 10^{20}-10^{21} cm^{-3}, the negative contribution due to free electrons and the positive contribution from the bound electrons in equation 2.18 nearly cancel each other [37]. In this scenario, the real part of the permittivity becomes zero or nearly zero and can be tuned within the region of interest covering across near-infrared (NIR) to mid-IR spectrum, facilitating a

phenomenon also known as epsilon-near-zero (ENZ). Moreover, ENZ could also be tuned by modulating the parameters in the expression such as m^* *and* γ by interband or intraband optical pumping [38] and electrical biasing [19,39,40] that have been reported in the literature. For example, electrons' effective mass (m^*) is inversely proportional to the curvature of the band structure. So, optically pumping an ENZ material with photons energy less than the band gap (intraband transition) results in hot electrons at the higher energy states in the CB and causes m^* to increase due to the nonparabolicity of the energy band structure [41]. This ENZ phenomenon with tunability is beneficial as it facilitates subwavelength field confinement through the requirement of the boundary condition that is the continuity of the normal component of the electric field ($\varepsilon_1 E_1 = \varepsilon_2 E_2$) and slow light effect [42,43]. Moreover, ENZ has emerged as an alternative to conventional metals [1], possessing the intrinsic ($\chi^{(3)}$) and extrinsic feature ($1/n^2$) to enhance non-resonant nonlinear LMI [42] demonstrating unity order refractive index modulation [44,45]. These key features made ENZ materials exhibit strong and ultra-fast nonlinearities within a sub-wavelength thickness with unique features, for example, the generation of higher harmonics by relaxing strict phase matching conditions as opposed to the conventional nonlinear materials (e.g., $LiNbO_3$, BBO, and KTP). Besides, they find applications in photonic devices such as optical isolators, all-optical switches, EO modulators and switches, perfect absorbers, LED, etc. [43].

Several schemes exist by which ENZ could be achieved and can be broadly categorized into four groups namely plasmonic ENZ materials having plasma frequency corresponding to free electrons, photonic multilayers composed of alternating dielectric-ENZ or dielectric-metal materials designed by effective medium theory, all-dielectric photonic crystals having ENZ at Γ point in the Brillouin zone, and hollow metallic waveguide exhibiting ENZ at 3 dB cutoff frequency [43].

Among all the schemes, the Transparent Conducting Oxide (TCO) material family includes promising materials such as indium tin oxide (ITO), indium-doped cadmium oxide (In:CdO), aluminum-doped zinc oxide (AZO), gallium-doped zinc oxide (GZO) [42,43,46,47]. Figure 2.13 shows the optical properties of several ENZ materials [1]. These materials are CMOS compatible and the homogeneous thin films of which can be deposited by well-established procedures using magnetron sputtering, chemical vapor deposition (CVD), and atomic layer deposition (ALD). These materials provide sufficient electrical conductivity to be used as an electrode while desired optical tuning can be achieved by appropriate biasing. This is why these materials are being used in nano-optoelectronic devices, for example as transparent conducting electrodes in touchscreens. Among the TCO materials, ITO has been widely reported due to its features such as wide bandgap

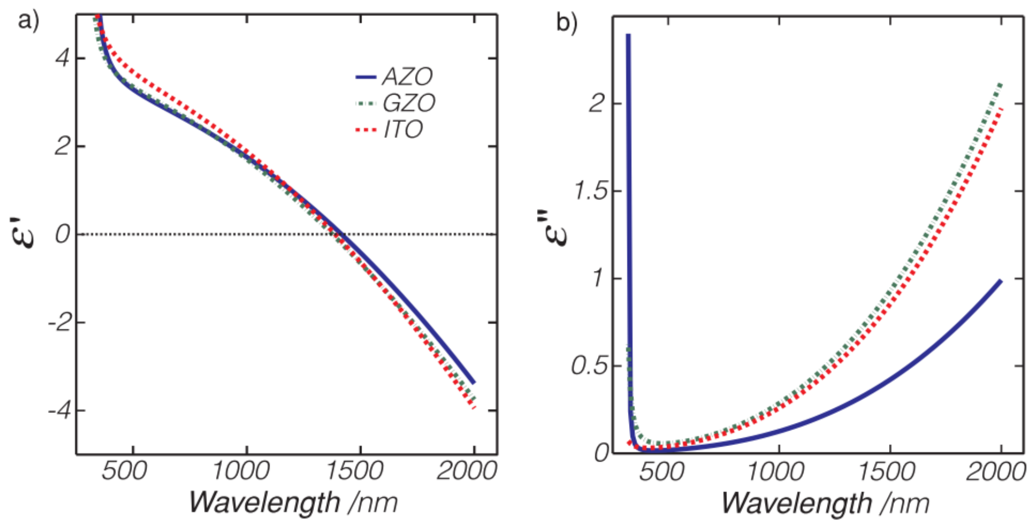

Fig. 2.13: (a) Real and (b) imaginary part of the permittivity of three ENZ materials [1].

(~3.8 eV), and ability to be highly doped (2 to 3 orders to that of the Si) [48]. This is why, in this research, ITO has been incorporated as both the gate transparent electrode and the tunable material

that gives rise to the ENZ phenomenon necessary for light modulation in an EAM. Besides ENZ, several other mechanisms have been demonstrated to conceptualize and implement EAM. These mechanisms will be discussed in the following section.

2.8. Methods of Electro-optic/absorption Modulator

An electrical signal can be encoded onto an optical signal by modulating light's fundamental properties such as amplitude, phase, polarization, and frequency. Implementing an EOM/EAM requires the incorporation of active tunable materials, the refractive index or the absorption coefficients of which are required to be changed upon the application of external perturbation (*e.g., voltage, current, optical pulse, temperature*) [49]. Figure 2.14 shows the schematic design flow

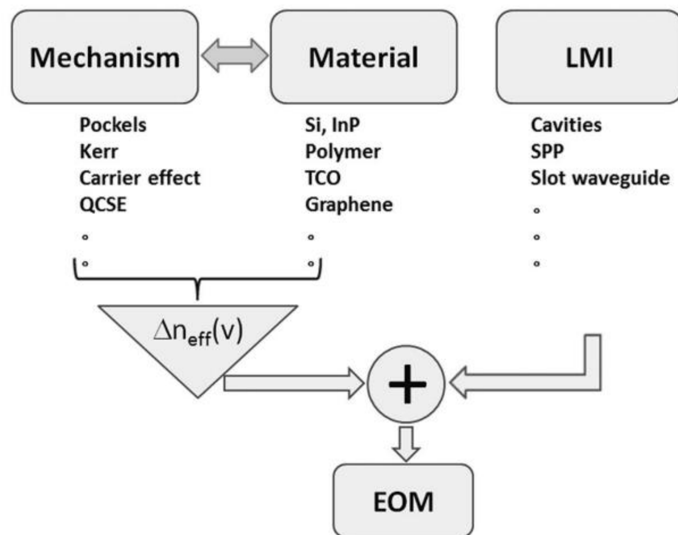

Fig. 2.14: Schematic showing basic design flow of implanting an EOM [49].

of building an EOM in which each scheme combined with an appropriate tunable material produces a function of refractive index change of the material. As shown in the figure, several

mechanisms can be used to realize an EAM. Among them, Pockel's and plasma dispersion effects are the two of the most common methods of modulation and will be broadly discussed along with a brief introduction of each other schemes in the following section.

2.8.1. Pockels and Kerr Effect

The electro-optic (EO) effect refers to a change in the real part of the optical refractive index (*n*) of a non-linear optical (NLO) material due to an external static or low frequency (smaller than the light frequency) electric field and is expressed as the Taylor series expansion in terms of the electric field as given in Equation 2.19 [50]

$$n(E) = n - \frac{1}{2} r n^3 E - \frac{1}{2} r n^3 E^2 + \ldots \qquad 2.19$$

The first term in the expansion refers to *linear electro-optic effect* or simply Pockel's effect due to linear dependence of refractive index change to the electric field and is usually the most dominant one compared to higher order terms. The coefficient *r* is referred to as Pockel's coefficient. On the other hand, the second term in Equation 2.19 indicates that the index change follows quadratically with the applied electric field, a third-order nonlinearity also known as the Kerr effect. However, the effect is much weaker compared to Pockel's effect for the same applied voltage resulting in inefficient modulation [51]. NLO crystals such as lithium niobate ($LiNbO_3$), potassium dihydrogen phosphate (KDP), barium titanate ($BaTiO_3$), and semiconductors such as gallium arsenide (GaAs), cadmium telluride (CdTe), and zinc telluride (ZnTe) [49,52] exhibit the Pockel's effect due to lack of inversion symmetry (i.e., non-centrosymmetric) in their crystal morphology.

As an example, $LiNbO_3$ is a uniaxial crystal exhibiting two different refractive indices namely ordinary (*n₀*) and extraordinary (n_e) refractive index even under no biasing condition. The corresponding expressions are given in Equation 2.20(a-b).

$$n_0(E) = n_0 - \frac{1}{2} r_{13} n^3 E \qquad 2.20(a)$$

$$n_e(E) = n_e - \frac{1}{2} r_{33} n^3 E \qquad 2.20(b)$$

where, $n_0 \sim 2.3$, $n_e \sim 2.2$, $r_{13} = 9.1 pm/V$, and $r_{33} \sim 30 pm/V$ at an operating wavelength of 633 nm [53]. For the relatively large Pockel's coefficient along the extraordinary axis (*i.e., the optical axis along the z-axis in the crystal*), an electric field applied along the crystal z-axis is preferable

to achieve an appreciable change in refractive index [54]. Having the relation in Equation 2.20, a phase modulator can be implemented by letting light pass through the materials while applying an electric field simultaneously as shown in Figure 2.15.

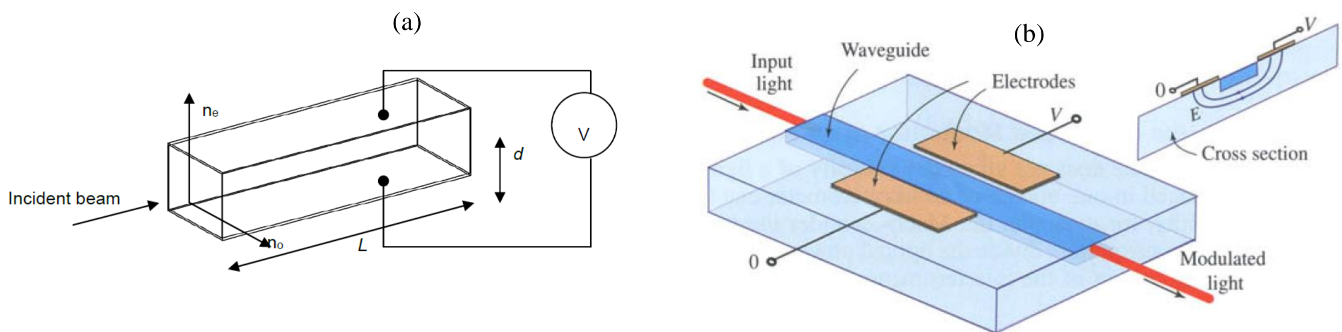

Fig. 2.15: (a) Application of a voltage across the optic axis (n_e) of a $LiNbO_3$ crystal (b). Schematic showing integrated phase modulator [50].

The propagating light will experience a phase change, $\phi = n(E)k_0L = 2\pi n(E)L/\lambda_0$. Putting the expression of $n(E)$ for the extraordinary axis (n_e), the phase change is given by Equation 2.21 [50].

$$\phi = \phi_0 - \pi \frac{V}{V_\pi} \tag{2.21}$$

where, $\phi_0 = 2\pi nL/\lambda_0$, d and L are the thickness and length of the crystal, λ_0 is the free space wavelength, $V = E/d$, and $V_\pi = (d\lambda)/(Lrn^3)$ corresponds to a π phase shift of the modulated light at the output end if applied voltage $V = V_\pi$. A phase modulator alone is not sufficient to realize an EO intensity modulator, rather can be realized by incorporating a phase modulator in one of the two arms of a Mach-Zehnder interferometer (MZI) as shown in Figure 2.16(a) [52,55]. Ideally, the input light intensity is split in half at the Waveguide Y's. In one of the arms, light traverse without any perturbation and acts as the reference beam. On the other arms, the light experiences a phase shift due to applied voltage. Both beams destructively interfere at the second

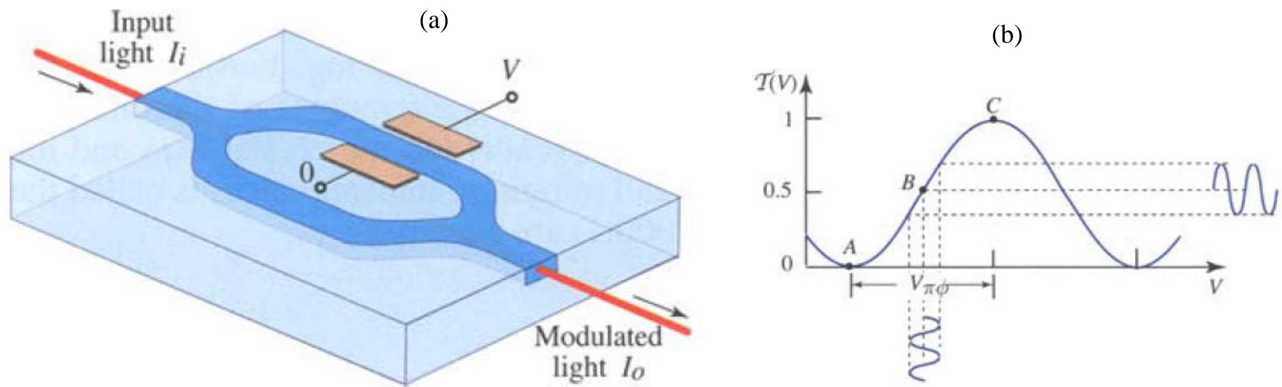

Fig. 2.16: (a) A MZI intensity modulator with the inclusion of phase modulator in one of the arms (b) Change in the transmission upon application of an applied voltage shown in (a). The voltage V_π required for a π phase shift and thus switching normalized transmission between 0 and 1 is shown [50].

Y junction of the waveguide leading to a change in intensity given by the expression in Equation 2.22 and plotted in Figure 2.16(b)

$$T(V) = \cos^2\left(\frac{\phi_0}{2} - \frac{\pi}{2}\frac{V}{V_\pi}\right) \qquad 2.22$$

2.8.2. Plasma Dispersion Effect

Light propagating through a material can be modulated by modulating the carrier concentration profile within that material. The carrier concentration profile can be modulated electrically or optically. For example, carriers could be accumulated, injected, or depleted in Si under an applied electric field. This will bring a change in both optical refraction and absorption in the material according to the Kramers-Kronig relation offering the opportunity to control both the amplitude and the phase of the traveling guided light wave [52]. This means of modulation is referred to as

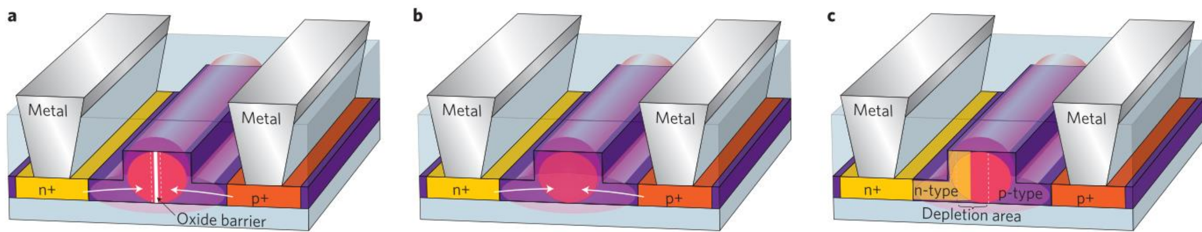

Fig. 2.17: Cross-sectional image of typical plasma dispersion-based Si optical modulators applying three different schemes such as (a) carrier accumulation using MOS configuration (b) carrier injection using p-i-n configuration, (c) carrier depletion using a lightly doped p-n junction [58].

the free carrier or plasma dispersion effect. For example, free carrier change in Si results in a change in refractive index that further results in a shift in resonance frequency [56,57]. So, Incorporating Si into MOS, p-n, and p-i-n configuration has been demonstrated for implementing modulators. Figure 2.17 shows schematics for such three schemes [58].

In MOS configuration (Figure 2.17a), light travels through a thin Si waveguide split in half by an oxide, confined and surrounded by gates and buried oxide. Upon biasing, opposite charge carriers accumulate and thus change the optical properties of the thin Si waveguide layers. However, the modulation speed and efficiency of this scheme are limited by the resistance and capacitance of the device and the lack of sufficient carriers within the Si layer. In a p-i-n configuration (Figure 2.17b), carriers are injected into the intrinsic Si region to increase the absorption where the light is mostly confined. However, there is a tradeoff between the device's speed of operation and the intrinsic silicon region width due to the long carrier recombination lifetime (in the order of nano-second). This could potentially be overcome using a carrier depletion-based scheme (Figure 2.17c) in which the guided Si region is split in half and the propagating light mode pass through two different regions, one lightly n-type and another p-type, respectively. Under a reverse bias state opposite carriers are pulled out of the waveguide region increasing the depletion region and thus imposing a change in the refractive index experienced by the propagating mode. The carrier extraction time even though is small (~pico-second) compared to its carrier injection counterpart but falls short in modulation efficiency due to the low number of carriers involved. Moreover, free carrier-induced optical change in Si is small [49,59]. To overcome these limitations of Si-based schemes, recently, alternative semiconductors and semimetals such as TCO (*e.g., ITO*) and 2D materials (*e.g., graphene*) have been employed to demonstrate increased modulation efficiency facilitated by enhanced optical properties of the materials. The materials are capable of exhibiting plasmonic behavior which is the oscillation of free carrier in response to LMI. Plasmonic is beneficial as it facilitates subwavelength field confinement, increased LMI, miniaturization of the

device's footprint, and increased operation speed and bandwidth while suffering from an increased off-state insertion loss [59]

In addition to Pockel's and free carrier schemes, an applied electric field could shift the energy of atoms and molecules containing elliptical electronic states and thus their optical properties giving rise to a phenomenon known as the Stark effect [52,60]. Besides, an applied electric field could potentially shift band edges and thus absorption spectra of bulk semiconductors and dielectrics, a phenomenon referred to as the Franz-Keldysh effect. Moreover, the excitonic states between electrons and holes confined in a multiple quantum well structure (MQW) can be perturbed by reducing the energy of the electron-hole pair and thus red shifting the absorption edge. These phenomena have been used to demonstrate electro-optic and electro-absorption modulators [8,61,62]. Moreover, phase change materials such as vanadium oxide (VO_2) and ternary germanium-antimony-tellurium (GST) compound material also facilitate large refractive index change upon the application of external voltage or temperature utilizing which EOM designs have been proposed [52,63]. However, the reversible phase change mechanism is slow and requires comparatively large energy per bit (fJ/bit) [49].

Each scheme described above has its advantages and disadvantages that need to be evaluated to merit their performance for a particular application in question. For EOM/EAM, several performance metrics have been defined and used to compare different schemes and will be discussed in the following section.

2.9. Performance Metrics

The performance or merit of Electro-Optic and Electro-Absorption Modulators are evaluated based on certain parameters such as Extinction Ratio, Insertion Loss (IL), footprint, Energy-Bandwidth, Speed, Power consumption, etc.

2.9.1. Extinction Ratio

ER also known as Modulation Depth (MD) measures how effectively the modulation scheme affects the light intensity at the output end between a modulator's on and off state. In other words, the difference between light intensities at the output end when a modulator is set to high transmission (HT) and low transmission state (LT) respectively. It is usually expressed in dB units [58,64]. For example, ER of a modulator can be defined by Equation 2.23.

$$ER = -10 \cdot \log(\frac{I_{\max}}{I_{\min}}) \ (dB) \qquad 2.23$$

As a numerical example, a 3 dB ER corresponds to a reduction of light intensity by 50% at a low transmission state compared to the intensity at a high transmission state. ER as high as possible is desirable for long transmission distances but a 4-5 dB ER is sufficient for on-chip interconnect applications [58].

2.9.2. Insertion Loss

Insertion Loss (IL) also known as propagation loss or off-state loss measures the optical loss the light signal suffers as it traverses through the modulating region while the device is not subjected

to any external perturbation (*e.g., voltage*). IL as low as possible is desirable. For example, for a Si rib-waveguide-based modulator, IL can be determined by calculating the mode loss from the imaginary part of the effective mode index derived from the 2D analysis given by Equation 2.24 [64,65].

$$\alpha = 10 \cdot \left| \log\left(e^{-\frac{4\pi}{\lambda}\mathrm{Im}\{n_{eff}\}}\right) \right| \ (dB/\mu m) \qquad 2.24$$

The expression in Equation 2.24 can also be used to calculate ER by determining the difference between mode losses $(\alpha_{ON} - \alpha_{OFF})$ with and without external perturbation respectively. The difference provides ER in dB/µm from which the length (L in µm) of the modulating region can be calculated from the ratio of desired ER (dB) to the ER (dB/µm). Upon calculating the length L, the IL for the modulating region can be calculated from the product of L and α_{OFF}. Apart from the modulating region, losses can also occur from the light propagating through the passive components (grating coupler, taper, waveguide, etc.). However, the losses are minimal compared to the modulating region if the operating wavelength is well below the band gap of the passive waveguide material (*e.g., Si*), smooth and efficient coupling happens between light modes from the passive waveguide to the active modulating region and vice versa.

2.9.3. Electro-Optic and Optical Bandwidth

EO Bandwidth (BW) or speed measures how fast an electrical signal can be encoded onto an optical signal and directly indicates the maximum bit rate that a modulator can support [64]. It is usually defined by the frequency at which a modulator performs a 3 dB modulation given by a

well-known expression as $f_{3dB} = \frac{1}{2\pi RC}$; where R and C refer to lumped resistance and capacitance of the device. On the other hand, optical BW indicates the range of light wavelength a modulator can modulate with satisfactory performance.

2.9.4. Energy Consumption

Energy consumption measures mean energy that is lost per bit [64]. In other words, it quantifies the energy expended in producing each bit of data [58]. It is usually theoretically determined $((1/4)CV^2)$ as opposed to measuring it experimentally. The (1/4) factor is usually used from the probability of writing either bit "1" or "0" which is assumed as 25%. However, the theoretical estimate could deviate from the actual value if non-idealities overcome the over-simplified theoretical model considered [64]. To justify the replacement of electrical on-chip interconnects with their optical counterparts, a modulator must offer energy per bit $\sim 10 fJ\ bit^{-1}$. However, today's servers based on electrical interconnects typically consume $\sim 10-30 pJ\ bit^{-1}$ while MZI-based modulators reported in the literature for optical interconnects consume $\sim 5 pJ\ bit^{-1}$. This emphasizes the potentiality of Si modulators especially the one with an electro-absorption scheme [58].

2.9.5. Footprint

A footprint is the measurement of the area a modulator occupies for appreciable light modulation. To meet the requirements of large integration densities in PICs, a footprint as small as possible is desirable [58,64].

Given the discussion on EAM schemes and the definition of performance metrics in the last two sections (2.8 and 2.9 respectively), Table 2.1 highlights the performance summary of some state-of-the-art EOM/EAMs reported in the literature.

Table 2.1. Performance summary of the state-of-the-art modulators reported in the literature

Device	Modulation (dB)	Insertion Loss (dB)	Energy Consumption (fJ/bit)	Speed (GHz)	Size [μm²]
$LiNbO_3$-based EOM [4]	30	<1dB	0.37	50	20[mm]
Si Micro Ring Photonic [66]	9	1	1	25	25
Si Travelling Wave Photonic [67]	3	4	N/R	25	~1 x 10^6
Organic Polymer Plasmonic [21]	6	9	25	70	10
$Sn:In_2O_3$ Plasmonic (ENZ) [17]	10	16	4*	25	200
Au/In_2O_3 Plasmonic (ENZ) [19]	6.5	10	2.1pJ/bit	~2*	4
Graphene-based modulator [68]	3	N/R	N/R	1.2	25

(N/R represents data not reported. *Values that have been estimated)

2.10. Mode Analysis of Rib and Slot Waveguide for EAM

To modulate light and thus realize an EAM, the corresponding light wave needs to be guided by restricting energy flow to only one direction using structures also known as waveguides. Waveguides are well-known structures that are being used to guide EM waves in the regime such as radio and optical frequencies for a very long time. One prominent example could be optical fiber which has revolutionized the way information is being transferred even across continents.

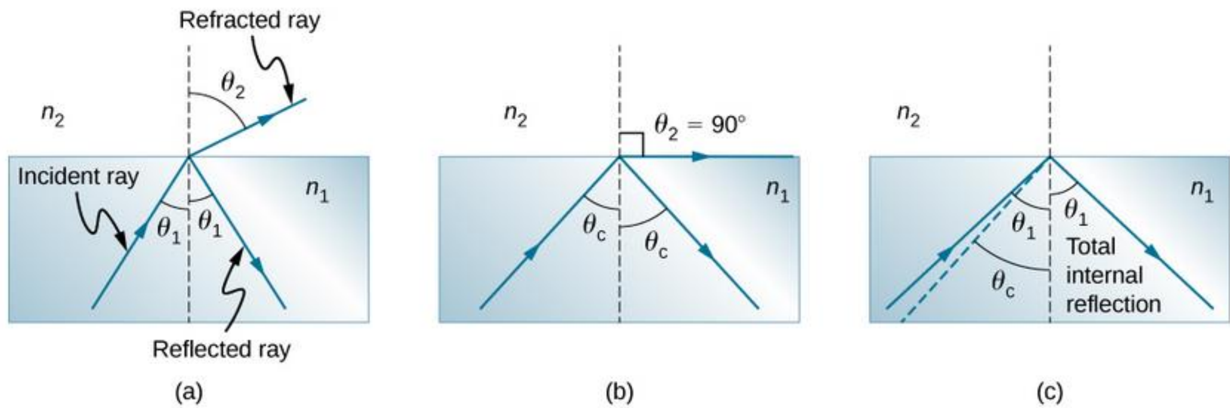

Fig. 2.18: Schematics for the illustration of (a) light propagates from one medium to another medium with distinct refractive indices. (b) Critical angle at the interface that causes light to traverse along the interface with $\theta_2 = 90^0$. (c) Total Internal Reflection of light for $\theta_1 > \theta_C$

Waveguide's function can well be understood by Total Internal Reflection (TIR) from geometrical optics [69]. To illustrate, a ray of light propagating through a medium-1 is incident at an interface between medium-1 and medium-2 where the corresponding refractive indices are n_1 and n_2 respectively as shown in Figure 2.18. At the interface, light could refract into and propagate through medium-2 or reflect into medium-1. If $n_1 > n_2$, the refracted ray will bend away from the normal as in Figure 2.18 (a). The angles and refractive indices are related to each other by Snell's law expressed by Equation 2.25.

$$n_1 \sin\theta_1 = n_2 \sin\theta_2 \quad 2.25$$

The angle of incidence, $\theta_1 = \theta_C$ for which the refracted light traverse along the interface making the transmitted angle $\theta_2 = 90^0$ is called the critical angle as shown in Figure 2.18(b). If $\theta_1 > \theta_C$, the light is reflected into medium-1 and the phenomenon is known as TIR. Utilizing this phenomenon light could be trapped and guided through a high-refractive-index material (*e.g., Si with a refractive index of ~3.48 at 1.55 µm*) surrounded by a low-index material (*e.g., air with a refractive index of 1*). Figure 2.19 shows two types of such configurations namely ridge and rib

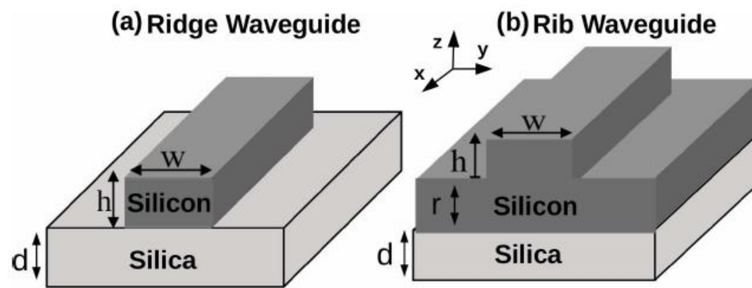

Fig. 2.19: Schematic showing two types of waveguide configuration (a) Ridge and (b) Rib [2].

waveguides on a Silica substrate [2] with air (not shown in the figure) in the surroundings acting as the low-index cladding material. According to the figure, light is confined in the y-z plane while propagating in the x-direction. On the other hand, light could also be guided within a low-index material surrounded by high-index material due to the EM field discontinuity at the interface between high-index-contrast materials as shown in Figure 2.20 [70].

To analyze the performance of a 3D waveguide, it is necessary to identify and understand which types of EM waves are allowed to propagate at a given frequency. The frequencies of waves that

can propagate through a waveguide are referred to as resonant modes. The lowest frequency that could propagate through the waveguide is known as a cutoff frequency or fundamental mode. The propagating resonant modes are dictated by the size (*e.g., width, w, height, h*) and relative permittivity of constituent materials of a particular waveguide configuration. Propagating modes can be fully described by complex-valued propagation constants and spatial distributions of all field components. For example, in Figure 2.19, Transverse Electric (TE) and Transverse Magnetic

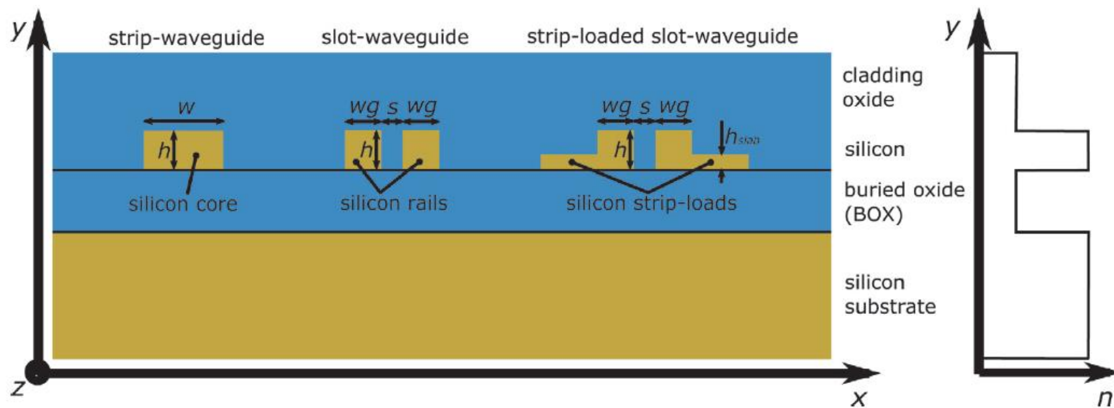

Fig. 2.20: Schematic showing conventional slot and strip loaded Si waveguide. A conventional strip waveguide configuration is also shown to point out geometrical differences. The respective refractive indices of constituent materials are also shown [70].

(TM) modes can be characterized by field components $E_x = E_z = H_y = 0$ and $H_x = H_z = E_y = 0$ respectively. In other words, E_y and H_z components dominate in TE mode while E_z and H_y components dominate in TM mode [2].

To investigate and find such modes, an analysis known as mode analysis could be performed by exciting modes in a 2D transverse cross-section of a waveguide with appropriate boundary conditions while employing the eigenmode solutions to Maxwell's equations. To do so, several

numerical techniques are available such as the two-dimensional beam propagation method, effective index method, finite difference method, and finite element method (FEM) [71,72]. In this research, FEM has been used to find the TE mode necessary to confine light upon biasing MIS structure with the help of ENZ. The analysis utilizes the frequency with the Helmholtz equations for electric and magnetic fields while searching for a solution in the form of a wave traveling in the out-of-plane direction. The Helmholtz equations for electric (*E, V/m*) and magnetic (*H, A/m*) fields are given by the expressions in Equation 2.26(a,b) respectively.

$$\nabla_{\perp}^{2} E + k_0^2 (\varepsilon_r - n_{eff}^2) E = 0 \qquad 2.26(a)$$

$$\nabla_{\perp}^{2} H + k_0^2 (\varepsilon_r - n_{eff}^2) H = 0 \qquad 2.26(b)$$

where, $\nabla_{\perp}^{2} = \partial^2 / \partial y^2 + \partial^2 / \partial z^2$, $k_0 = 2\pi / \lambda_0$ is the free space wave number with λ_0 being the wavelength in a vacuum, ε_r is the relative permittivity of the material in which light is confined, n_{eff} is the effective mode index defined by the expression in Equation 2.27

$$n_{eff} = \frac{\beta}{k_0} \qquad 2.27$$

where, $\beta = 2\pi / \lambda_{eff}$ is the propagation constant that signifies the phase rotation per unit distance. So, from Equation 2.27, the effective mode index can be defined as the ratio of wavelength in the confining medium to the wavelength in a vacuum [73]. Figure 2.21 shows the normalized E-field intensities of TE and TM modes for strip and slot-configured waveguides shown in Figure 2.20 derived from FEM analysis [70]. From Figure 2.21, the difference in EM field distribution or mode

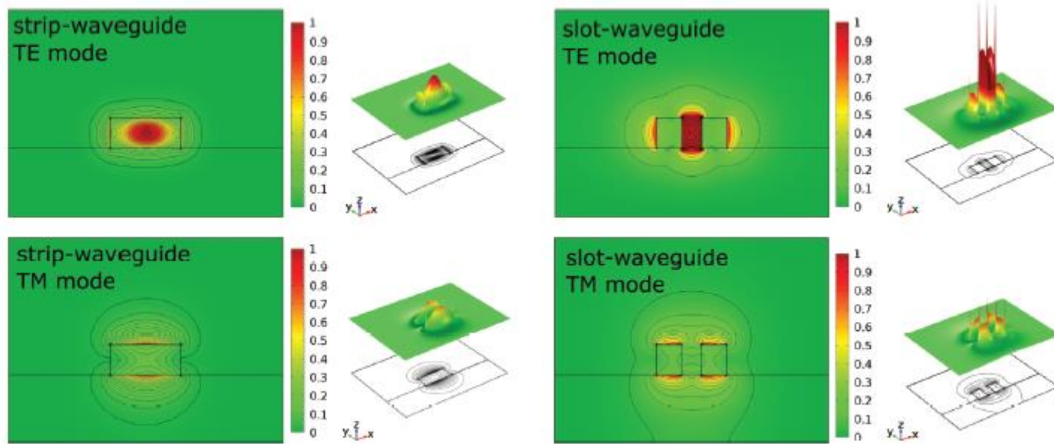

Fig. 2.21: FEM analysis to find TE and TM modes in strip and slot waveguides with operating wavelength of 1.55 µm, substrate and cladding refractive indices of 3.48 and 1.44 respectively [70].

profile for TE mode between strip and slot waveguide is comprehensible. The field is predominantly confined within the high-index material that is diffraction limited in strip configuration (top-left) while the slot waveguide squeezes and confines the mode within the relatively narrow slot containing the low-index material (top-right). This distinct feature of high confinement in slot structure is beneficial as it makes the light more sensitive to refractive index change of the surrounding media compared to strip configuration. In fact, the slot waveguide is more advantageous than the strip one, particularly for sensing applications since a major portion (~70%) of the guided light can be confined near the rails in slot configuration compared to only a minor portion (~20%) in case of strip configuration [70]. In this research, an MIS capacitor structure has been incorporated in both rib and slot configurations and performance comparison has been investigated in terms of EAM performance metrics discussed in the previous section. It will be shown that due to the increased sensitivity, the slot configuration provides better performance compared to its rib counterpart.

3. Introduction and Optimization of EAM

In this chapter, we introduce the modulator design with constituent components and discuss its functionality. The proposed EAM will be optimized by first optimizing the MOS and later the result of which will be incorporated into wave optics analysis. A good portion of the discussion was published as a conference [74] and journal paper [65] and directly copied in this chapter, in the conclusion, and appendices.

3.1 Introduction to Modulator Design

Overviewing the summary presented in Table 2.1 from section 2.9, each scheme has its advantages and disadvantages. For example, EOM that is based on purely manipulating the real part of the refractive index (*e.g., in ref* [4]), though offers low IL with an appreciable ER but falls short in terms of device footprint. On the other hand, plasmon-assisted EAM offers high ER with a small device footprint but at a cost of increased IL (*e.g., in ref* [19]) hindering their practicality for on-chip cascaded operation. That is why this research aims to reduce the IL of a plasmon-assisted EAM utilizing ENZ.

(a) (b)

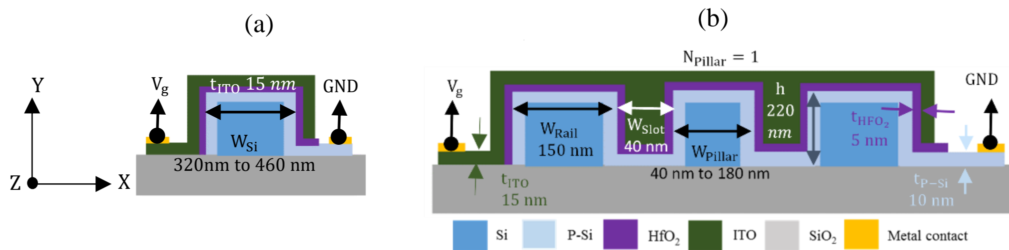

Fig. 3.1. Schematic of (a) Rib and (b) Slot configurations of EAM. For multi-slots N_{Pillar} is the number of Si pillars in the middle of two Si rails. $N_{Pillar} = 0$ corresponds to single slot configuration while $N_{Pillar} = 1,2,3$ correspond to 2, 3 and 4-slot configurations of EAM [65,74].

In this research, rib, single-slot, and multi-slot configurations of EAMs have been analyzed and the performance metrics have been determined for the operating wavelength of 1.55 µm. Figure 3.1(a-b) shows the schematic of rib and slot configuration-based EAM on a Si on Insulator (SOI) substrate respectively. The corresponding dimensions of the constituent layers are shown. Each configuration consists of a MOS that houses the tunable material ITO (green), a thin dielectric oxide, and p-type Si (light blue). In the analysis, ITO and p-type Si has been considered as the contacts. In the rib configuration, light is mostly confined within the Si waveguide. On the other hand, light is mostly confined within the slot(s) (*e.g., between Si rails*) in single (multi) slot configuration. Upon negatively biasing the MOS at the ITO contact (p-type Si being grounded), electrons accumulate at the interface between ITO and dielectric oxide. The real part of the permittivity reduces as the electron concentrations within the accumulation layer increase (according to the Drude model) with the increment of negative applied voltage. An appropriate negative gate voltage could bring the real part of the permittivity close to zero at the operating wavelength facilitating the ENZ phenomenon. This will lead to the confinement of a transverse magnetic (TM) EM field polarized in the x-direction (considering that the EM light field is traveling in the z-direction) to fulfill the requirement of the boundary conditions [43,47]. And thus, the amplitude of the light can be modulated along the z-direction.

3.2: MOS Optimization

In the proposed EAM design, the MOS is an integral part, the optimization of which is crucial for the overall device's performance. Plasmonic EAMs reported in the literature largely make use of

metal as the contact to bias the device [16–21]. Besides working as contact, the metal also supports a hybrid plasmonic-photonic mode which partially pulls the electromagnetic field (EM) out of the silicon and improves overlap with the dynamic layer [19]. Even though this phenomenon is helpful in terms of achieving appreciable ER in the device on-state (*i.e., low-transmission state*), it incurs an undesirable loss in the device's off-state. To combat this, our goal is to utilize ENZ as a means to both confine and modulate, but only when modulation is needed. This is realized through a capacitor structure comprising ITO, a dielectric oxide, and p-type Si as shown in Figure 3.2(a).

Each aspect of the MOS device is considered and optimized in the following sections using the Density Gradient (DG) model within the finite element method (COMSOL Multiphysics). As discussed in section 2.5, this approach provides more accurate accumulation layer carrier profiles than the semi-classical device model [30]. Si is taken as the ground contact and is heavily doped ($p = 1\times10^{17} cm^{-3}$) with a p-type dopant (boron) to reduce series resistance so that an achievable equivalent resistance of ~100Ω or even less can be achieved [19,40]. In particular, the optimization process seeks to achieve the peak modulation while minimizing the base carrier concentration within the ITO layer, so as to minimize the off-state transmission loss of the device. The parameters used in the simulation have been enlisted in Table A1 in appendix I

3.2.1 Selection of Oxide

The first step in the optimization of the MOS structure is to select the oxide material. The rapid progress of CMOS integrated circuit technology has demanded the scaling of Si-based MOS field effect transistors (MOSFET) [75]. However, scaling down by reducing the thickness of the dielectric makes the device susceptible to increased gate leakage currents due to Fowler-Nordheim

tunneling as well as breakdown [76]. To overcome this, high-k dielectrics such as HfO_2, Al_2O_3, Ta_2O_5, etc. have been proposed [77].

For our device, a preferable oxide should be chosen to withstand the dc electric field required to accumulate sufficient electrons within ITO to achieve ENZ condition

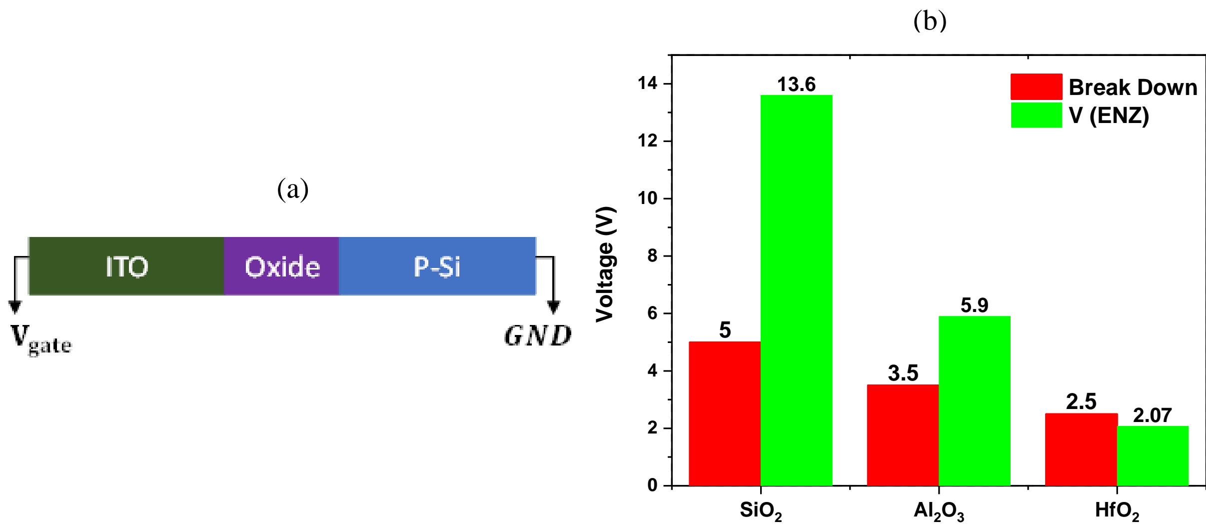

Fig. 3.2. (a) 1D schematic of the capacitor structure [65] (b) Comparison between break down voltage (red bar) and the voltage across the oxides (green bar) to achieve ENZ condition for three different

without breaking down. In this research, the possibility of using HfO_2, Al_2O_3, or SiO_2 has been investigated by considering a thin 5 nm oxide in an ITO/Oxide/Si type MOS structure (Figure 3.2(a)), while the base carrier concentration within ITO is taken as $n = 1\times10^{20} cm^{-3}$. The breakdown voltages for the oxides are reported as 5 MV/cm, 7 MV/cm, and 10 MV/cm respectively [30]. Figure 3.2(b) shows a comparison between the breakdown voltage (red bar) and the voltage, V (ENZ), that applies across the oxide (green bar) to achieve ENZ condition (to achieve a peak carrier concentration within ITO of $\sim 6.5\times10^{20} cm^{-3}$ [19,30]) for all three oxides.

From the figure, HfO_2 having a higher dielectric constant (25 as compared to 9 and 3.9 for Al_2O_3, and SiO_2 respectively [77]) is the only material that is able to achieve this condition within the limit of its breakdown voltage for the base carrier concentration of $n = 1\times10^{20} cm^{-3}$. As a result, the use of Al_2O_3 and SiO_2 would require a larger base carrier concentration in ITO to facilitate reaching the required peak carrier concentration of $6.5\times10^{20} cm^{-3}$ for a smaller applied voltage. However, this is disadvantageous as it would result in increased IL of the device and could produce a reduced loss contrast between the biased and unbiased states. As a result, HfO_2 is selected as the oxide for the MOS structure of the EAM. Besides, it is possible to achieve high conformal growth of HfO_2 by ALD [78,79].

The thickness of HfO_2 has been set to keep at the initial 5 nm because an increased thickness will require an increased operating voltage to achieve ENZ (*e.g.,* $E = V/d$). While this would reduce the capacitance, it would increase the energy consumption and could eventually lead to the need for an applied voltage that exceeds common on-chip 5 V rails. However, the use of a larger spacer layer would be useful in scenarios where device speed is of utmost importance, as a reduced capacitance would facilitate a faster-operating bandwidth.

3.2.1. Optimization of Carrier Concentration in ITO

To further optimize the MOS capacitor, we seek to reduce the carrier density within the ITO (to minimize off-state loss) while still being able to accumulate sufficient carriers under a bias to achieve ENZ, requiring a peak electron concentration of approximately $6.5\times10^{20} cm^{-3}$ for the ITO film taken herein [19,30] as the gate contact. By varying the base carrier concentrations within the

ITO, we observe how the applied gate voltage required to achieve this ENZ condition is distributed throughout various sections of the device (specific material properties used for the simulations are detailed in supplemental information Appendix I). Figure 3.3(a) shows the total voltage applied segmented into the voltage drop across the various sections of the capacitor structure. Considering the contacts, the voltage drop within the ITO is reduced (~0.44 V) as the carrier concentration is increased due to the improved conductivity. This is beneficial as the voltage across ITO is essentially lost energy in the system. However, this reduction is partially counteracted by the

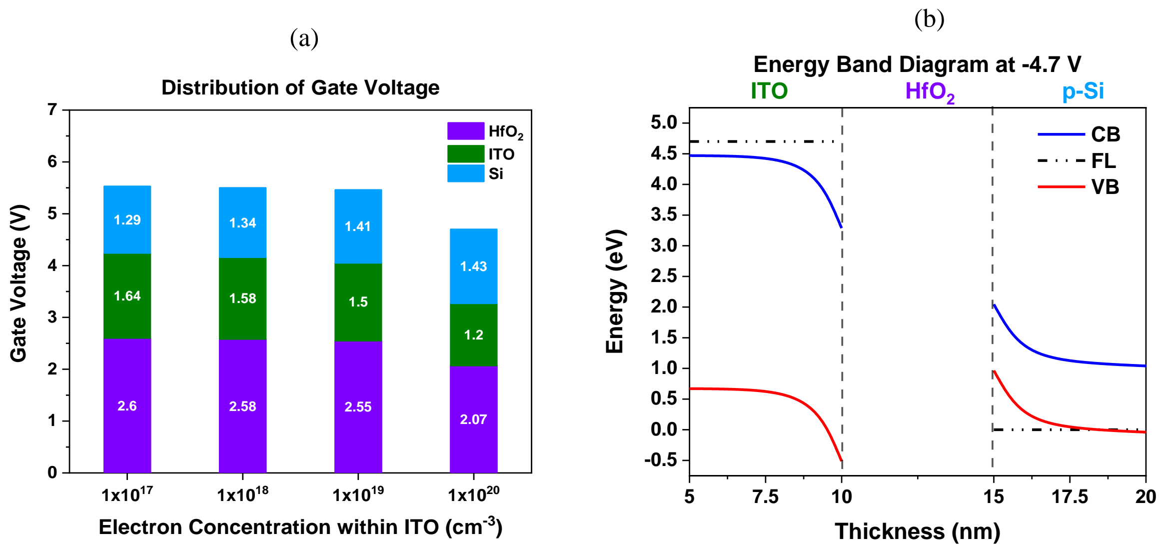

Fig. 3.3. (a) Distribution of gate voltage across various section of capacitor structure. Voltage drops across Oxide, ITO, and p-type Si. (b) Energy band diagram of the optimized MOS structure at a gate voltage of -4.7 V. The oxide has been defined as a "charge conservation" layer [65].

increased voltage drops within Si (~0.14 V), with increased ITO doping. Finally, a reduction in the voltage drop across the 5 nm HfO_2 is observed with higher concentrations, largely due to the ability to apply a smaller voltage (-4.7 V as compared to -5.53 V) to achieve ENZ. This is key to successful operation because the typical breakdown voltage of HfO_2 is 2.5 V per 5 nm (5

MV/cm [30]), requiring carrier concentrations in the ITO > $0.2\times10^{20}cm^{-3}$ to achieve ENZ without breakdown in our structure. Further doping of ITO could be employed to reduce the required voltage and move further away from the breakdown. However, as noted this will bring the unbiased ENZ condition closer to the operating wavelength, resulting in an increased off-state loss (according to the Drude model). As a result, we select a base carrier concentration of $n=1\times10^{20}cm^{-3}$ to keep the applied voltage below 5 V and remaining below the breakdown of the 5 nm HfO_2.

3.2.2. Results and Discussion

Figure 3.3(b) shows the energy band diagram of the final capacitor structure at a gate voltage of -4.7 V derived using the optimized parameters for the MOS structure. Figure 3.4(a-b) shows the electron and hole concentration within ITO and p-Si for several gate voltages illustrating the ability to achieve ENZ conditions within the ITO for an applied bias of -4.7 V. We note that the value of the DG effective mass of electrons in ITO was determined by comparing DG and Schrödinger-Poisson (SP) model (See supplemental information Appendix II) [32,34].

Given the analysis of the capacitor structure, a carrier concentration of $1\times10^{20}cm^{-3}$ and application of -4.7 V bias is suitable for achieving ENZ within the limits of dielectric breakdown for realistic ITO films with a mobility of 40 cm^2/V.s [39]. However, as is clear from Figure 3.4(c-d), this manifests in a layer with a minuscule thickness (< 1 nm). As a result, it can be considered as a 2D surface, and the overall ER of the modulator is considered as proportional to the ENZ surface area. On the other hand, as the volume of ITO increases, a higher percentage of the total

EM field will traverse the lossy ITO material as compared to low-loss Si and HfO_2, thus increasing IL. Therefore, the key metric of ER/IL can be considered as proportional to the ENZ surface-to-TCO volume ratio (SVR) for a given mode shape.

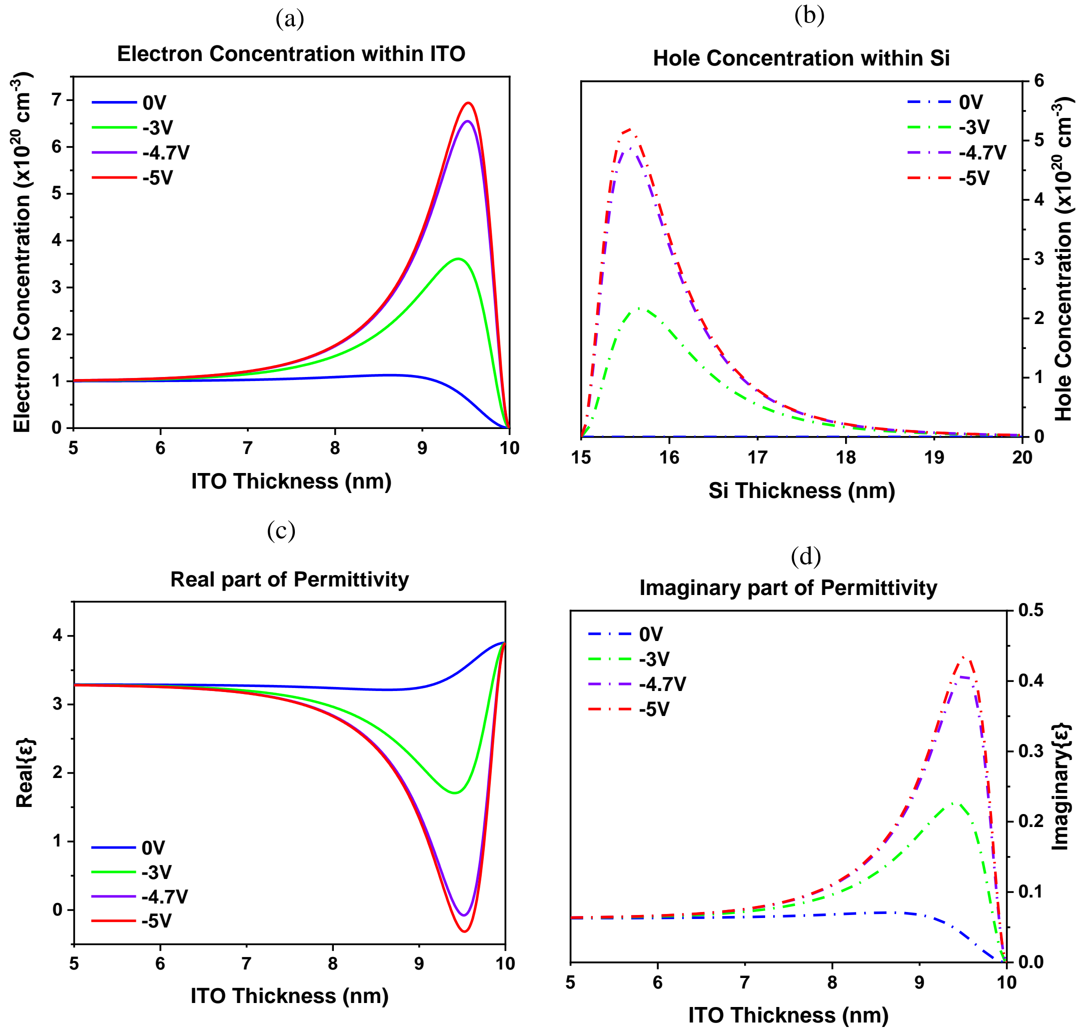

Fig. 3.4. (a-b) Electron and Hole concentration within ITO and p-type Si as a function of gate voltage. The bulk hole carrier concentration within p-type Si is $1\times10^{17}cm^{-3}$ (c-d) Real and Imaginary part of permittivity within ITO as a function of gate voltage and ITO thickness [65].

3.3. Optimization of Electro-Absorption Modulator

As discussed in section 3.2, a thin layer of ENZ is achievable from the MOS configuration treating ITO as both the gate and tunable material. This should facilitate light modulation guided by a waveguide that is covered by the MOS structure. The carrier profile for the MOS layers (ITO and p-Si) reported in the previous section (figure 3.4) has been extracted from 1D numerical

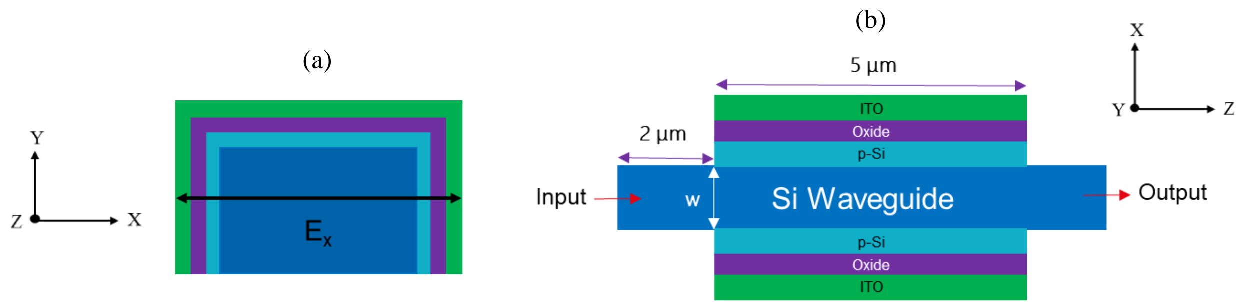

Fig. 3.5. Schematic of cross-sectional view of rib-based Si waveguide with MOS structure (a) in the X-Y plane to determine 2D carrier distribution. The false colors indicating individual layers are marked in fig. (b) in the X-Z plane to evaluate performance metrics and FOM.

analysis. However, the carrier profile in a real device will be three-dimensional. Determination of 3D carrier distribution by simulating a 3D MOS structure, and later coupling the results into a 3D waveguide for the investigation of optical modulation is computationally expensive and time-consuming, especially with a Finite Element Method where mesh size should be a fraction of wavelength in interest [70]. Rather, a 2D cross-sectional view in the X-Y plane is helpful to get the carrier distribution and then mimic the distribution in the Z-direction. For example, Figure 3.5(a) shows a 2D cross-sectional view (X-Y plane) of Si rib-based EAM covered with the optimized MOS structure. Air has been assumed as the surrounding cladding layer (not shown in the figure). An EM light wave with the Poynting vector into the Z-direction will be mostly confined in the Si waveguide with TE mode evanescent field leaking into the MOS and surrounding air

cladding along the X-direction. This TE mode of the EM field (E_x) can be perturbed by introducing ENZ layers upon biasing the MOS structure. On the other hand, light modulation could be inspected by analyzing a cross-sectional view of the EAM at the X-Z plane as shown in Figure 3.5(b). That is why first, a 2D analysis of a MOS structure has been performed to determine 2D carrier distribution. Later, a cross-sectional view of a Si rib-based EAM covered with MOS structure in the X-Z plane has been numerically analyzed to determine performance metrics and Figure of Merit (FOM).

3.3.1. 2D Carrier Distribution in MOS

Figure 3.6(a) shows the 2D carrier distribution in the optimized MOS structure comprising ITO,

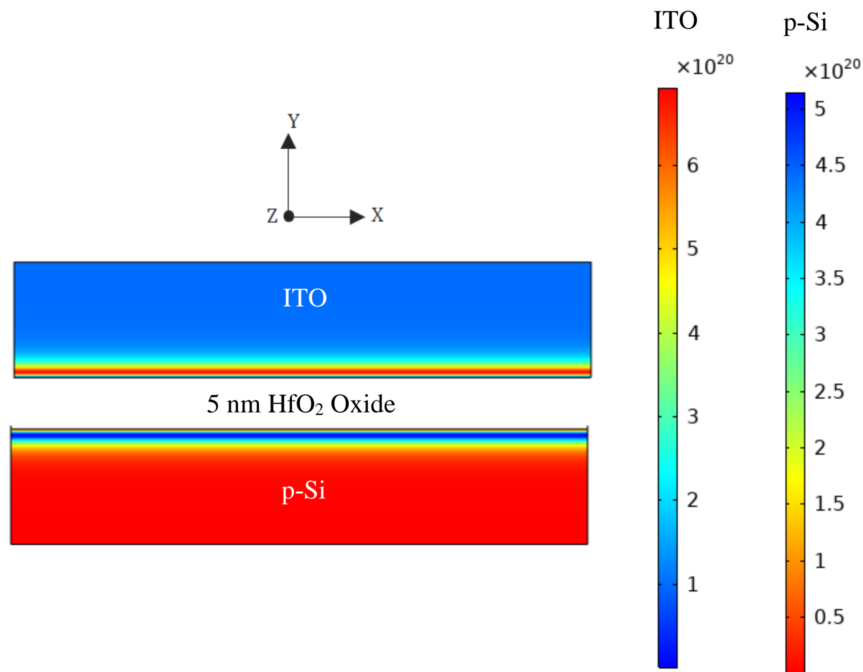

Fig. 3.6. 2D carrier distribution in the optimized ITO/HfO_2/p-Si MOS configuration. The corresponding color bars (unit in cm^{-3}) and the orientation of the MOS are also shown.

HfO_2, and p-Si. The analysis has been performed using the semiconductor module available in the Finite Element Method COMSOL Multiphysics. The polarity of the applied voltage at the ITO and the p-Si end is -5V and 0V respectively (The parameters used in the simulation have been enlisted in Table A1 in Appendix I).

3.3.2. Performance Analysis of a 2D Cross-Sectional EAM

Determining the 2D carrier distribution, the spatial distribution of electrons in ITO has been incorporated into the Drude equation in the wave optics analysis to define the spatial variation of permittivity within ITO. As shown in Figure 3.5(b), the length of the MOS section that covers the Si waveguide and the waveguide itself is 5 and 9 μm respectively. *w* is the width of the Si waveguide and has been assumed as the variable parameter considering that the smaller the value the higher the evanescent field interacts with the MOS. To investigate the optical modulation,

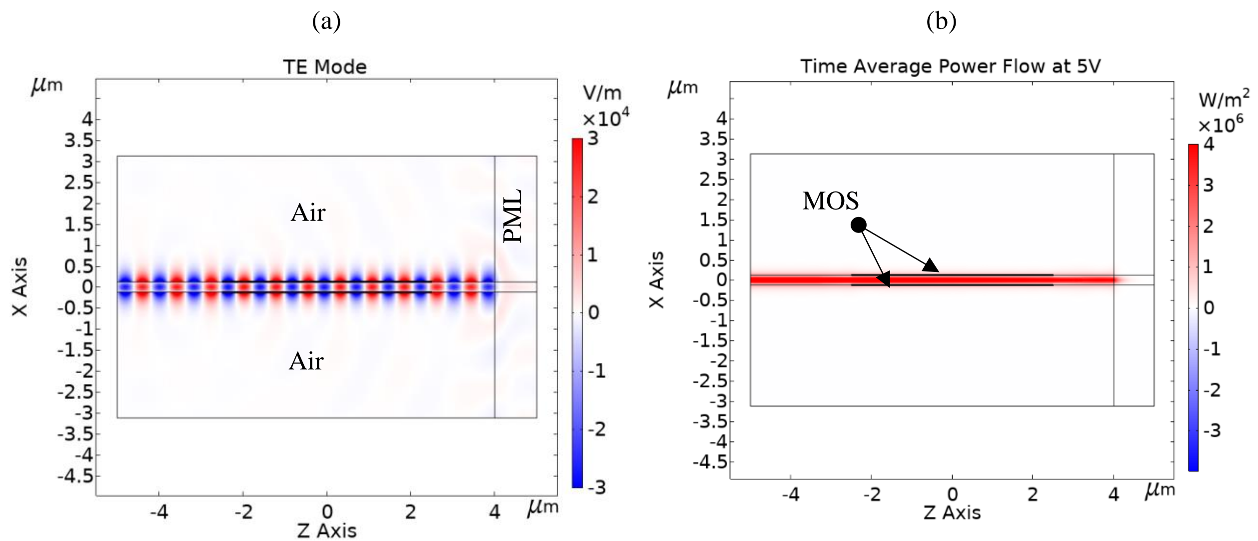

Fig. 3.7. Cross sectional analysis of the EAM with *w* = 240 nm (a) The X-component of the EM filed propagating in the Z direction. The air and PML layer have been indicted. (b) Time average power flow into the Z direction at 5V applied voltage.

Boundary Mode Analysis available in the wave optics module has been applied while defining a port at the input end to inject the appropriate TE mode into the waveguide. A thick Perfectly Matched Layer (PML) of thickness 1 μm has been defined at the output end (not shown in the figure) to overcome impedance mismatching and thus prevent spurious reflections at the output end boundary. A scattering boundary condition has been imposed on all outer boundaries except the input end where the port is defined. Figure 3.7(a) shows the TE mode (E_x) of the propagating EM field at 0V. Figure 3.7(b) shows the time average power flow of the TE mode into the Z-direction. The modulator total loss at a particular voltage has been calculated using Equation 3.1.

$$Total\ Loss_{V_g} = 10 \cdot \log(\frac{P_{Avg-Out}}{P_{Avg-In}}) \quad \text{(dB)} \qquad 3.1$$

where $P_{Avg\text{-}In}$ and $P_{Avg\text{-}Out}$ are the average power at the input and output end of the Si waveguide at a particular voltage. The total loss defined here has been assumed to include IL as well as any other losses due to reflection, refraction, scattering, absorption, etc. as light traverses the guiding layer. The ER has been calculated by taking the difference between total losses corresponding to applied voltage -5V and 0V respectively. This research has aimed to achieve an ER of at least 6 dB with an IL of less than 1 dB. To quantify we define a Figure of Merit (FOM) as given in Equation 3.2 requiring a value of ≥ 6.

$$FOM = \frac{Modualation\ Depth(\geq 6dB)}{Insertion\ Loss(\leq 1dB)} \qquad 3.2$$

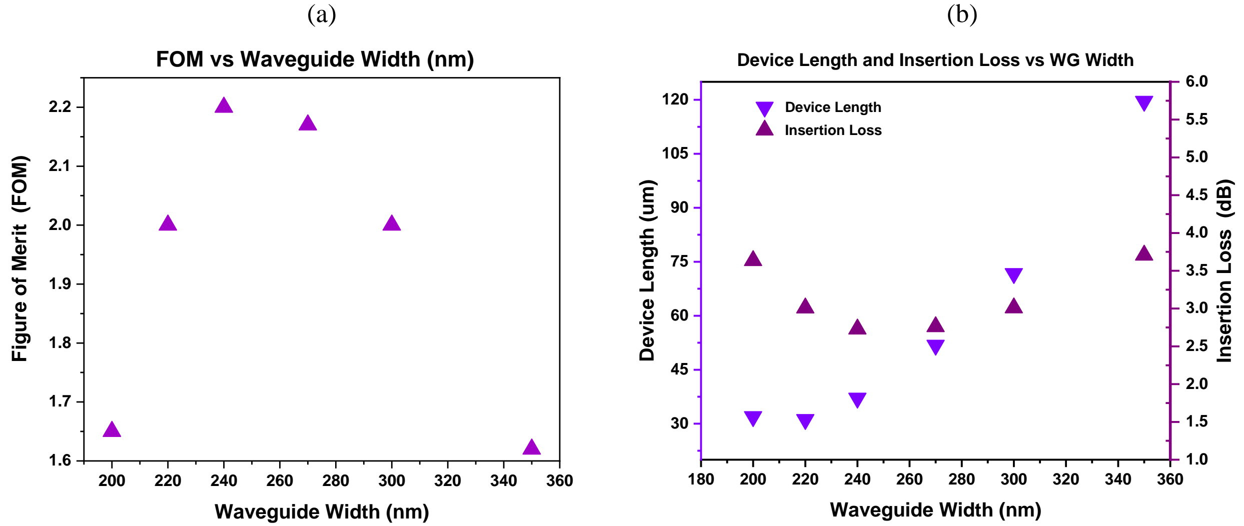

Fig. 3.8. Cross sectional analysis of the EAM with wide range of waveguide width (a) FOM as a function of waveguide width. (b) Device length and Insertion loss showing relatively poor performance of rib-based configuration.

Figure 3.8(a) shows the FOM as the function of waveguide width. According to the figure, the current configuration performs poorly for a wide range of waveguide width, even the best device with a width, $w = 240\ nm$ requires a length of >30 μm to reach 6 dB modulation, resulting in an IL of ~2.7 dB as shown in Figure 3.8(b). This performance is inferior compared to state-of-the-art plasmon-assisted EAMs reported in the literature [9,19,40,80].

3.3.3. Introduction to Surface-to-Volume Ratio

The analysis of the cross-sectional Si rib-based waveguide and the corresponding poor performance indicates that the minuscule thickness of ENZ is not enough to extract the light that is mostly confined within the higher index Si waveguide. This provides two primary conclusions: First, the ENZ layer can be considered as a 2D surface due to its minuscule thickness (<1 nm), and as the ENZ layer facilitates light confinement, the overall ER of the modulator can be considered

as proportional to the ENZ surface area. So, an increase in ENZ surface area is expected to improve FOM. Second, poor performance predominantly occurs due to the poor overlapping between the mode and the ENZ layer. While this can be improved by confining light within the TCO layer, this will result in more energy propagating through the lossy TCO layer, resulting in an increased IL. Thus, a minimal overall amount of TCO is desired (*e.g., minimal volume*). For example, the ideal scenario where light is mostly confined within ENZ layers necessitates confining light within the TCO material (*e.g., in this case, ITO*) that generates the ENZ. As the volume of ITO increases, a higher percentage of the total EM field will traverse the lossy ITO material in the off-state compared to low-loss Si and HfO_2, thus increasing IL. These two conclusions further indicate that the key metric of ER/IL can be considered proportional to the ENZ surface-to-TCO volume ratio (SVR) for a given mode shape [74].

3.3.4. Performance Comparison between Rib and Slot Configuration

To verify the concept of SVR discussed in the previous section, a comparison between the performances of a traditional rib waveguide and a slot waveguide has been made, the schematics of which have been shown in Figure 3.1(a-b) in section 3.1. Figure 3.9(a-b) shows the ER (dB/μm) (black curve) and IL (red curve) incurred for modulation of 6 dB in the case of a rib and single slot configuration, respectively, versus the rib width and Si-rail width. For simplicity, the 2D analysis for the difference in performance between the rib and slot structure can be expressed by the following overlap integrals of ER and IL as shown in Equations 3.3(a-b):

$$ER = \left. \frac{\iint E \cdot ENZ\, dxdy}{\iint E\, dxdy \iint ENZ\, dxdy} \right|_{V=-4.7V} \qquad 3.3(a)$$

$$IL = \left. \frac{\iint E \cdot TCO\, dxdy}{\iint E\, dxdy \iint TCO\, dxdy} \right|_{V=0V} \qquad 3.3(b)$$

For ER, the figure considers the normalized overlap between the electric field of the optical mode and the cross-sectional area of the thin ENZ surface, reaching unity when the electric field is entirely confined within the ENZ region. Similarly, the IL can be expressed as the normalized

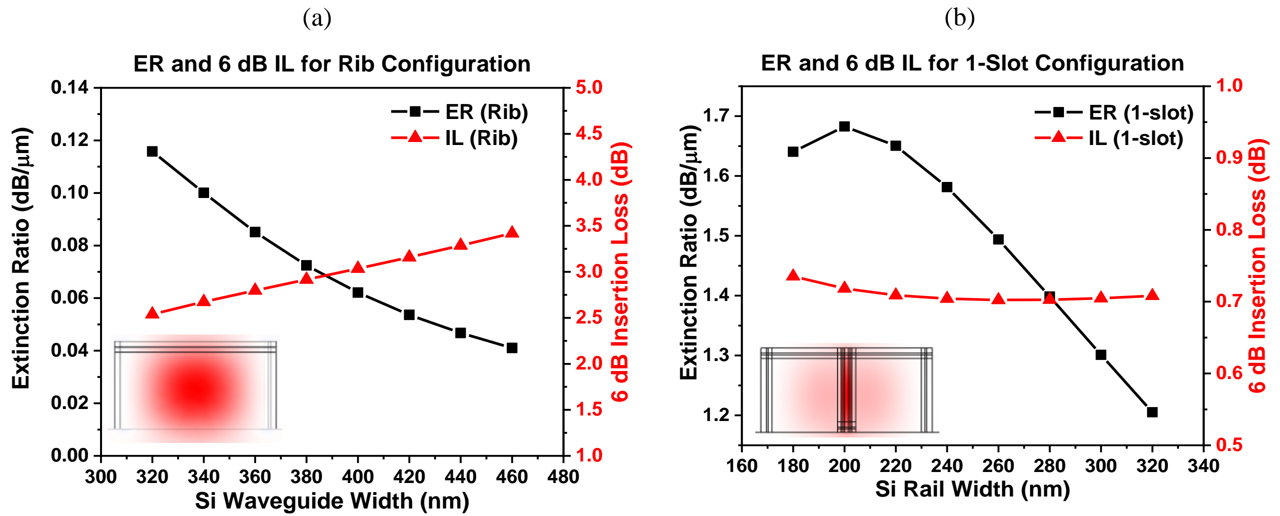

Fig. 3.9. ER (dB/μm) (black) and IL for 6dB modulation (red) for (a) rib and (b) single slot configuration respectively. The slot width is 40 nm [65].

overlap between the electric field of the optical mode and the cross-sectional area of the entire TCO (under the assumption the loss within the Si is negligible). So, the FOM can be expressed as the ratio of equations 3.3(a-b) as shown in Equation 3.4:

$$FOM = \frac{\iint E \cdot ENZ\, dxdy}{\iint ENZ\, dxdy} \times \left(\frac{\iint E \cdot TCO\, dxdy}{\iint TCO\, dxdy} \right)^{-1} \quad 3.4$$

which describes the ratio of the normalized field within the dynamic ENZ region able to be modulated, to the normalized field within the lossy TCO layer. For a mode shape that remains roughly constant, the first term can be increased by enlarging the ENZ layer, or surface, while the latter term can be reduced by shrinking the volume of the TCO (*i.e., increasing the SVR of the geometry*).

Additionally, modification of the electric field spatial distribution may also be used to improve the FOM by confining light near the ENZ region (*i.e., confinement*). However, since the ENZ region is within the TCO, this action will invariably increase the overlap with the TCO as well. As a result, a simultaneous reduction in the volume of the TCO should be applied. The practical limit to this scaling is due to fabrication limitations and the ability to create many thin, parallel, ENZ

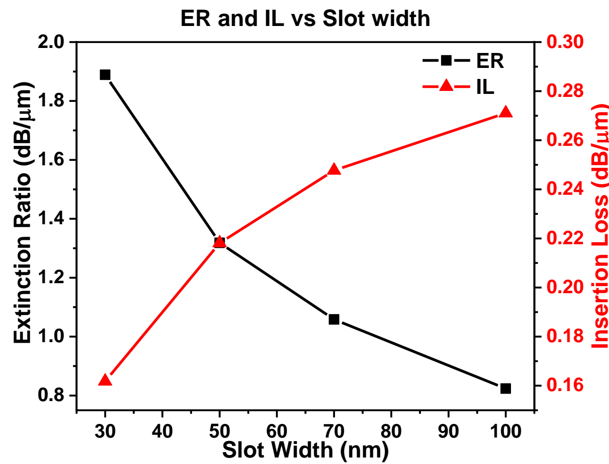

Fig. 3.10. ER (dB/µm) and IL (dB/µm) for single slot configuration as a function of slot width shows increasing loss with increasing slot width containing ITO. The rail width is fixed and equal to 200 nm for single slot configuration [65].

surfaces with small volumes within the spatial region of the mode. For the rib, the light remains mostly confined within Si irrespective of the rib width and ITO thickness (time average power flow in the Z direction at 0 V, inset of Figure 3.9(a)). While this provides reasonably low IL in dB/µm, the ENZ layer alone is insufficient to extract the electric field from the rib to achieve strong mode overlap and modulation. This results in a low ER in the case of the rib configuration, requiring a longer device to achieve appreciable modulation (*e.g., 70.48 µm for 6 dB ER with a Si waveguide width of 360 nm*).

The slot configuration improves upon this primarily by affecting the spatial confinement of the mode and thereby improving its overlap with the dynamic ENZ layer (time average power flow in the Z direction at 0V, inset of Figure 3.9(b)). However, the gains are minimal if the volume of the TCO remains large (*e.g., slot widths > 100 nm*), Figure 3.10. Thus, a reduction in the volume of the TCO is enforced by reducing the slot width, significantly improving performance by reducing the volume of the TCO while maintaining a strong spatial overlap with the ENZ surface. This scaling is limited by fabrication constraints for lithography and etching. Here, an aspect ratio of ~5:1 [81] has been chosen, thus setting W_{slot} equal to 40 nm for a silicon layer of 220 nm thickness for all subsequent configurations. A potential fabrication procedure for the proposed device is outlined in Appendix III. In the following analysis, unless otherwise stated, the only variable parameter is the width of the Si waveguide, rail, and pillar for the rib, single, and multi-slot configurations respectively indicating the fact that the increasing trend of Si content in the device geometry decreases the percentage volumetric content of the TCO.

3.3.5. Performance of Multi-Slot Configuration

Following the discussion from the previous section, the SVR may be pushed higher by inserting more ENZ layers, achieved through a multi-slot waveguide. Figure 3.11(a) shows the comparison among 2 to 4-slot configurations in terms of ER (dB/μm) and IL assuming a length needed to achieve an ER of 6 dB. The 4-slot configuration having a higher ENZ surface area provides higher ER (2.62 dB/μm) while the respective 6 dB IL remains almost steady (~0.7 dB). To compare single to multi-slot configurations, we consider the ratio of ER (dB/μm) and IL (dB/μm) as the FOM and select structures that have a real part of the effective mode index equal to 2 to allow for efficient coupling of light to and from a typical Si rib waveguide [82]. In this case, the single slot has a rail width of 220 nm, the 2 to 4-slot structures have Si pillar widths of 180 nm, 120 nm, and 100 nm, respectively, and the slot width remains fixed at 40 nm for all structures. Figure 3.11(b) shows the comparison in terms of the FOM and active ENZ surface area to TCO volume ratio. Here the TCO

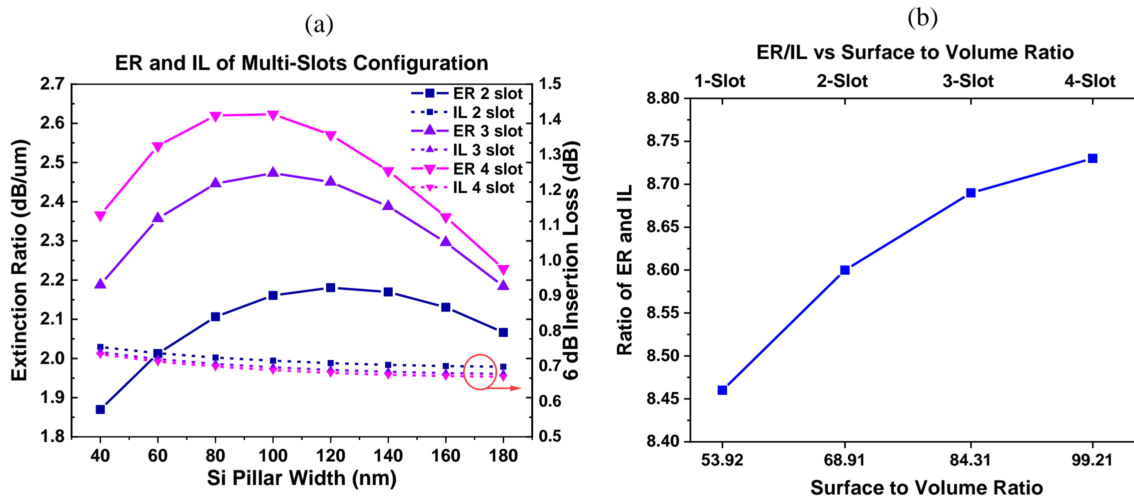

Fig. 3.11. (a) Comparison of multi-slots configurations with respect to ER (dB/μm) and 6 dB IL (b) FOM (ER/IL) as a function of the total ENZ surface area to TCO volume ratio shows improved performance from single to multi-slot configurations [65].

volume for all structures has been expressed as a percentage of the total device volume to account for the increase in the size of each structure. Our study indicates that increasing the ENZ surface area from single to multi-slot configuration improves performance, where the 4-slot structure has a FOM of 8.73 which is better than previously reported plasmonic and hybrid plasmonic modulators (e.g., 4.51, 7.1) [9,19,40,80,83,84]. The FOM for multi-slot structures can further be improved by increasing overlap between the optical mode and ENZ region through optimizing the geometrical parameters (*e.g., by reducing* W_{Slot}*, and optimizing the rail and pillar widths*). However, this will change the corresponding effective mode index leading to a more challenging optical coupler design [82,85]. The mode profile at 0V, the effective mode index, and field confinement at device ON and OFF state for the final optimized 4-slot EAM have been presented in supplemental information Appendix I.

3.3.6. Tradeoffs associated with Surface-to-Volume Ratio

While the approach to improve the ER to IL FOM can be optimized through the SVR and confinement approach, it is also inexorably linked to the speed and energy consumption of the device. To investigate this relationship, we estimate the resistance (taking 6 x 10^{-4} Ω.cm as the resistivity of ITO valid for a carrier density of 1 x 10^{20} cm^{-3} [86] and capacitances of the four configurations corresponding to Figure 3.11(b). Assuming a need for 6 dB modulation, the resistances ($R = \rho L/A$) for single and 2 to 4 slots EAMs are 160 Ω, 274 Ω, 410 Ω, and 536 Ω respectively. Similarly, the estimated capacitances ($C = (\varepsilon_0 \varepsilon_r A)/d$) are 235 fF, 254 fF, 273 fF, and 310 fF respectively. Figure 3.12(a) shows the corresponding RC-limited device speed ($f = 1/(2\pi RC)$) and energy consumption ($U = (1/4)CV^2$) and a comparison with other state-of-

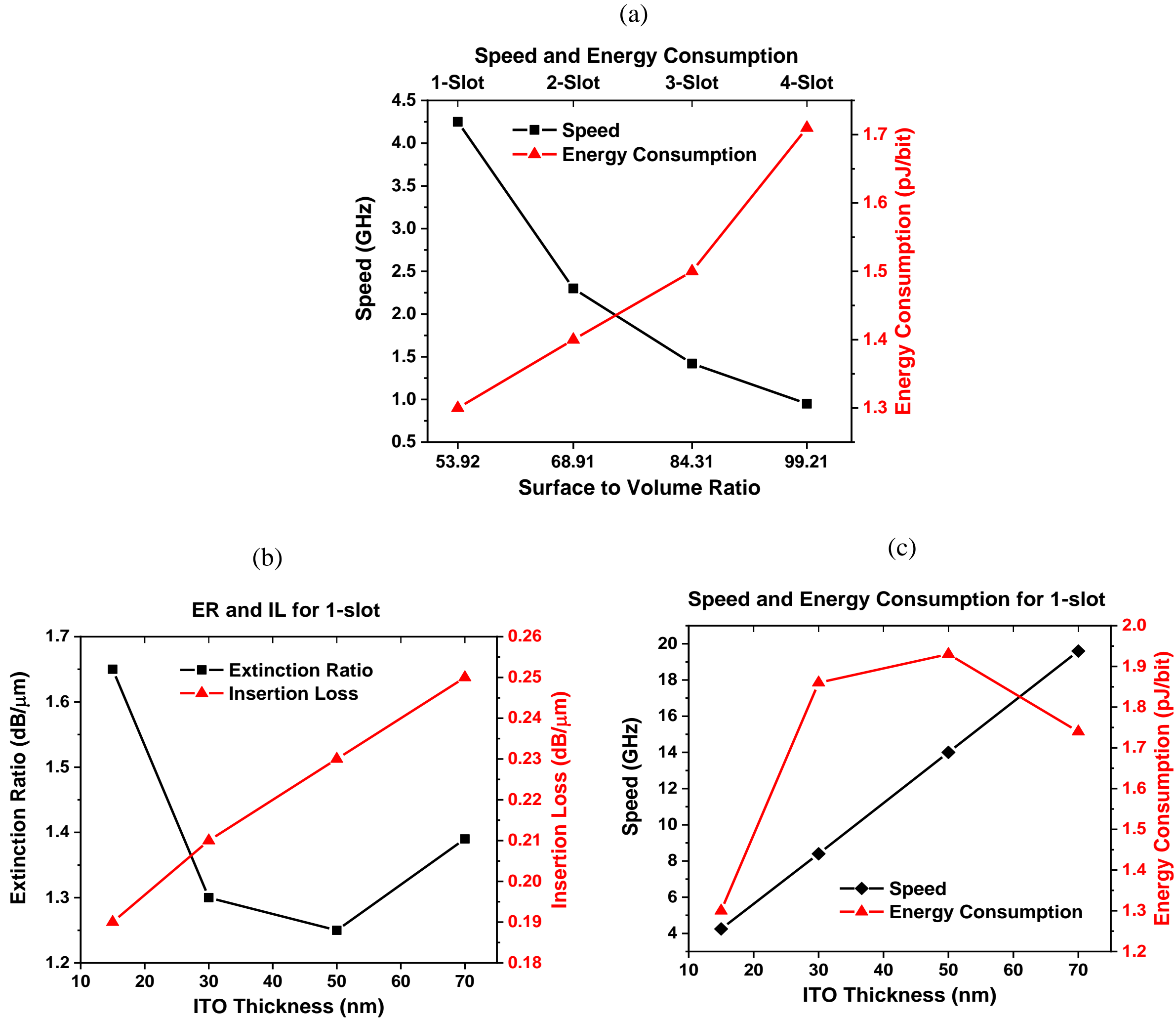

Fig. 3.12. (a) The speed and energy consumption of the slot waveguide designs, illustrating a trade-off in terms of device operation speed and energy consumption. (b) ER and IL and (c) Speed and Energy consumption for 1-slot configuration respectively as a function of the top ITO contact thickness, outlining an approach to mitigate these issues if constraints on IL and driving voltage are relaxed. The 15 nm device was biased at -4.7 V while the other structures were biased at -5.0 V, required to achieve a comparable peak accumulation density within the slot region. The slot width remains same for all cases [65].

the-art modulators reported in the literature is presented in Appendix IV. Overall, a greater than 10x reduction in the IL can be seen, when compared to other plasmonic-style designs, while

maintaining appreciable ER (6 dB) and size (~6 μm^2). However, the speed and energy consumption of the devices are negatively impacted.

This decrease in speed and increase in energy consumption is a result of the increase in resistance and capacitance of the structures which results from the goal to minimize IL, thereby prioritizing a large area and thin ITO layer. This can be mitigated in several ways: 1) by increasing the thickness of the dielectric spacer, 2) by increasing the thickness of the ITO layer, and 3) by increasing the base carrier concentration of the ITO if one relaxes the constraints on the acceptable IL and driving voltages. For example, Figure 3.12(b-c) illustrates that by increasing the thickness of the ITO layer for the single slot design, the speed can be increased to 20 GHz while maintaining similar energy consumption if one can tolerate a moderate increase in the IL of the device (1.07 dB IL for a 6 dB modulation depth). We note that the decrease in ER for the thicker films is due to variations in the mode overlap primarily with the ENZ regions on the outermost edges of the waveguide and further optimization could improve this value. Ultimately, it is clear that the typical tradeoff between energy and bandwidth remains [87], and each structure should be optimized for the specific requirements of the application at hand, considering the relative importance of speed, energy consumption, loss, and size. Nonetheless, the TCO-enabled plasmon-assisted approach allows for the realization of a fully solid-state, non-resonant, compact, robust, and low-loss device for integrated photonics.

4. Material Growth and Characterization for the Optimized EAM

This chapter discusses the optical and electrical properties of as-deposited materials that form the MOS structure. ITO and oxides have been deposited by atomic layer deposition (ALD) and characterized by spectroscopic ellipsometry. So, a brief introduction to ALD and SE will be provided in sections 4.1 and 4.2. The chapter also discusses the process necessary for performing p-type doping of Si.

4.1. Basics of Atomic Layer Deposition

Atomic Layer Deposition (ALD) is a thin film technique where the constituent materials are in the form of a vapor phase during the deposition. This technique was first introduced as atomic layer epitaxy (ALE) in 1977 through the demonstration of ZnS film growth for flat panel displays [88]. ALD has been demonstrated as a promising technique with advantages over other techniques such as physical vapor deposition (PVD) and chemical vapor deposition (CVD) that cope with the ongoing requirement of device miniaturization in both the semiconductor industry and research [89]. For example, PVD that relies on physical processes does not necessarily result in a strong chemical bond between the grown film and the substrate, hence increasing the chance of delamination. On the other hand, even though CVD involves chemical reactions, this may not directly involve the substrate surface. Unlike these techniques, ALD facilitates strong chemical reactions on the substrate surface by which chemical bonds form between the substrate and the film and within the film itself as the film grows [90]. The beneficial aspect of ALD could be justified by its features such as cyclic, self-limiting, and the ability to produce pin-hole-free

controlled growth of conformal thin film at low temperatures [89,91]. The term “thin” is used in the sense that the technique is capable of growing films with thicknesses ranging from 1 nm to several hundreds of nanometers. As an example, Figure 4.1 schematically shows a basic cyclic nature of an ALD technique for the growth of a thin film, “A-B”.

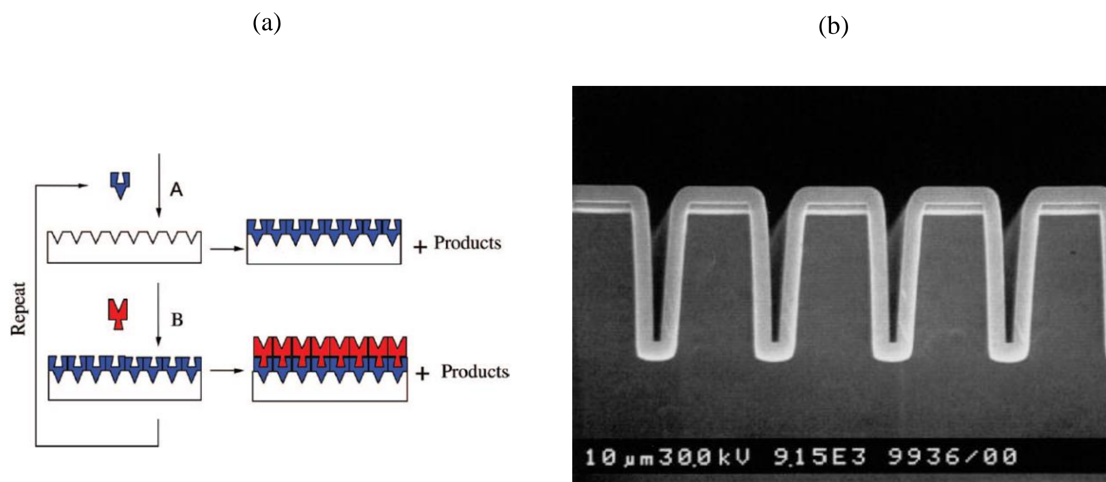

Fig. 4.1: (a) Schematic showing cyclic nature of ALD growth process involving two precursors “A” and “B” for the growth of the film “A-B”. (b) Cross-sectional SEM image showing excellent conformal growth of Al_2O_3 on a high-aspect ratio Si trench [89].

A substrate that is placed inside a reactor (not shown in the figure) within which optimized set temperatures could be maintained, for example, the substrate and the reactor wall temperatures, necessary for the optimal growth of a thin film. A gaseous precursor “A” is pulsed into the chamber for a certain amount of time (t_A) that chemisorbs on accessible sites on the substrate while the precursor ideally does not react with itself manifesting the self-limiting nature of the ALD. The time a process allows a precursor to become chemisorbed on the substrate surface is referred to as chemisorption time, t_{A-Chem}. Once no accessible sites are available on the substrate, the substrate

is considered saturated, and the reaction stops. In this process, by-products are generated that are purged away under vacuum conditions by an inert gas (*e.g.,* N_2, *Ar*). In the next step the second precursor, "B" is pulsed into the chamber that chemisorbs for a certain period (t_B) on the accessible sites generated by precursor, "A" in the previous sub-cycle. Similarly, the process is followed by the corresponding chemisorption time t_{B-Chem} and the purging for the removal of by-products. At this stage, a binary layer A-B is formed and could be considered the first cycle for the growth of the "A-B" film. This layer-by-layer self-limiting growth ensures that the reactions in each sub-cycle are driven to completion and fill every accessible site resulting in continuous, smooth, conformal, and pin-hole-free film on the substrate. In fact, excellent conformal growth of Al_2O_3 even on the high-aspect-ratio Si trench has been reported in the literature as shown in Figure 4.1(b).

The pseudo-precursors described in Figure 4.1(a) could be applied to any practical precursors. For example, Tri-Methyl-Aluminum (TMA) (Al $(CH_3)_3$) and water (H_2O) are widely used as the precursors for Al and O_2 respectively for the growth of Al_2O_3 as shown in Figure 4.2(a) [92]. The TMA once is pulsed into the chamber, the methyl groups ($-CH_3$) on the TMA react with the hydroxyl groups on the substrate according to the following reaction.

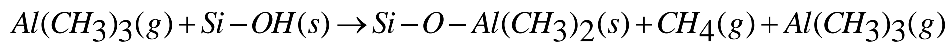

$$Al(CH_3)_3(g) + Si-OH(s) \rightarrow Si-O-Al(CH_3)_2(s) + CH_4(g) + Al(CH_3)_3(g)$$

The TMA does not chemically react with the chemisorbed TMA maintaining the self-limiting feature of the ALD process. The by-products (CH_4 and Al $(CH_3)_3$) are removed in the purging step by an inert gas (*e.g.,* N_2) and the substrate is left with methyl groups of the chemisorbed TMA. In the next step, H_2O is pulsed into the chamber that reacts with the methyl groups of the chemisorbed

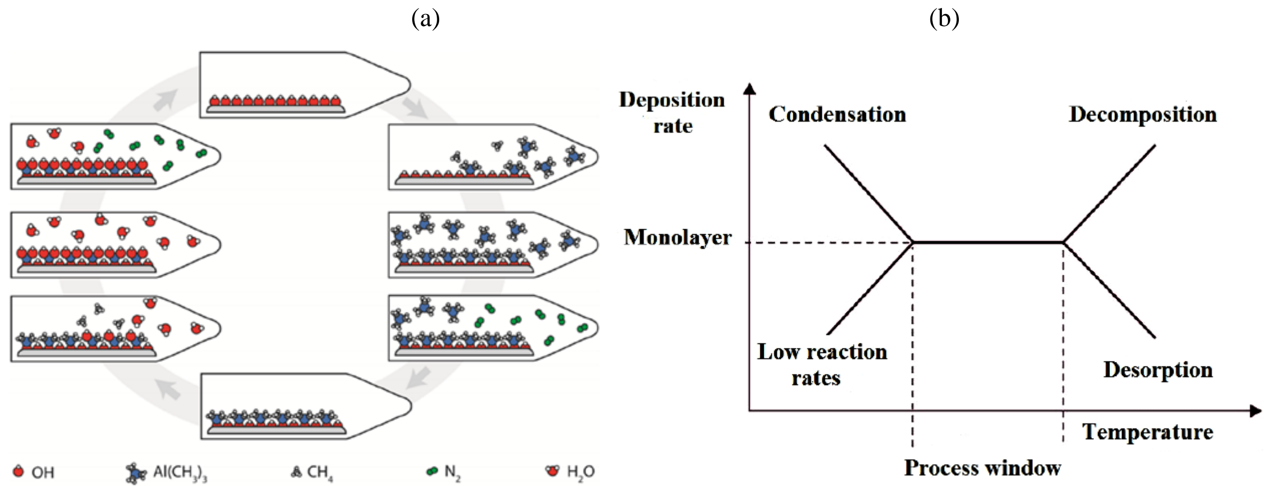

Fig. 4.2: (a) Growth of Al_2O_3 using ALD with TMA and H_2O as the precursors for Al and O_2 respectively analogous to "A" and "B" in fig. 4.1 (a) [92] (b) A so-called temperature window for an ALD process [93].

TMA. The reaction creates oxygen bridges between adjacent Al atoms, new hydroxyl groups, and methane as by-products according to the following reaction.

$$H_2O(g) + -O-Al(CH_3)_2(s) \rightarrow -O-Al(OH)_2(s) + (-O-)_2Al(OH)(s) + CH_4(g) + H_2O$$

The formation of a very strong Al-O bond from efficient reactions is crucial for the growth of Al_2O_3 [89]. The by-products are purged away, and the top surface contains hydroxyl groups ready to react with TMA while pulsed in the next cycle. The thickness of the monolayer after the first step is the growth per cycle (GPC) corresponding to that step. The cycle could be repeated as needed to acquire desired film thickness. However, GPC could vary from cycle to cycle based on the concentration of available accessible sites, nucleation, and evolution of the film as the film grows. A typical Al_2O_3 growth rate of 1.1-1.2 A^0 has been reported per the "A-B" cycle. The cyclic nature makes the surface reactions in an ALD process sequential that prevents the gaseous mixing

of two precursors. It is beneficial as it hinders the formation of particles from gaseous reactions. These particles if formed could deposit on the sample surface producing a granular film [89].

As most of the ALD process is thermally activated, temperature plays an important role in the controlled growth of a thin film [93]. The effect of temperature on ALD thin film growth can be described with the help of the "temperature window" as shown in Figure 4.2(b). If the temperature is not sufficiently high enough, the precursor might get condensed and will not react spontaneously with the substrate due to a lack of enough activation energy. On the other hand, with a temperature greater than the window limit, a precursor might be prematurely decomposed resulting in a higher deposition rate [94]. Alternatively, the precursor might not form a strong bond with the substrate surface causing desorption at high temperatures. This will lead to little or no reaction with another precursor and thus resulting in a reduced or even no film growth at all.

4.2. Basics of Spectroscopic Ellipsometry

After the growth of necessary materials by ALD for the optimized EAM, optical properties of grown materials need to be determined. To do so, Spectroscopic Ellipsometry (SE) measurement is one of the effective means that is an indirect non-destructive optical measurement approach that helps determine the physical parameters of thin films such as thickness, refractive index, carrier concentration, mobility, etc. The term indirect has been used in the sense that, in ellipsometry, a polarized beam of light is reflected off a sample at an oblique angle of incidence and the change in polarization state induced by the sample is detected. Then the measurement data is analyzed and modeled to extract physical parameters corresponding to the material under measurement. Figure

4.3(a) shows the basic schematic for the measurement technique. The incident beam contains in-plane (*p*) and out-of-plane (*s*) components.

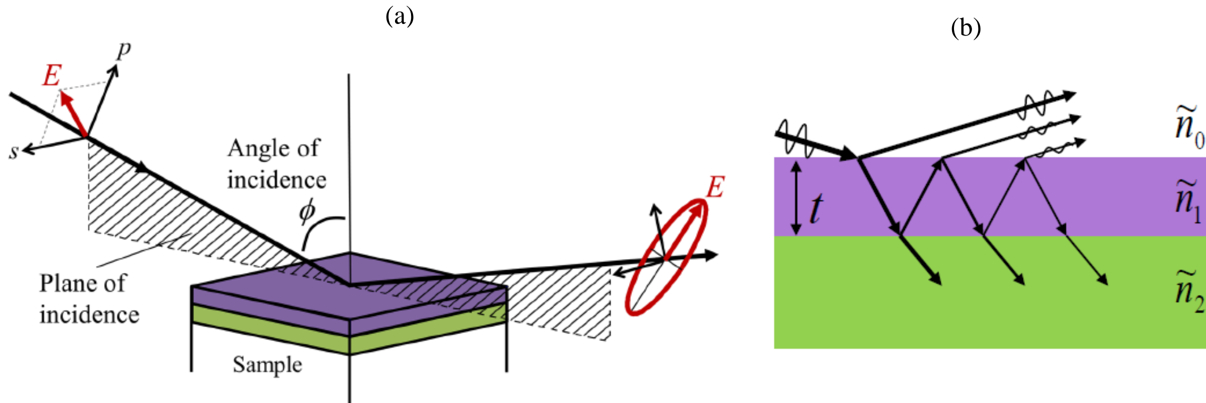

Fig. 4.3: (a) Schematic depicting ellipsometry measurement technique at oblique incident. The polarization of incident beams changes upon the reflection off the sample surfaces/interfaces. (b) Schematic showing multiple reflections and refractions at the interfaces [95].

A beam with a known, but arbitrary polarization is incident upon the material. For a thin film the, waves reflected from each interface experience different reflection coefficients based on their polarization and produce interference patterns as shown in Figure 4.3(b). As a result of this interaction, the light polarization changes, embedding a signature of material properties (*e.g., the refractive index*). Typically, this interaction is detected in the reflection of light from the sample.

In ellipsometry, each layer of a sample could be described by thickness and optical constants (*n* and *k*). After the measurement, the data are presented in terms of the SE parameters Ψ and Δ as given in Equation 4.1 [95,96].

$$\tan(\Psi)e^{i\Delta} = \frac{\tilde{r}_p}{\tilde{r}_s} = \frac{|r_p|}{|r_s|}e^{i(\delta_p - \delta_s)} \quad 4.1$$

Here, $\tilde{r}_p$ and $\tilde{r}_s$ are the complex reflection coefficient for p and s polarized light, respectively, also known as complex Fresnel reflection coefficients. δ_P and δ_s represent the phase of the p and s-polarized light respectively. Figure 4.4 shows sample experimental data (Ψ and Δ). The

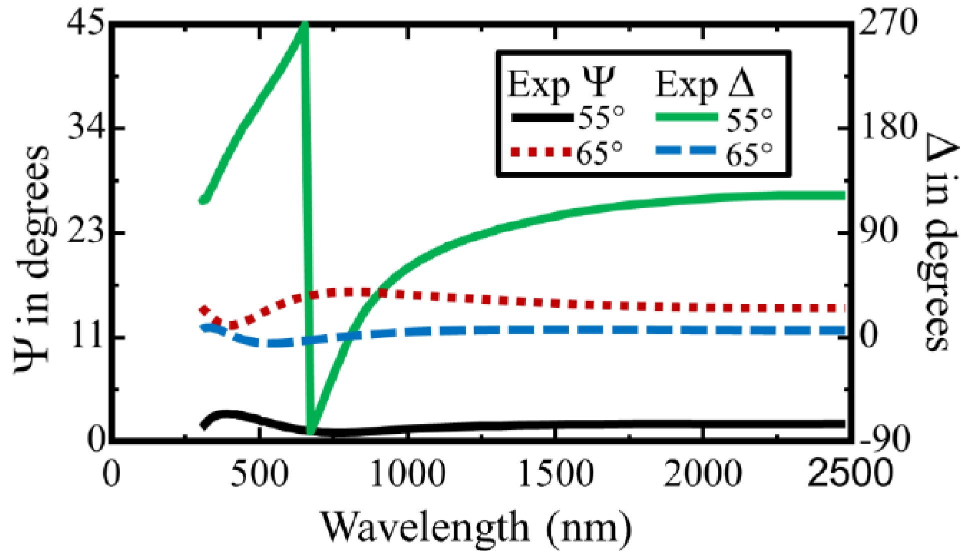

Fig. 4.4: A sample ellipsometry measurement at oblique incidences showing data in terms of Ψ and Δ [95].

parameter Ψ and Δ do not directly interpret the physical properties of the material. To extract meaningful parameters such as thickness and optical constants, a model must be built to fit the optical data. The fitting quality is determined by Mean-Square-Error (MSE) which solely indicates how well the model matches the SE data. Figure 4.5 shows the basic flow diagram for ellipsometry. Depending on the type of materials (*e.g., metals, dielectric oxide, semiconductor*) different fitting methods such as Cauchy, Sellmeier, B-spline, General Oscillator (Gen-Osc: Drude, Lorentz, etc.) are available. For example, the Drude-Lorentz Oscillator can be used to model thin films containing free electrons such as ITO, AZO, GZO, etc., the concept of which has been discussed

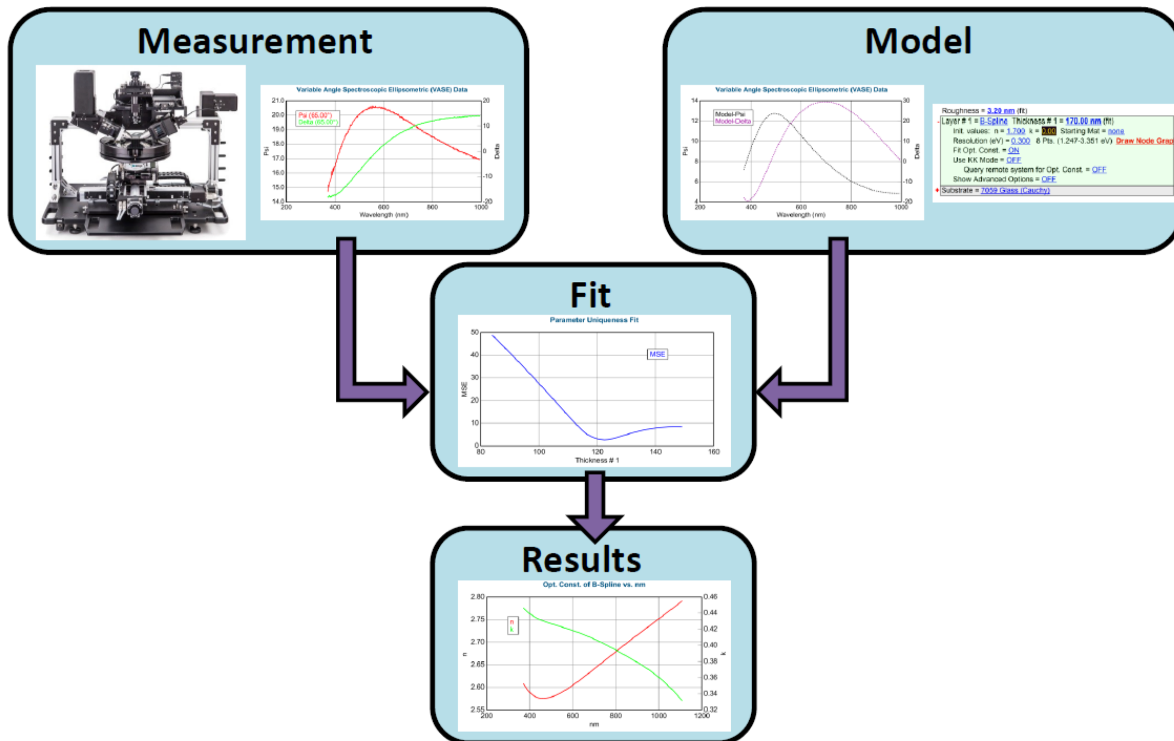

Fig. 4.5: Basic flow diagram for spectroscopic ellipsometry for the extraction of physical parameters [95]

in section 2.6. On the other hand, Cauchy and B-spline are used to model transparent dielectric (*e.g.*, HfO_2) and metals (*e.g.*, *TiN*) respectively.

4.2.1. Cauchy Model for Transparent Film

For a transparent film (i.e., no absorption within a specified range of photon energies, for example, SiO_2 in the visible and IR regimes), the Cauchy model can be used to fit SE data and extract optical functions. The optical constants of such materials can be represented by a refractive index (n) that varies slowly as a function of photon energy and an exponential absorption tail (k) across a range of spectrums with photon energy less than the band gap edge. The refractive index is expressed by an inverse power series of wavelengths containing only even terms given in Equation 4.2 [96].

$$n(\lambda) = A + \frac{B}{\lambda^2} + \frac{C}{\lambda^4} \qquad 4.2$$

Besides the extinction coefficient is represented by a simple exponential function (Equation 4.3)

$$k(\lambda) = (K_{amp}) e^{a_{\exp}\{1.24(\frac{1}{\lambda} - \frac{1}{(E_{BE})})\}} \qquad 4.3$$

Where, A, B, and C are variable fit parameters to determine the refractive index. K_{amp} and a_{exp} are fit parameters for determining the shape of the extinction coefficient (k). E_{BE} represents a band edge that is not a fit parameter but can be set manually in the model.

4.2.2. B-spline Model for Metals

The B-spline method uses basis spline [95] curves to represent complex dielectric functions (ε_1 and ε_2) as a function of photon energy (eV). The curves consist of a series of nodes or knots, each of which has a position and amplitude. Mathematically a higher-order B-spline basis function $B_i^k(x)$ can be defined by Equation 4.4 [97].

$$B_i^k(x) = (\frac{x - t_i}{t_{i+k} - t_i}) B_i^{k-1}(x) + (\frac{t_{i+k+1} - x}{t_{i+k+1} - t_{i+1}}) B_{i+1}^{k-1}(x) \qquad 4.4$$

The superscript k denotes the degree of the B-spline while the subscript i indexes the knots that are the nodes on the x-axis where the curve transitions occur from one polynomial segment to another. A spline curve $S(x)$ could be formed as a linear sum of n basis functions as shown in Equation 4.5.

$$S(x) = \sum_{i=1}^{n} c_i B_i^k(x) \qquad 4.5$$

Where c_i are the spline coefficients for the *i-th* basis function. Figure 4.6(a) shows a sample B-spline basis function t_i for degrees 0,1,2, and 3. B-spline has been reported as computationally efficient compared to conventional cubic spline along with a few other features. For example, changing the amplitude of a node only affects the local shape of the curve [95,97]. This approach only involves a fitting function having a set number of nodes to accurately match ellipsometry data (Ψ and Δ) and produce optical functions. Besides, Kramers-Kronig consistency is crucial to derive physically correct dispersion (imaginary part of permittivity, $\varepsilon_2(\omega) \geq 0$) and could easily be implemented by imposing the spline coefficients to be positive, $c_i \geq 0$ (Figure 4.6(b)) [97].

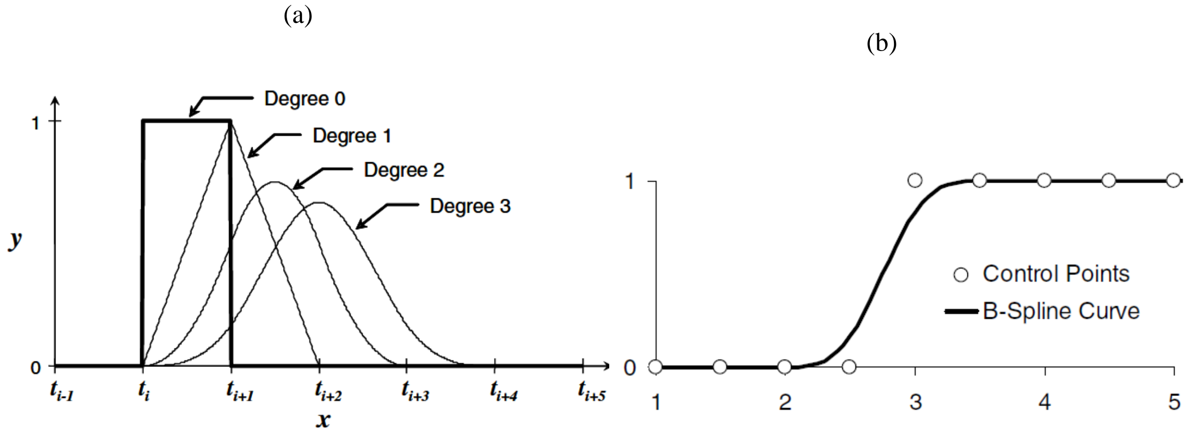

Fig. 4.6: (a) Formation of a B-spline curve with basis functions through degree 0 to 3. (b) Implementation of Kramers-Kronig consistency in B-spline by imposing positive value of controlling points for a smooth transition near the band edge absorption of a material [97].

However, because it is purely mathematical, it fails to extract any physical properties from the sample such as carrier concentration, band-edge, and scattering rate values [95]. However, the B-spline model can then be used as a fitting function for general oscillators (*e.g., Lorentz, Drude*) and vice versa, enabling the extraction of physical parameters. So, plasmonic materials such as

metals (*e.g., gold, TiN*) that absorb light and are thus associated with loss can be modeled using the B-spline technique and one can swap between them [98]. This is helpful in certain cases as the B-spline coefficients can aid in finding unique general oscillator coefficients.

4.3. Sample Preparation for Material Growth

As part of an MIS fabrication process that is required for an EAM, materials such as dielectric oxides (e.g., HfO_2), TCO (e.g., AZO), and metal (e.g., TiN) have been deposited using ALD and the properties of which have been investigated by SE. Before depositions, sample substrates are needed to be cleaned appropriately. The substrates were cleaned in order as follows: First, acetone was used to remove any organic dust or particles by rinsing the substrates for approximately 3 to 5 minutes. Second, Iso-Propyl-Alcohol (IPA) spray was immediately applied as soon as the substrates were removed from the acetone beaker. This helps to remove acetone and prevents it from becoming volatile upon contact with air. The substrates were then dipped and rinsed into the IPA beaker for approximately 3 to 5 minutes. Third, the substrates were cleaned by rinsing using toluene for approximately 3 to 5 minutes to remove any oil or grease contaminants. Finally, toluene was removed by subjecting the substrates to IPA again for 3 to 5 minutes. Note that rinsing was performed using ultrasonication.

4.4. ALD Growth of HfO_2 and HfAlO alloy

A dielectric oxide is an indispensable component of an MIS structure and is thus an integral part of the proposed EAM. The semiconductor technology industry has been using SiO_2 as the gate

dielectric oxide the thickness of which has been constantly reduced to shrink transistors and thus increase device density following Moor's law. However, there is a tradeoff between gate voltage and the thickness of SiO_2 since leakage current increases with reduced thickness due to direct tunneling through SiO_2 thin film [99]. One possible solution is to use a thicker dielectric material with a higher dielectric constant to decrease leakage current and improve switching speed. HfO_2 and Al_2O_3 have been reported as alternatives to conventional SiO_2 gate oxide [100,101]. HfO_2 has a relatively large dielectric constant (k = 20-25) and moderate bandgap (~5.7 eV) but it lacks performance requirements due to low crystallization temperature (< 500^0C) resulting in higher leakage current along the grain boundaries [100]. On the other hand, Al_2O_3 has a large bandgap (~8.8 eV) but falls short due to a relatively low dielectric constant (k = 6-9) [99]. To overcome this, a homogeneous mixture of HfO_2 and Al_2O_3 forming HfAlO can show improved thermal stability at elevated temperatures (~1000^0C). Besides, optimum Al incorporation diffuses into HfO_2 causing a more stabilized tetragonal phase resulting in an improved dielectric constant and bandgap while reducing hysteresis and electrical defects [99].

As discussed in section 3.2.1, HfO_2 has been incorporated as the dielectric oxide within the optimized MIS and the final optimized EAM will require the deposition of the oxide directly on top of Si. In this research, optical properties of purely HfO_2 and HfAlO alloy by the inclusion of Al_2O_3 into HfO_2, grown on Si substrate have been investigated. Tetrakis(ethylmethylamido)hafnium (IV) (TEMAH), Trimethyl aluminum (TMA), and water (H_2O) have been used as the precursors for hafnium, aluminum, and oxygen respectively. Figure 4.7 shows the schematic of pulses and periods for the ALD growth processes. For all the growth

processes, Ar has been used as the carrier and purging gas. A total of four samples were grown to investigate the effect of the Al inclusion

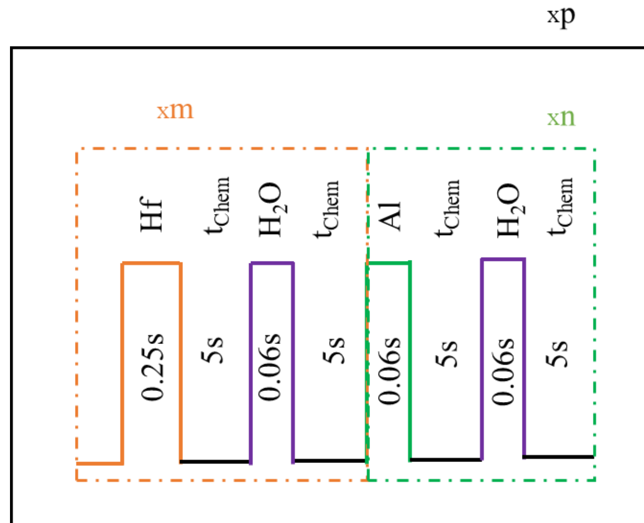

Fig. 4.7: Schematic showing the precursor pulses and the corresponding periods of the individual section of the ALD growth process for HfAlO.

on the optical properties of HfO_2. The process can be expressed as $[m \cdot (HfO_2) + n \cdot (Al_2O_3)] \cdot p$ where *m* and *n* represent the repeating times for the HfO_2 and Al_2O_3 sub-cycles respectively while *p* represents the repeating times of the whole super cycle [99]. For all the grown samples, the set temperatures are summarized in Table 4.1.

Table 4.1: Set temperatures for the growth of HfO_2 and HfAlO alloys

Title	Temperature
Substrate Chuck inside the reactor	250^0C
Reactor wall (top and bottom)	200^0C
Precursor delivery line	150^0C

The SE data have been acquired at three angles of incidence: 50^0, 60^0, and 70^0 using J.A. Woollam M2000 spectroscopic ellipsometer. Figure 4.8(a) shows SE measurement data acquired at a 50^0 angle of incidence for sample S3. All the acquired data have been fitted using the Cauchy model in CompleteEASE software. Table 4.2 compiles the value of *m,n,* and *p* from the growth processes

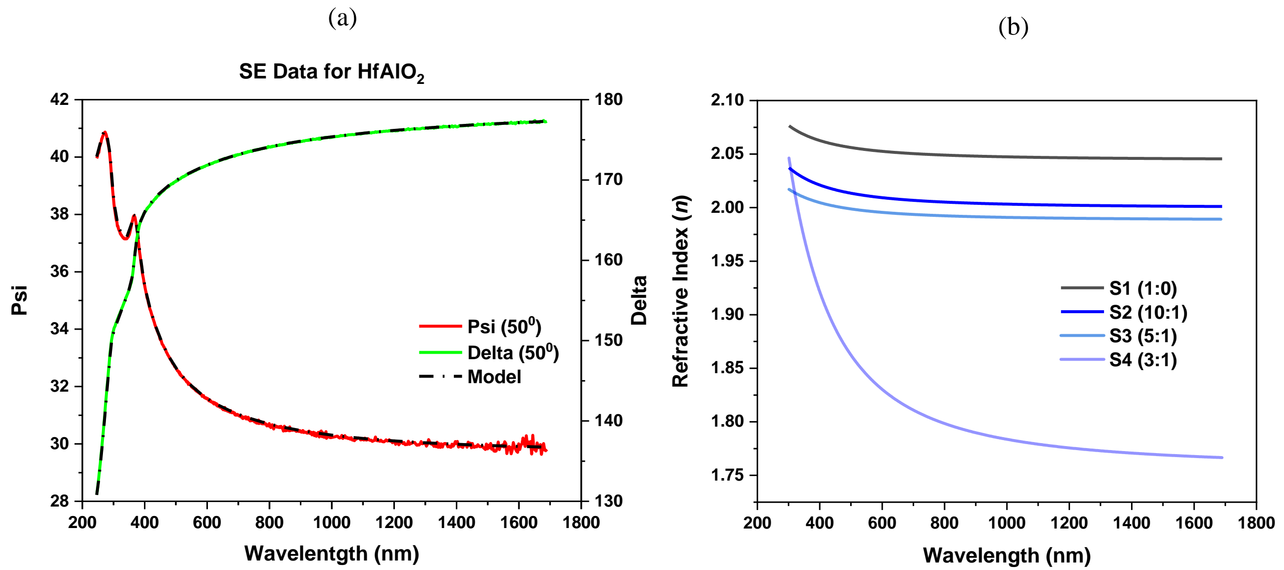

Fig. 4.8: (a) SE data in terms of Ψ and Δ for the sample S3 at a 50^0 angle of incidence. The respective data from the model is also shown (b) Refractive index (real part, n only) of grown samples showing the decreasing trend of n with increasing trend of Al content. The imaginary part of the refractive indices (*k*) for each oxide is close to zero (not shown in the figure).

and the value of the coefficients A, B, C, MSE, film thickness (nm), and the roughness from the Cauchy model for each sample.

Table 4.2: Summary of the parameters applied to oxide growth processes and the derived values from the Cauchy model.

ID	*m*	*n*	*p*	A	B	C	MSE	Thickness	Roughness
S1	1	0	50	2.05	0	0.0003	1.63	11	1.82
S2	10	1	5	2	0.0034	0	1.77	10.76	0
S3	5	1	8	1.98	0.00265	0	1.59	10.75	1.12
S4	3	1	17	1.679	0.03129	0	3.43	10	2

From the table, the content of Al increases from S1 to S4. In other words, S1 is purely HfO_2 while the rest samples are $HfAlO_2$ alloys. Figure 4.8(b) shows the optical constants (real part of refractive indices (*n*) only) of the four samples. From the figure, with the increasing inclusion of Al causes the refractive index of the alloy to reduce. The S4 was grown with a relatively high percentage of Al content with a ratio of 3:1 (*m:n*) and resulting in the refractive index (*n*) closest to Al_2O_3 compared to other samples. The scope of this research has been the verification of the optical properties of HfAlO alloy through the inclusion of Al_2O_3. From the results (Figure 4.8(b)), the relative permittivity lies within the range set by Al_2O_3 and HfO_2 which is consistent with the literature work [99]. However, this research did not cover the analysis such as capacitance-voltage measurements (C-V) and X-ray photoelectron spectroscopy (XPS) to further analyze and verify the improved dielectric constant, band gap, and stoichiometry of the grown films. Further analysis might provide a better understanding of achieving a HfAlO alloy with a higher dielectric constant and band gap for reduced leakage current, and optimum effective oxide thickness (EOT), making the oxide alloy suitable for the integration in MIS for the EAM application.

4.5. ALD Growth of Al-doped ZnO

The ALD technique is used to grow a variety of materials. Besides dielectric oxides such as Al_2O_3, TiO_2, HfO_2, etc., other transparent conducting oxides (TCO) such as Al-doped ZnO (AZO), Tin doped Indium Oxide (ITO), Ga doped ZnO (GZO) have been reported [79,86]. AZO is one of the materials in the TCO family that exhibits ENZ behavior. Being transparent in the visible regime and possessing tunability for ENZ make the material useful for many different applications, for

example, in Electro-absorption Modulators (EAM), light-emitting diodes, flexible transparent electronics, and solar cells [102]. In this research, a TCO has been considered as both the tunable active material that facilitates the optical modulation and the metallic contact in the MIS structure. First, the tunability of ENZ point across the spectrum for the AZO films has been investigated on a Si substrate by tuning the Al precursor pulse time. Second, the AZO films were deposited on fused silica substrates, and the corresponding thickness, spectral position of ENZ, film resistivity, and carrier scattering time have been analyzed.

The AZO films have been deposited on Si substrates using trimethyl aluminum (TMA), Diethyl Zinc (DEZ), and H_2O as the precursors for Al, Zn, and O_2 respectively. A complete cycle referred to as a super cycle is composed of two distinct sub-cycles. Figure 4.9 shows the schematic of pulses with duration and chemisorption periods for the growth process. Here *m* represents the repeating time of the sub-cycle for the ZnO growth. On the other hand, *n* represents the repeating

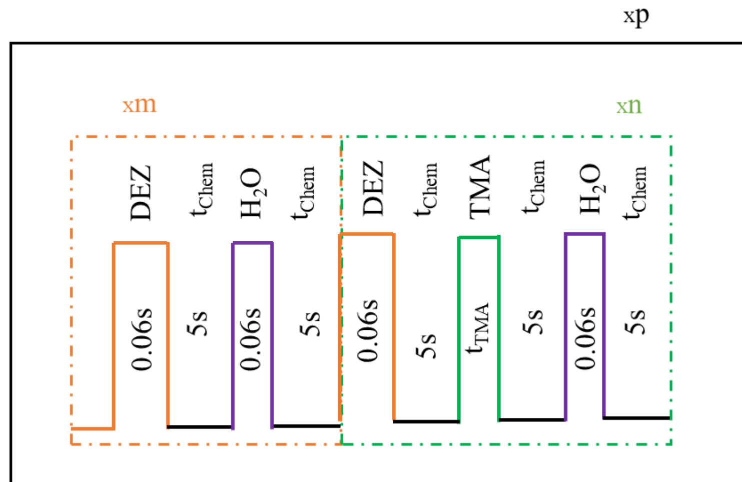

Fig. 4.9: Schematic showing the precursor pulses and the corresponding periods of the individual section of the ALD growth process for Al-ZnO.

times of the sub-cycle in which Al pulse is included. The sub-cycle represented by n could also be referred to as the dosing sub-cycle [94]. The number of dosing sub-cycles and the TMA pulse period could be tuned to control the free electrons within the grown film. And thus, the spectral position of ENZ across the spectrum can be tuned according to the Drude model for doped semiconductors.

Two films, S1 and S2 have been grown on Si substrates with two different TMA pulse periods (7.5 and 60 milliseconds respectively). In the growth processes, the first sub-cycle is composed of alternating 5 pulses of DEZ followed by H_2O (*i.e.,* $m=5$). The first sub-cycle is then followed by a single dosing sub-cycle to introduce Al as the dopant (i.e., $n=1$). The whole super cycle was repeated for 80 and 70 cycles for samples S1 (i.e., $p=80$) and S2 (i.e., $p=70$) respectively to grow films with a thickness of ~45 nm and ~35 nm. For all the AZO growth processes, Ar has been used as the carrier and purging gas. The set temperatures for the growth processes have been enlisted in Table 4.3.

Table 4.3: Set temperatures for the ALD growth of Al-doped ZnO

Title	Temperature
Substrate Chuck inside the reactor	350^0C
Reactor wall (top and bottom)	300^0C
Precursor delivery line	150^0C

Figure 4.10(a) shows SE measurement data in terms of Ψ and Δ acquired at an oblique incidence of 55^0 for the sample S2. In the figure, the corresponding fitted data are also shown. In the modeling, Si has been used as the substrate. The AZO layer has been modeled as a general oscillator (Gen-Osc) constituting two types of oscillators namely PSEMI0 and Drude (RT)

available in the CompleteEASE software package. Figure 4.10(b) shows the optical constants (ε_1 and ε_2) of the two samples. Having a larger dosing period (~9x) causes the ENZ point to blueshift for the sample S2 compared to S1 as shown in the figure.

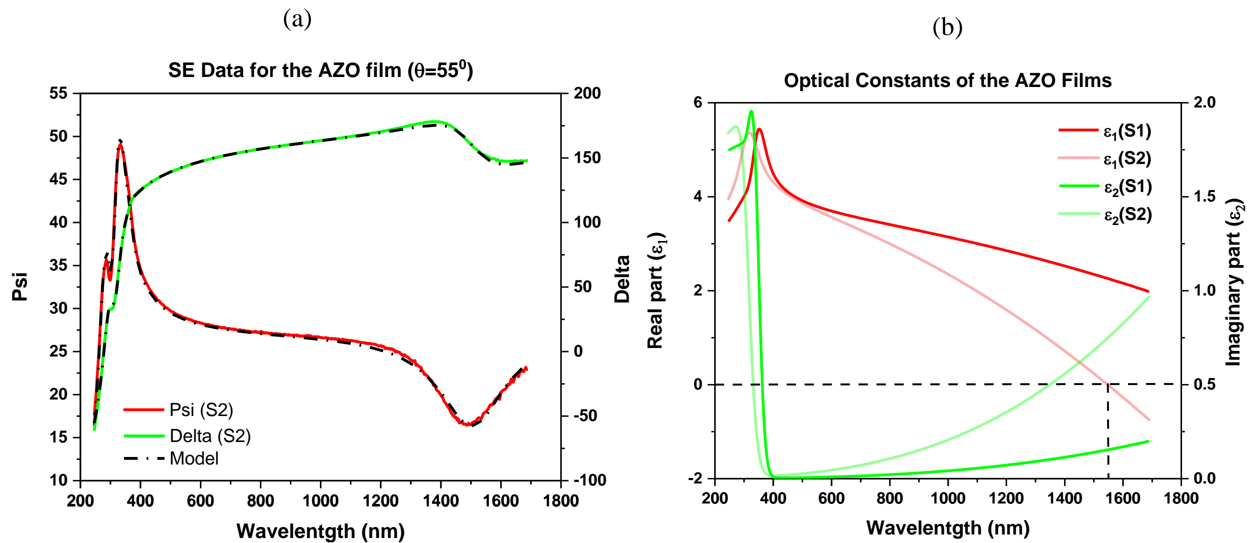

Fig. 4.10: For the AZO films grown on Si substrate (a) SE reflection data at oblique incidence for the sample S2 (b) Optical constants of the films derived from modeling the film as Gen-Osc layer. The black dotted line points out the ENZ at ~1550 nm for the sample S2.

An AZO thin film was also grown on a 4-inch fused silica substrate to investigate the uniformity of thickness, resistivity, and carrier scattering time of the deposited film. The dosing cycle was set to achieve ENZ at ~1500 nm. The super cycle was set to run 60 times. The $m:n$ was set as equal to 5:1 like before for samples on Si. Figure 4.11(a) shows the Ψ and Δ data acquired at an oblique incidence of 60^0. For transparent substrate, reflection from the substrate back surface interferes with the reflected lights from the air/film and film/substrate interfaces. This backscattering is

(a) (b)

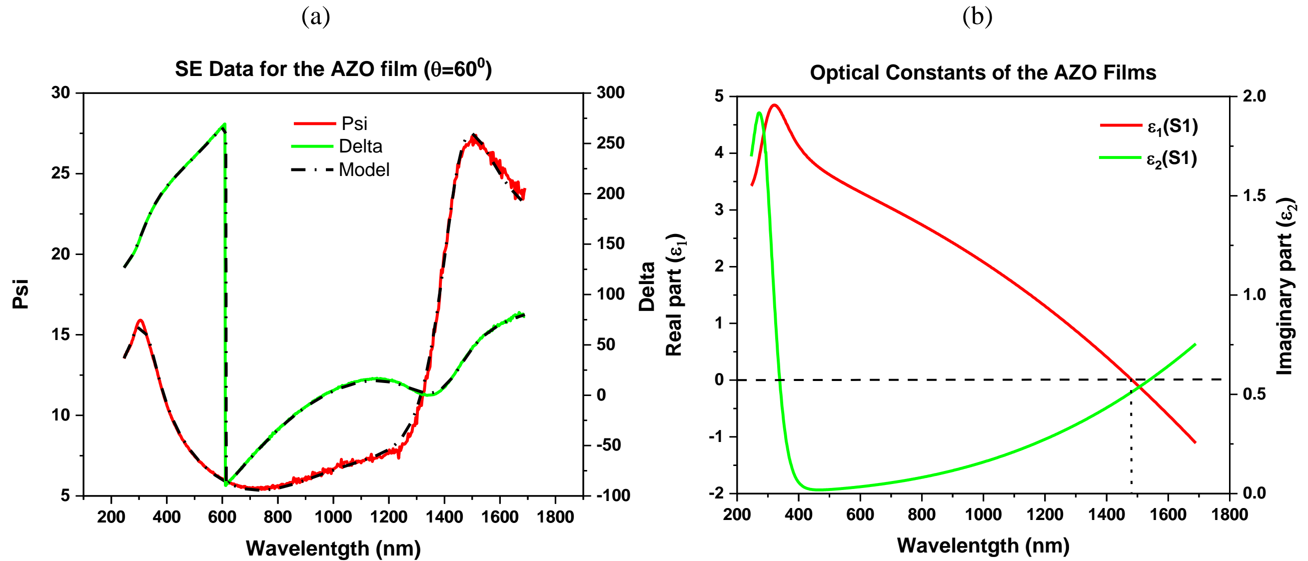

Fig. 4.11: For the AZO films grown on SiO_2 substrate (a) SE measurement data acquired at an oblique incidence of 60^0 (b) Optical constants of the films derived from modeling the film as Gen-Osc layer. The black dotted line points out the ENZ at ~1472 nm.

incoherent with the surface reflections [90] and might cause complications if gets detected at the detector unless dealt with care. The CompleteEASE software offers an option to correct amplitude offset due to the back surface reflection. Besides roughening the substrate backside, for example, adding a cloudy tape helps scatter light and prevent the light reflected off the backside from propagating back to the detector. In this measurement, the second approach has been adopted. Figure 4.11(b) shows the optical constant of the film. The ENZ is located at ~1472 nm with an imaginary part of the permittivity equal to ~0.5. Figure 4.12(a-c) shows the uniformity of the film in terms of thickness, resistivity, and scattering time. The thickness ranges from 33 to 37 nm, the resistivity is quite uniform across the film with a deviation as low as 0.02 mΩ.cm, and the scattering time ranges from 5.7 to 6.2 femtoseconds.

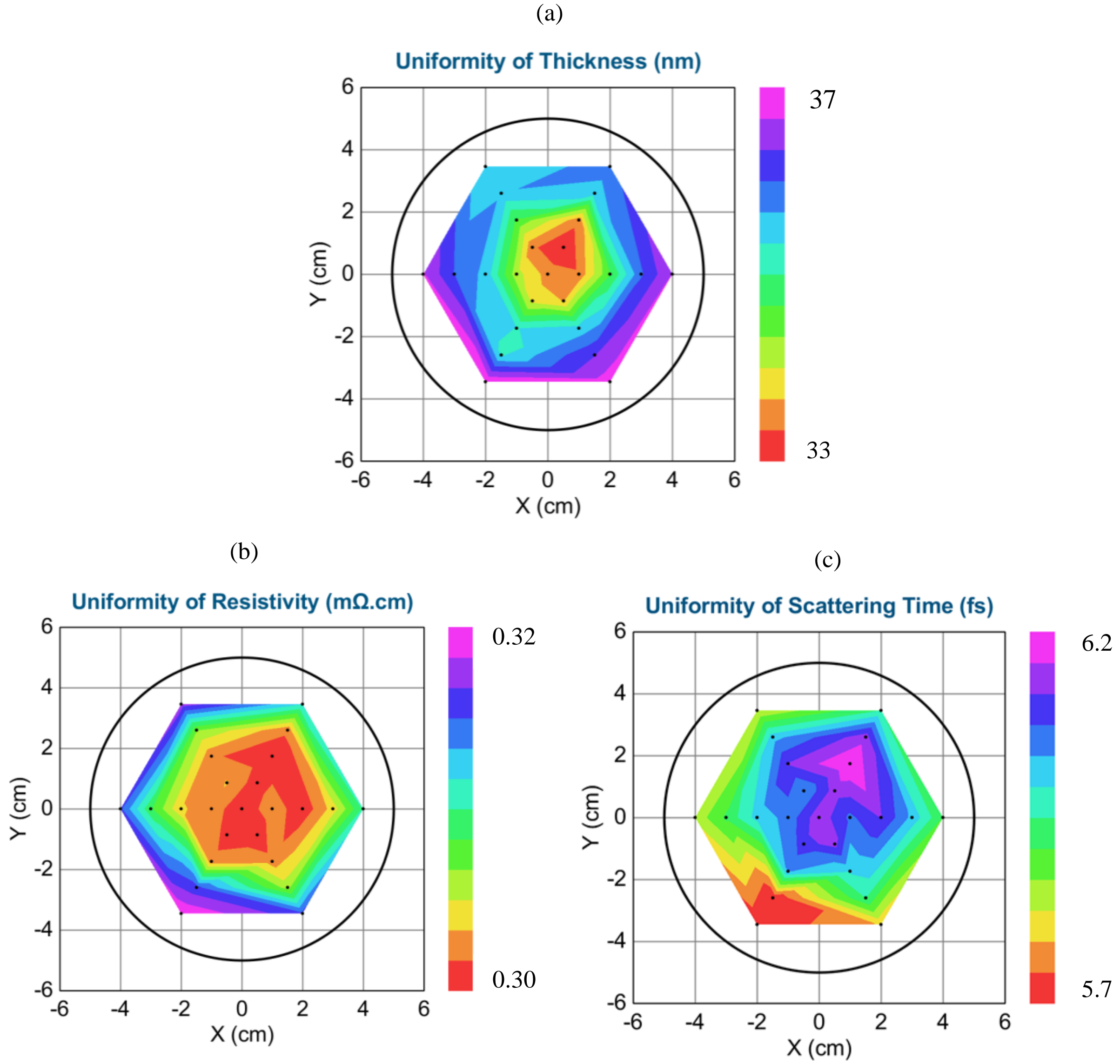

Fig. 4.12: For the AZO films grown on SiO_2 substrate (a-c) Surface plots showing the uniformity of the film in terms of thickness, resistivity, and scattering time respectively.

This research focused on tuning the dosing period to tune the spectral position of ENZ point (ε_1) of AZO and investigate the imaginary part of the permittivity, ε_2. ε_2 as small as possible is desirable so that optical loss can be minimized from light-ENZ material interaction at EAM off-state and thus the IL. From the results, Figure 4.10(b), the ENZ can be tuned by optimizing the

dosing period and thus setting appreciable electron concentration within the film while $\varepsilon_2 \sim 0.1$ is achievable at EAM off-state. However, the research did not focus on a Hall measurement of the film grown on a SiO_2 substrate. So, the further scope of the continuation of this research could be extracting carrier concentration, DC resistivity, and mobility from hall measurement to optimize the dosing period in the growth process. This is crucial for EAM application, for example, since increasing carrier concentration could potentially increase the loss factor ($\gamma = e/(m^{*}\mu)$), even at the off-state endangering the main goal of achieving reduced off-state IL. Nonetheless, an AZO film with mobility, $\mu \geq 40\ cm^2/V \cdot s$, $\varepsilon_2 < 0.1$, and resistivity $\sim 10^{-3}\Omega \cdot cm$ could be promising as both gate and tunable material for EAM applications.

4.6. ALD Growth of TiN for Metallic Contact

Metals are crucial for applications such as in plasmonic, metamaterials, and Transformation Optics (TO). Conventional metals that are used for such applications include gold, silver, and copper. Their optical dielectric function could be expressed by the Drude-Lorentz model discussed in section 2.6. According to the model, the real part of the permittivity (ε_1) of these conventional metals is very large [1]. This is disadvantageous in some applications. For example, in TO, the equal filling fraction of dielectric and metallic portion is preferable to achieve a balanced polarization necessary for the applications. But with large ε_1 the filling fraction of metal becomes small, placing a challenge for their integration in nanofabrication. Moreover, the imaginary part of the permittivity (ε_2) represents a loss that is detrimental to optical applications. The loss mechanism depends on mainly three factors namely interband, intraband, and electrons scattering

or relaxation losses (γ). The intraband and scattering losses often make overall losses appreciably high for optical applications even if the interband component is absent in the NIR regime. The requirement of the thin metal film results in smaller grain boundaries than thick metal one and thus increases overall loss [1]. The dependency of γ on grain boundary (d) is expressed by Equation 4.6.

$$\gamma = \gamma_0 + A\frac{\upsilon_F}{d} \quad 4.6$$

where γ_0 is the scattering loss for bulk metal, A is a dimensionless empirical constant, and υ_F is the Fermi velocity of electrons in a metal. To overcome such challenges, efforts have been put to introduce alternatives to conventional metals. Metal nitrides such as TiN, TaN, HfN, etc. have been reported as alternatives to gold and silver. In this research, the metallic contacts are assumed to be located appreciably far away from where the light EM is predominantly confined (*i.e., within Si rib waveguide or TCO slot*) so that metal does not interact with light for the expectation of a low off-state loss. Nonetheless, the fabrication of the proposed EAM will include metallic contacts for biasing the device.

In this research, as an alternative to conventional plasmonic materials, TiN has been grown on c-plane sapphire, glass, and Si substrates using the ALD technique (Cambridge Fiji G2). Besides its metallicity and optical loss have been investigated in terms of optical constants. The tetrakis(dimethyl-amido) titanium (IV) (TDMAT) and N_2 plasma have been used as the precursors for Ti and N_2 respectively. The set temperatures for the growth recipe at different parts of the instrument are listed in Table 4.4.

Table 4.4: Set temperatures for the ALD growth of TiN

Title	Temperature
Substrate Chuck inside the reactor	450^0C
Reactor wall (top and bottom)	300^0C
Precursor delivery line	150^0C
Precursor jacket	75^0C

Figure 4.13 shows the single cycle of the recipe for the growth of TiN. The TDMAT was pulsed in the chamber for 0.25 seconds. The recipe then allows a chemisorption time of 0.5 seconds followed by N_2 plasma for 25 seconds. The Ar was used as both the carrier and purging gas at 30 sccm and 10 sccm respectively.

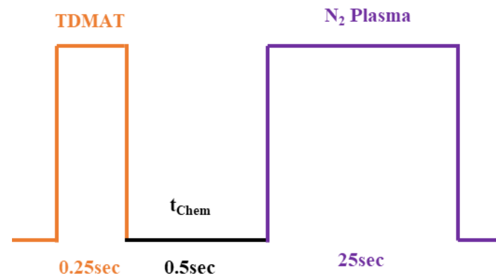

Fig. 4.13: Schematic representation of a single cycle for the ALD growth of TiN.

Table 4.5: Set temperatures for chamber baking

Title	Temperature
Substrate Chuck inside the reactor (no sample)	500^0C
Reactor wall (top and bottom)	350^0C
Precursor delivery line	175^0C

The ALD chamber needs to be conditioned and optimized for the growth of the final optically thick (*i.e., more than 5 to 6 times skin depth*) TiN films. For example, if the same chamber is used for the growth of oxide materials that could cause the presence of oxygen in the chamber. In turn

that could degrade the metallicity of the grown film [103–105]. To overcome this the chamber has been baked for more than 8 hours by setting temperatures as listed in Table 4.5. Four growth trials have been performed before the growth of the final thick TiN film. The fourth trial has been performed under the same condition listed in Table 4.4 and the single recipe (Figure 4.13) was

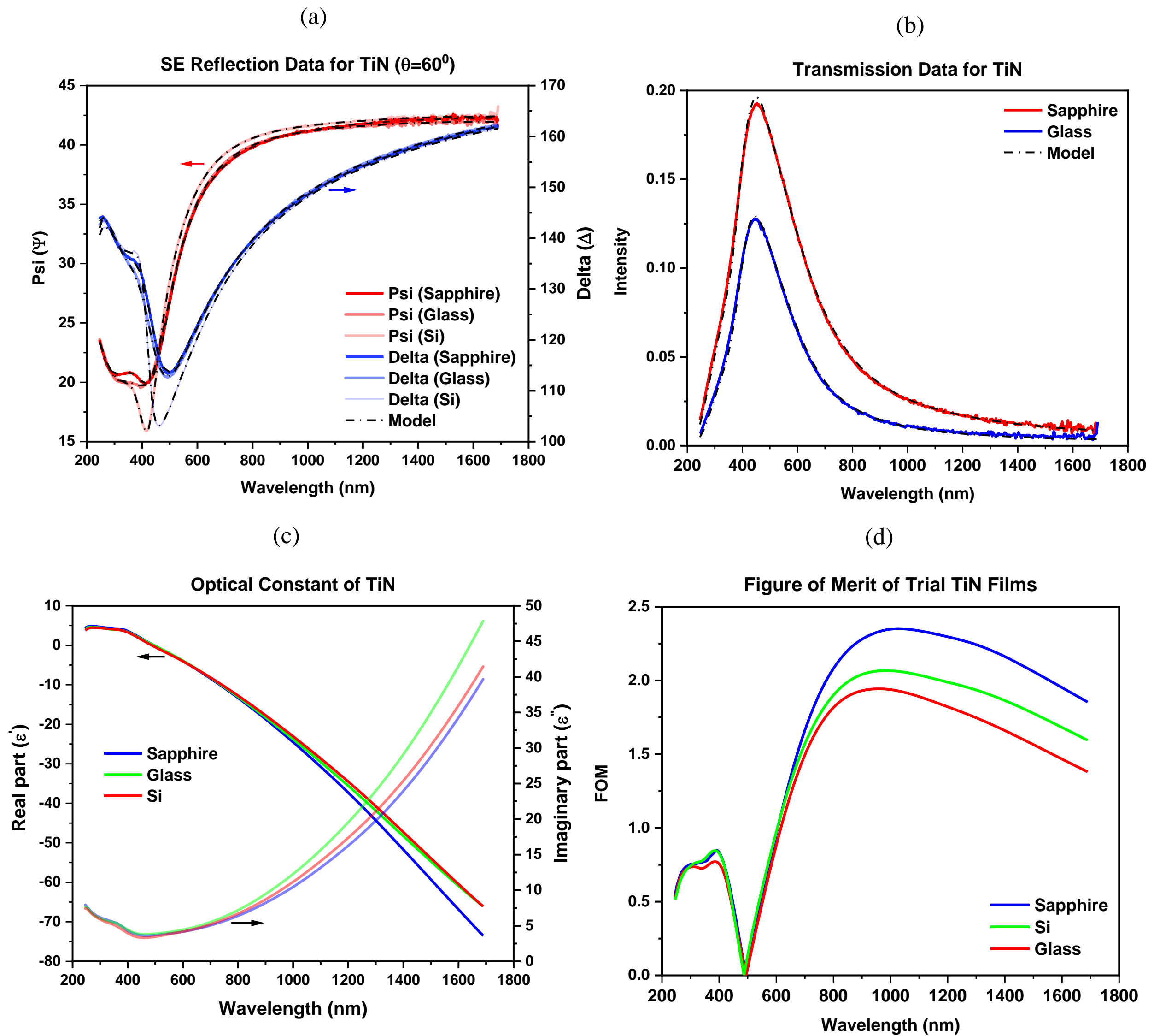

Fig. 4.14: For the films grown in the fourth trial (a) SE reflection data (b) Transmission intensity for films on Sapphire and glass (c) Derived permittivity from the B-spline model. (d) FOM showing the peak at ~2.4 for the film grown on c-plane Sapphire substrate.

repeated 510 times to grow a film with a thickness of ~60 nm. The estimated growth rate was calculated as 1.2 A^0/cycle. A reflection measurement has been performed for all the films while only transmission measurements have been executed for the film deposited on sapphire and glass. The measurement was performed using the J. A. Woollam M2000 Spectroscopic Ellipsometry instrument and the associated CompleteEASE v. 6.53 software has been used to model the data.

Figure 4.14(a) shows the SE reflection data in terms of Ψ and Δ. Figure 4.14(b) shows the transmission intensity for the trial TiN films. The corresponding models are also shown in the figures. The data have been fitted using B-spline. Before selecting the B-spline, TiN2 optical constants available in the software have been used as a starting material for the fitting of the measurement data. Following this, TiN2 has then been replaced with a B-spline model. The summary of the fitting results is enlisted in Table 4.6. Figure 4.14(c) shows the derived real and imaginary permittivity of TiN deposited on c-plane sapphire, glass, and Si substrates. The real permittivity can be considered as an indicating parameter for the film metallicity, and degree of crystallinity while the imaginary part can be thought of as an indicator for the loss factor. So, a Figure of Merit (FOM) defined as the ratio of the absolute value of the real and the imaginary part of the permittivity could be taken into account to compare the quality of the grown films [106].

Table 4.6: Summary of the results from the B-spline model

Substrate	Node Resolution (eV)	Starting Material	MSE	Peak FOM
c-plane Sapphire	0.3	TiN 2	2.05	2.51
Glass			2.14	2.42
Si			2.05	1.9

Figure 4.14(d) shows the FOMs for the grown TiN films. The TiN on c-plane sapphire results in a higher FOM equal to ~2.4.

In this research, later, optically thick films were grown (more than ~10 times the thickness of the skin depth). The single recipe shown in Figure 4.13 was repeated 2050 times. Since the film is optically thick, only the SE reflection measurement was performed and fitted with the same procedures discussed for the trial sample. The resulting permittivity and FOM are shown in Figure 4.15(a-b). The FOM for the film on c-plane sapphire is ~2.51 which is slightly higher than the trial sample. For a thin TiN film, the interface between grown TiN and substrate results in a low-quality TiN phase that light could reach and sense the phase during measurements. On the other hand, for thick films with thickness many fold the skin depth, light cannot reach and sense the low-quality phase [106]. This could contribute to a slightly better FOM for the grown thick films.

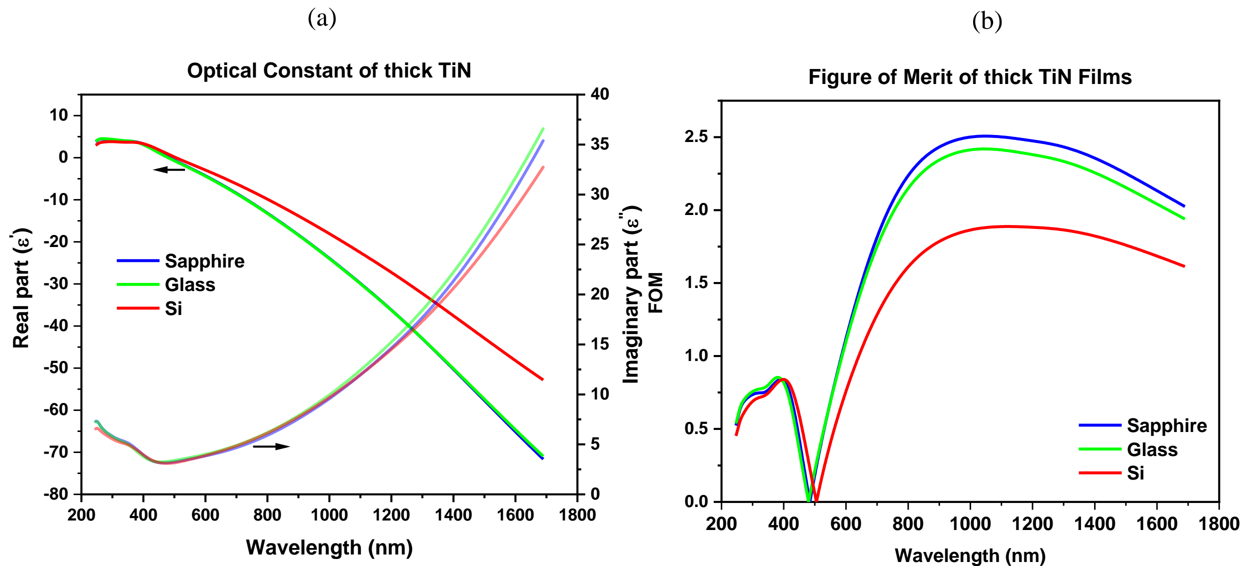

Fig. 4.15: For the final grown optically thick TiN film (a) Derived permittivities from the B-spline model. (b) FOM showing the peak at ~2.51 for the film grown on c-plane Sapphire substrate.

4.7. p-type Doping of Si

As previously discussed in section 3.2, the optimized MOS structure includes a p-type Si layer as the ground contact. Undoped Si has resistance in the order of mega-ohm and needs to be doped to increase its conductivity (*i.e., reduced resistivity to decrease unnecessary voltage drop*) for the prevention of any negative effect on the device's operation speed ($1/RC$) and power consumption ($\frac{1}{4}CV^2$). In this research, Si has been doped by a commercially available solid p-type dopant (boron nitrite planar diffusion source, BN-HT) to investigate the change in resistivity and thus the efficacy of the doping process. Si on Insulator (SOI) samples have been cut in a rectangular shape for the sake of the Hall measurement (Van Der Pauw) that is necessary to extract the sheet resistivity [107,108]. Samples need to be cleaned before putting into the furnace. Table 4.7 enlists the sample cleaning steps.

Table 4.7: Sample preparation for the doping process

Step	Process
1	Dip into BOE (1:10) to remove any native oxide for 3 minutes
2	Rinse with DI water followed by N_2 dry
3	Rinse with Acetone for 3 minutes
4	Rinse with IPA for 3 minutes
5	Rinse with DI water followed by N_2 dry

The sample and the solid dopant have been placed facing each other on a quartz boat. The list of events that happened in the furnace has been summarized in Table 4.8

Table 4.8: Doping processes in the furnace

Step	Processes
1	Ramp up the temperature to 90^0C inside the furnace (N_2 flow: 6 slpm)
2	Insert the boat into the furnace at a 50% speed (N_2 flow: 3 slpm)
3	Dry out the sample and activate the dopant for 30 minutes (N_2 flow: 10 slpm)
4	Ramp up and stabilize the temperature to 1000^0C inside the furnace (N_2 flow: 6 slpm)
5	Soaking for 1 hour (N_2 flow: 10 slpm)
6	Ramp down the temperature to 200^0C (N_2 flow: 6 slpm)
7	Boat out and cool down the sample (N_2 flow: 3 slpm)

During the doping process in the furnace several reactions happen as follows:

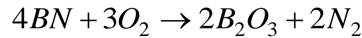

$$4BN + 3O_2 \rightarrow 2B_2O_3 + 2N_2$$

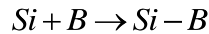

$$Si + B \rightarrow Si - B$$

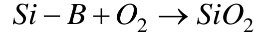

$$Si - B + O_2 \rightarrow SiO_2$$

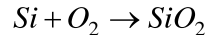

$$Si + O_2 \rightarrow SiO_2$$

Initially, boron nitrite reacts with O_2 and releases B_2O_3 that reacts with Si and produces byproducts such as the Si-B phase and boro-silicate-glass (BSG). Si reacts with O_2 and produces SiO_2. A post-doping treatment is necessary to remove the unnecessary top by-product layers following several steps before performing the Hall measurement. First, a SiO_2 or BSG layer could be formed at the surface. This layer has been removed by subjecting the sample to buffered oxide etch (1:10) for 3 minutes. Second, the Si-B phase does not react with BOE. So, the samples were chemically oxidized by nitric acid (HNO_3) for 30 minutes at 90^0C to transform the Si-B phase into BSG. Third, the newly formed BSG has been removed by putting the sample into BOE for 3 minutes. All three steps were followed by rinsing the samples with DI water and N_2 dry. Then the Hall measurement

(Lake Shore system) was performed, and the resistivity of the doped samples and the undoped samples has been determined as equal to ~12 Ω/Sq. and ~87 MΩ/Sq. respectively, indicating a many-fold reduction of Si resistivity. Moreover, by tuning the doping duration, Si resistivity could even be controlled to any desired value.

Conclusion and Future Prospect:

In this thesis, a numerical investigation has been conducted on multiple configurations of EAMs with the primary goal of side-step plasmonic loss. To do so the typical metal contact from the top of the device has been replaced with heavily doped ITO to reduce the off-state IL to less than 1 dB while including experimentally achievable parameters in the analysis. The research also covers the factors that impose tradeoffs on the device scheme and its performance. Through the analysis, the beneficial aspect of using increased SVR and mode overlap to reduce loss while maintaining modulation depth has been pointed out by comparing a rib, as well as single and multi-slot configurations, realizing a non-resonant 4-slot EAM device that exhibits ER as high as 2.62 dB/μm and IL as low as 0.3 dB/μm, facilitating 6 dB ER with 0.7 dB IL.

While the approach is a viable scheme to realize low-loss plasmon-assisted modulators with sub-dB IL, it does not escape the typical trade-offs [87,109], and it is emphasized that the device must be carefully optimized for the constraints of a given application using experimental parameters to function as intended, something not always done. Without this, exceptional performance can be predicted [110,111], but not realistically achieved. For example, the use of a low-doped ITO layer requires an operation close to the breakdown of the dielectric to achieve sufficient accumulation of carriers to produce the ENZ layer, and the voltage losses within the various layers reduce the

overall energy efficiency and speed. However, slight relaxation on the IL metric enables a final optimization of parameters such as the layer thickness, enabling a non-resonant single-slot modulator with ER of 1.4 dB/μm, IL of 0.25 dB/μm, in 6.3 μm^2 with speeds ~20 GHz and energy consumption of 1.74 pJ/bit. Such compact non-resonant devices are desirable for applications where thermal environments are unpredictable as they avoid power-hungry thermal stabilization [112]. Moreover, unlike other competing techniques, the system is entirely solid-state and CMOS-compatible, enabling integration with existing silicon photonics platforms alongside operation in robust environments. Ultimately, significant leaps in the performance of TCO-based EAMs are tied to improved mobility in conformal TCO materials (currently ~30–40 $cm^2/V.s$) [19,30,39], as this enables improved field enhancement [40] while minimizing off-state IL.

The research also investigates the optical and electrical properties of constituent materials incorporated in the EAM design. Al-doped ZnO and HfAlO alloy have been deposited by ALD and characterized by SE analysis. It has been shown that the off-state loss factor (~0.1) of AZO in the numerical analysis can be achievable from the deposited film at the desired operating wavelength. Besides the research further points out the future scope of reducing the off-state loss factor of TCO films. HfAlO alloys have been investigated and shown that the refractive index within the range of that of the HfO_2 and Al_2O_3 is achievable leaving a future scope to investigate film morphology to determine any improvement in the crystalline phase, bandgap, and dielectric strengths. Moreover, the research discussed the low-temperature growth of TiN that could be used as an alternative to conventional metals and incorporated into the design of EAM.

Appendices

The appendices were incorporated in a journal paper [65] and directly copied here with some modifications for Table A2.

Appendix I:

Material parameters for the determination of carrier profile and device optimization:

Table S1. Material parameters for the semiconductor and optical analysis

	Parameter	ITO	*HfO_2	Silicon	SiO_2
Semiconductor Analysis	Relative Permittivity (ε_r)	9 [30]	25 [64]	11.8 [30]	N/A
	Band Gap (V)	3.8 [30]	-	1.08 [30]	
	Electron affinity (V)	5 [30]	-	4.17 [30]	
	DOS, valence band (1/cm^3)	4×10^{19}	-	1.04×10^{19} [30]	
	DOS, conduction band (1/cm^3)	5×10^{18} [30]	-	2.8×10^{19} [30]	
	Electron mobility (cm^2/V.s)	40 [39]	-	1000 [30]	
	Hole mobility (cm^2/V.s)	5	-	450 [113]	
	Effective mass (m*)	0.35 [7,30]	-	-	
	DG effective mass (m$^*_{DG}$)	$m_0/3$ [32,34]	-	-	
Wave Optics Analysis	Refractive Index	**	2.07 [64]	3.48 [64]	1.5 [64]

*HfO_2 has been defined as a "charge conservation" layer. **We determine the spatial distribution of electron concentration (N) within ITO from semiconductor analysis. The spatial profile (N) is then used in the Drude model expressed as $\varepsilon_{ITO}(N)$ in equation (1) to define the spatial permittivity and refractive index $(n = \sqrt{\varepsilon_{ITO}})$ of ITO, with $\varepsilon_\infty = 3.9$, and $\Gamma = q/(m^* \mu)$ [64,114]. Effective mode indices (n_{eff}) have been found by analyzing each configuration in the FEM eigenmode solver (COMSOL Multiphysics). The corresponding propagation loss (PL) (dB/µm) has been

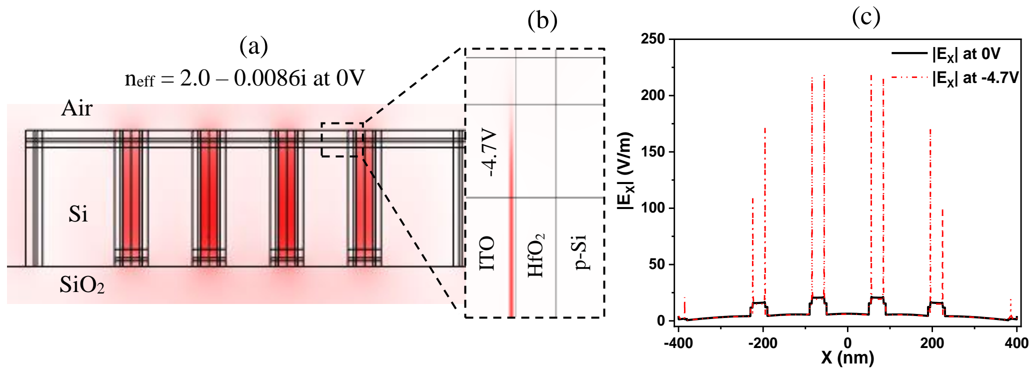

Fig. S1. (a) Effective mode index and the Ex-component of electric field at 0V. The dotted closed line highlights interfaces of ITO/HfO_2/p-Si to show (b) Field confinement at the interface of ITO/HfO_2 at -4.7V. (c) $|E_x|$ at 0V and -4.7V [65].

calculated by the following equation [64], $\alpha = 10\left|\log_e - (4\pi \operatorname{Im}\{n_{eff}\})/\lambda\right|$. The ER (dB/µm) is expressed by the equation: $ER(dB/\mu m) = \alpha_{ON} - \alpha_{OFF}$ where α_{ON} and α_{OFF} are propagation loss at a gate voltage of -4.7V and 0V respectively. The IL (dB/µm) is equal to the α_{OFF}. Figure S1(a) shows the mode profile and the effective mode index for the 4-slot EAM at 0V. The EM field is mostly confined within the ITO slot. Figure S1(b) shows the field confinement at the ITO/HfO_2 interface upon the application of a biasing voltage of -4.7V. Figure S1(c) shows the cutline view of the $|E_x|$ component in device ON and OFF states.

Appendix II:

Density Gradient (DG) theory provides a generalized form of the conventional Drift-Diffusion theory. While both methods obey electrostatics and current conservation laws, the main difference between them is the way each method treats the equation of states of the electron and hole gases. According to the DG theory, the equation of states of a carrier (electron/hole) gas depends not only on its density but also on its density gradient and the theory does so by including a quantum potential [31]. This theory has been reported as computationally efficient for device simulation that requires quantum confinement [32]. The carrier (electron/hole) profile at thermal equilibrium can be determined by solving partial differential equations that include a linear-gradient coefficient ($b_{n\ or\ p}$) that measures the strength of the gradient effect in the carrier gas. The linear gradient coefficient is inversely proportional to the product of density gradient effective mass ($m^*_{n\ or\ p}$) and a dimensionless parameter, r. It has been reported that the usual practice to determine the carrier profile is to fix the value of r while changing the value of $m^*_{n\ or\ p}$ and compare the results with the same obtained from solving the Schrödinger and Poisson (SP) equations. However, it is also reported that the product of $m^*_{n\ or\ p}$ and r is almost one under all conditions [32,34]. We further verify this approach for the electrons in ITO by simulating a 1D MOS (Metal/HfO_2/ITO) structure utilizing both DG and SP analysis available in the finite element method (COMSOL multi-physics, semiconductor Module version 5.5). In COMSOL multi-physics, the value of the parameter, r is by default fixed as equal to 3. So, we set the value m_n^* equal to $m_0/3$ where m_0 is the rest mass of a free electron. Figure S2 shows the comparison between electron concentrations in ITO predicted by DG and SP for the applied voltages of 0.1V and 1V.

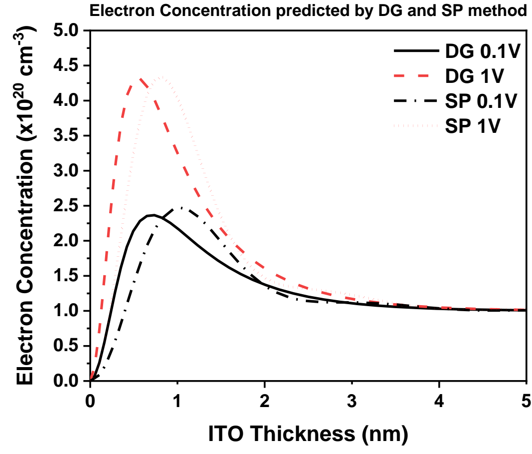

Fig. S2. Verification of the DG effective mass of electrons in ITO by comparing electron concentrations derived from DG and SP method for two different voltages. The density gradient effective mass has been set as $m_0 / 3$ where m_0 is the rest mass of free electron. For SP method, the effective mass of electron in ITO has been set as $0.35m_0$ [65].

Appendix III:

The process would begin with a standard silicon-on-insulator wafer with a 220 nm thick Si device layer and 2-5 µm thick buried oxide. Next, positive tone electron beam lithography resist, such as ZEP or PMMA, would be applied to the sample. The base racetrack waveguide, grating couplers, and rib-to-slot converter will be patterned in a single-layer exposure using electron beam lithography, followed by dry etching of Si using the Bosch process (a mixture of C_4F_8:SF_6 gas chemistry) in an inductively coupled plasma (ICP) system [81,115]. In the next step, a thin region of Si can be doped using conventional thermal evaporation doping processes with either liquid or solid dopants (e.g., BN-HT) where resistivities of 1-20 Ω/Sq. can be achieved based on the process conditions [116]. This can be completed across the entire waveguide device as the thin layer with moderate p-doping does not lead to significant propagation losses on the scale of our device. Alternatively, if selective doping is required, a SiO_2 or Si_xN_y hard mask can be deposited and patterned on top of the Si layer before the doping process. In the next step, conformal growth of 5 nm HfO_2 can be achieved by Atomic Layer Deposition (ALD) [78,79]. Using a non-critical photolithography exposure, the HfO_2 can be removed from all regions outside the active region by wet etching in ways such as using diluted HF [117], a mixture of HF, and formic acid [118], or using diluted phosphoric acid [119]. Similarly, a conformal ITO thin film with resistivity as low as ~ 6 x 10^{-4} Ω.cm can be deposited via atomic layer deposition (ALD) at relatively low optimum temperature (typically ~200-325^{0}C) and by optimizing the relative number of In_2O_3 and SnO_2 ALD cycles (using cyclopentadienyl indium (InCp) and ozone as the precursors for indium oxide (In_2O_3) while tetrakis(dimethylamino) tin (IV) and hydrogen peroxide as the source for tin oxide (SnO_2)) [86], followed by an aligned electron beam lithography exposure to pattern the ITO active

region and contact trace. Wet etching of ITO can be done using a solution of HCL [120]. Finally, metallic contact pads connecting to the p-Si and ITO layers can be added via photolithography and lift-off.

To inject light into the slot, a modified butt-coupling scheme can be used with an inverted tapered section in between the ridge and slot section, the length of which can be optimized (e.g., ~140 nm) to achieve a reasonable coupling efficiency (e.g., >90%) and propagation loss. However, in scenarios where the real estate is more important, a compact coupling scheme such as standard butt-coupling with optimized parameters (e.g. ridge core width ~500 nm, slot rail width ~275 nm, slot gap 50 nm, a zero gap between the ridge and slot section) can be designed for a proper mode match with a moderately increased loss [121]. As an alternative approach, phase matching between a wire and slot mode can also be achieved with the help of a mode transformer to experimentally realize a reasonable coupling efficiency (>90%) [82].

Appendix IV:

Table S2. Performance summary and comparison of the proposed EAM with the state-of-the-art modulators reported in the literature

Device	Modulation (dB)	Insertion Loss (dB)	Energy Consumption (fJ/bit)	Speed (GHz)	Size [µm^2]
$LiNbO_3$-based EOM [4]	30	<1dB	0.37	50	20[mm]
Si Micro Ring Photonic [66]	9	1	1	25	25
Si Travelling Wave Photonic [67]	3	4	N/R	25	~1 x 10^6
Organic Polymer Plasmonic [21]	6	9	25	70	10
Sn:In_2O_3 Plasmonic (ENZ) [17]	10	16	4*	25	200
Au/In_2O_3 Plasmonic (ENZ) [19]	6.5	10	2.1pJ/bit	~2*	4
Graphene-based modulator [68]	3	N/R	N/R	1.2	25
This Research (1-slot)	6	~1.07	1.74 [pJ/bit]	~20	6.3
This Research (4-slot)	6	0.7	1.71[pJ/bit]	~1	6.75

(N/R represents data not reported. *Values that have been estimated)

References

1. G. V. Naik, V. M. Shalaev, and A. Boltasseva, "Alternative plasmonic materials: Beyond gold and silver," Adv. Mater. **25**, 3264–3294 (2013).

2. N. Eti and H. Kurt, "Model analysis of ridge and rib types of silicon waveguides with void compositions," IEEE J. Quantum Electron. **52**, (2016).

3. Q. Cheng, M. Bahadori, M. Glick, S. Rumley, and K. Bergman, "Recent advances in optical technologies for data centers: a review," Optica **5**, 1354 (2018).

4. C. Wang, M. Zhang, X. Chen, M. Bertrand, A. Shams-Ansari, S. Chandrasekhar, P. Winzer, and M. Lončar, "Integrated lithium niobate electro-optic modulators operating at CMOS-compatible voltages," Nature **562**, 101–104 (2018).

5. M. H. Tahersima, Z. Ma, Y. Gui, S. Sun, H. Wang, R. Amin, H. Dalir, R. Chen, M. Miscuglio, and V. J. Sorger, "Coupling-enhanced dual ITO layer electro-absorption modulator in silicon photonics," Nanophotonics **8**, 1559–1566 (2019).

6. M. Zhang, C. Wang, P. Kharel, D. Zhu, and M. Lončar, "Integrated lithium niobate electro-optic modulators: when performance meets scalability," Optica **8**, 652 (2021).

7. R. Amin, J. K. George, S. Sun, T. Ferreira De Lima, A. N. Tait, J. B. Khurgin, M. Miscuglio, B. J. Shastri, P. R. Prucnal, T. El-Ghazawi, and V. J. Sorger, "ITO-based electro-absorption modulator for photonic neural activation function," APL Mater. **7**, 0–11 (2019).

8. Y.-D. Hsieh, J.-H. Lin, R. Soref, G. Sun, H.-H. Cheng, and G.-E. Chang, "Electro-absorption modulation in GeSn alloys for wide-spectrum mid-infrared applications," Commun. Mater. **2**, 1–8 (2021).

9. Q. Gao, E. Li, and A. X. Wang, "Ultra-compact and broadband electro-absorption modulator using an epsilon-near-zero conductive oxide," Photonics Res. **6**, 277 (2018).

10. J. Wang, F. Bo, S. Wan, W. Li, F. Gao, J. Li, G. Zhang, and J. Xu, "High-Q lithium niobate microdisk resonators on a chip for efficient electro-optic modulation," Opt. Express **23**, 23072 (2015).

11. J. D. Witmer, J. A. Valery, P. Arrangoiz-Arriola, C. J. Sarabalis, J. T. Hill, and A. H. Safavi-Naeini, "High-Q photonic resonators and electro-optic coupling using silicon-on-lithium-niobate," Sci. Rep. **7**, 1–7 (2017).

12. Y. Qi and Y. Li, "Integrated lithium niobate photonics," Nanophotonics **9**, 1287–1320 (2020).

13. T. Pan, C. Qiu, J. Wu, X. Jiang, B. Liu, Y. Yang, H. Zhou, R. Soref, and Y. Su, "Analysis of an electro-optic modulator based on a graphene-silicon hybrid 1D photonic crystal nanobeam cavity," Opt. Express **23**, 23357 (2015).

14. B. Hadian Siahkal-Mahalle and K. Abedi, "Ultra-compact low loss electro-optical nanobeam cavity modulator embedded photonic crystal," Opt. Quantum Electron. **51**, 1–15 (2019).

15. X. Li, X. Liu, Y. Qin, D. Yang, and Y. Ji, "Ultra-Low Index-Contrast Polymeric Photonic

Crystal Nanobeam Electro-Optic Modulator," IEEE Photonics J. **12**, (2020).

16. J. A. Dionne, K. Diest, L. A. Sweatlock, and H. A. Atwater, "PlasMOStor: A Metal−Oxide−Si Field Effect Plasmonic Modulator," Nano Lett. **9**, 897–902 (2009).

17. H. W. Lee, G. Papadakis, S. P. Burgos, K. Chander, A. Kriesch, R. Pala, U. Peschel, and H. A. Atwater, "Nanoscale conducting oxide PlasMOStor," Nano Lett. **14**, 6463–6468 (2014).

18. Chenran Ye, S. Khan, Zhuo Ran Li, E. Simsek, and V. J. Sorger, "λ-Size ITO and Graphene-Based Electro-Optic Modulators on SOI," IEEE J. Sel. Top. Quantum Electron. **20**, 40–49 (2014).

19. M. G. Wood, S. Campione, S. Parameswaran, T. S. Luk, J. R. Wendt, D. K. Serkland, and G. A. Keeler, "Gigahertz speed operation of epsilon-near-zero silicon photonic modulators," Optica **5**, 233 (2018).

20. A. Melikyan, L. Alloatti, A. Muslija, D. Hillerkuss, P. C. Schindler, J. Li, R. Palmer, D. Korn, S. Muehlbrandt, D. Van Thourhout, B. Chen, R. Dinu, M. Sommer, C. Koos, M. Kohl, W. Freude, and J. Leuthold, "High-speed plasmonic phase modulators," Nat. Photonics **8**, 229–233 (2014).

21. C. Haffner, W. Heni, Y. Fedoryshyn, J. Niegemann, A. Melikyan, D. L. Elder, B. Baeuerle, Y. Salamin, A. Josten, U. Koch, C. Hoessbacher, F. Ducry, L. Juchli, A. Emboras, D. Hillerkuss, M. Kohl, L. R. Dalton, C. Hafner, and J. Leuthold, "All-plasmonic Mach–Zehnder modulator enabling optical high-speed communication at the

microscale," Nat. Photonics **9**, 525–528 (2015).

22. J. A. Schuller, E. S. Barnard, W. Cai, Y. C. Jun, J. S. White, and M. L. Brongersma, "Plasmonics for extreme light concentration and manipulation," Nat. Mater. **9**, 193–204 (2010).

23. C. Haffner, D. Chelladurai, Y. Fedoryshyn, A. Josten, B. Baeuerle, W. Heni, T. Watanabe, T. Cui, B. Cheng, S. Saha, D. L. Elder, L. R. Dalton, A. Boltasseva, V. M. Shalaev, N. Kinsey, and J. Leuthold, "Low-loss plasmon-assisted electro-optic modulator," Nature **556**, 483–486 (2018).

24. D. A. Neaman, *Semiconductor Physics and Devices Basic Principles*, 4th Ed. (McGraw-Hill, 2012).

25. B. E. N. G. Streetman and S. K. Banerjee, *Solid State Electroninc Devices*, 6th Ed. (PHI Learning Private Limited, 2009).

26. R. F. Pierret, *Semiconductor Device Fundamentals* (1996).

27. K. K. N. S. M. Sze, *Physics of Semiconductor Devices*, 3rd Ed. (Wiley-Interscience, 2007).

28. R. F. Pierret, *Advanced Semiconductor Fundamentals*, 2nd Ed (n.d.), Vol. IV.

29. S. Zhu, T. Y. Liow, G. Q. Lo, and D. L. Kwong, "Fully complementary metal-oxide-semiconductor compatible nanoplasmonic slot waveguides for silicon electronic photonic integrated circuits," Appl. Phys. Lett. **98**, 1–4 (2011).

30. Q. Gao, E. Li, and A. X. Wang, "Comparative analysis of transparent conductive oxide

electro-absorption modulators [Invited]," Opt. Mater. Express **8**, 2850 (2018).

31. M. G. Ancona, "Density-gradient theory: A macroscopic approach to quantum confinement and tunneling in semiconductor devices," J. Comput. Electron. **10**, 65–97 (2011).

32. M. G. Ancona, "Equations of state for silicon inversion layers," IEEE Trans. Electron Devices **47**, 1449–1456 (2000).

33. M. G. Ancona, Z. Yu, R. W. Dutton, and P. J. Vande Voorde, "Density-gradient analysis of MOS tunneling," IEEE Trans. Electron Devices **47**, 2310–2319 (2000).

34. P. Andrei, "Identification technique for the Density-Gradient model," (2015).

35. R. K. and M. O. W. HANSCH, TH. VOGELSANG, "CARRIER TRANSPORT NEAR THE Si/SiO2 INTERFACE OF A MOSFET," **32**, 839–849 (1989).

36. M. Fox, *Optical Properties of Solid* (Oxford University Press, 2001).

37. N. Kinsey and J. Khurgin, "Nonlinear epsilon-near-zero materials explained: opinion," Opt. Mater. Express **9**, 2793 (2019).

38. C. Fruhling, M. G. Ozlu, S. Saha, A. Boltasseva, and V. M. Shalaev, "Understanding all-optical switching at the epsilon-near-zero point: a tutorial review," Appl. Phys. B Lasers Opt. **128**, 1–12 (2022).

39. R. Amin, R. Maiti, C. Carfano, Z. Ma, M. H. Tahersima, Y. Lilach, D. Ratnayake, H. Dalir, and V. J. Sorger, "0.52 v mm ITO-based Mach-Zehnder modulator in silicon photonics," APL Photonics **3**, 0–11 (2018).

40. B. Zhou, E. Li, Y. Bo, and A. X. Wang, "High-Speed Plasmonic-Silicon Modulator Driven by Epsilon-Near-zero Conductive Oxide," J. Light. Technol. **38**, 3338–3345 (2020).

41. R. Secondo, J. Khurgin, and N. Kinsey, "Absorptive loss and band non-parabolicity as a physical origin of large nonlinearity in epsilon-near-zero materials," Opt. Mater. Express **10**, 1545 (2020).

42. N. Kinsey, C. DeVault, A. Boltasseva, and V. M. Shalaev, "Near-zero-index materials for photonics," Nat. Rev. Mater. **4**, 742–760 (2019).

43. J. Wu, Z. T. Xie, Y. Sha, H. Y. Fu, and Q. Li, "Epsilon-near-zero photonics: infinite potentials," Photonics Res. **9**, 1616 (2021).

44. E. Feigenbaum, K. Diest, and H. A. Atwater, "Unity-order index change in transparent conducting oxides at visible frequencies," Nano Lett. **10**, 2111–2116 (2010).

45. A. Ball, J. Wu, D. Fomra, R. Secondo, S. Saha, M. Sojib, J. B. Khurgin, H. J. Lezec, and N. Kinsey, "Tailoring Nonlinearities in Epsilon-Near-Zero Materials via Structure and Excitation," in *Optica Advanced Photonics Congress 2022* (Optica Publishing Group, 2022), p. NoTu3F.2.

46. Z. Ma, Z. Li, K. Liu, C. Ye, and V. J. Sorger, "Indium-Tin-Oxide for High-performance Electro-optic Modulation," Nanophotonics **4**, 198–213 (2015).

47. V. E. Babicheva, A. Boltasseva, and A. V. Lavrinenko, "Transparent conducting oxides for electro-optical plasmonic modulators," Nanophotonics **4**, 165–185 (2015).

48. R. Amin, R. Maiti, Z. Ma, M. Miscuglio, H. Dalir, and V. J. Sorger, "An ITO-based Mach-Zehnder Modulator with Lateral MOS-Capacitor on SOI Platform," in *Frontiers in Optics + Laser Science APS/DLS* (OSA, 2019), p. JW3A.67.

49. K. Liu, C. R. Ye, S. Khan, and V. J. Sorger, "Review and perspective on ultrafast wavelength-size electro-optic modulators," Laser Photonics Rev. **9**, 172–194 (2015).

50. M. C. T. B.E.A. Saleh, *Fundamentals of Photonics* (Wiley Berlin, 2019).

51. G. L. Li, P. K. L. Yu, and I. Tutorial, "Optical Intensity Modulators for Digital and Analog Applications," Lightwave **21**, 2010–2030 (2003).

52. G. Sinatkas, T. Christopoulos, O. Tsilipakos, and E. E. Kriezis, "Electro-optic modulation in integrated photonics," J. Appl. Phys. **130**, (2021).

53. S. Nakano, K. Akiyama, and I. Shoji, "Accurate measurement of electro-optic coefficients of undoped and MgO-doped stoichiometric LiNbO_3," Opt. Mater. Express **7**, 939 (2017).

54. E. L. Wooten, K. M. Kissa, A. Yi-Yan, E. J. Murphy, D. A. Lafaw, P. F. Hallemeier, D. Maack, D. V. Attanasio, D. J. Fritz, G. J. McBrien, and D. E. Bossi, "Review of lithium niobate modulators for fiber-optic communications systems," IEEE J. Sel. Top. Quantum Electron. **6**, 69–82 (2000).

55. R. W. Boyd, *Nonlinear Optics, 3rd Ed. Ch11* (2008).

56. A. Liu, L. Liao, D. Rubin, H. Nguyen, B. Ciftcioglu, Y. Chetrit, N. Izhaky, and M. Paniccia, "High-speed optical modulation based on carrier depletion in a silicon waveguide," Opt. Express **15**, 660 (2007).

57. E. Timurdogan, C. M. Sorace-Agaskar, J. Sun, E. Shah Hosseini, A. Biberman, and M. R. Watts, "An ultralow power athermal silicon modulator," Nat. Commun. **5**, (2014).

58. G. T. Reed, G. Mashanovich, F. Y. Gardes, and D. J. Thomson, "Silicon optical modulators," Nat. Photonics **4**, 518–526 (2010).

59. D. Chauhan, Z. Sbeah, R. P. Dwivedi, J. M. Nunzi, and M. S. Thakur, "An investigation and analysis of plasmonic modulators: A review," J. Opt. Commun. 1–29 (2022).

60. J. I. Pankove and D. A. Kiewit, *Optical Processes in Semiconductors* (2010).

61. K. Nozaki, A. Shakoor, S. Matsuo, T. Fujii, K. Takeda, A. Shinya, E. Kuramochi, and M. Notomi, "Ultralow-energy electro-absorption modulator consisting of InGaAsP-embedded photonic-crystal waveguide," APL Photonics **2**, (2017).

62. L. Wu, Y. Zhou, Y. Cai, X. Cao, R. Wang, M. Qi, J. Fong, D. Feng, and A. Wu, " Design of a broadband Ge 1−x Si x electro-absorption modulator based on the Franz-Keldysh effect with thermal tuning ," Opt. Express **28**, 7585 (2020).

63. K. J. Miller, R. F. Haglund, and S. M. Weiss, "Optical phase change materials in integrated silicon photonic devices: review," Opt. Mater. Express **8**, 2415 (2018).

64. G. Sinatkas, A. Pitilakis, D. C. Zografopoulos, R. Beccherelli, and E. E. Kriezis, "Transparent conducting oxide electro-optic modulators on silicon platforms: A comprehensive study based on the drift-diffusion semiconductor model," J. Appl. Phys. **121**, (2017).

65. M. Sojib, D. Fomra, V. Avrutin, Ü. Özgür, and N. Kinsey, "Optimizing epsilon-near-zero

based plasmon assisted modulators through surface-to-volume ratio," Opt. Express **30**, 19781 (2022).

66. Q. Xu, B. Schmidt, S. Pradhan, and M. Lipson, "Micrometre-scale silicon electro-optic modulator," Nature **435**, 325–327 (2005).

67. D. M. Gill, W. M. J. Green, C. Xiong, A. Rylyakov, C. Schow, J. Proesel, J. C. Rosenberg, T. Barwicz, M. Khater, S. Assefa, S. M. Shank, C. Reinholm, E. Kiewra, S. Kamlapurkar, and Y. A. Vlasov, "Distributed electrode Mach-Zehnder modulator with double-pass phase shifters and integrated inductors," Opt. Express **23**, 16857 (2015).

68. M. Liu, X. Yin, E. Ulin-Avila, B. Geng, T. Zentgraf, L. Ju, F. Wang, and X. Zhang, "A graphene-based broadband optical modulator," Nature **474**, 64–67 (2011).

69. E. Hecht, *Optics* (Pearson, 2017).

70. P. Steglich, "Silicon-on-Insulator Slot Waveguides: Theory and Applications in Electro-Optics and Optical Sensing," Emerg. Waveguide Technol. (2018).

71. R. Yusof, N. Ali, P. Kolenderski, K. Slowik, and N. A. M. Ahmad Hambali, "Comparative Studies of Rib Waveguide Material for Quantum Communication Application," IOP Conf. Ser. Mater. Sci. Eng. **551**, (2019).

72. N. M. Kassim, A. B. Mohammad, A. S. M. Supa'at, M. H. Ibrahim, and S. Y. Gang, "Single mode rib optical waveguide modeling techniques," 2004 RF Microw. Conf. RFM 2004 - Proc. 272–276 (2004).

73. Kenji Kawano and Tsutomu Kitoh, *INTRODUCTION TO OPTICAL WAVEGUIDE*

ANALYSIS Solving Maxwell ' s Equations and the Schrodinger Equation (John Wiley & Sons, Ltd, 2001), Vol. 1.

74. M. Sojib, D. Fomra, V. Avrutin, and N. Kinsey, "Surface to Volume Ratio as a Design Principle for ENZ-based Plasmon Assisted Electro-Optic Modulators," in *Frontiers in Optics + Laser Science 2021* (Optica Publishing Group, 2021), p. JTh5A.22.

75. T. Kim, C. Oh, S. H. Park, J. W. Lee, S. I. Lee, and B. S. Kim, "Electrical properties of low-temperature SiO2thin films prepared by plasma-enhanced atomic layer deposition with different plasma times," AIP Adv. **11**, (2021).

76. M. J. , Jesse Judd, "Fabrication and Characterization of High-k Al2O3 and HfO2 Capacitors," in *36th Annual Microelectronic Engineering Conference, April 2018* (2018), pp. 1–5.

77. G. D. Wilk, R. M. Wallace, and J. M. Anthony, "High-κ gate dielectrics: Current status and materials properties considerations," J. Appl. Phys. **89**, 5243–5275 (2001).

78. M. Kopani, M. Mikula, E. Pinčík, H. Kobayashi, and M. Takahashi, "FT IR spectroscopy of nitric acid oxidation of silicon with hafnium oxide very thin layer," Appl. Surf. Sci. **301**, 24–27 (2014).

79. X. Nie, F. Ma, D. Ma, and K. Xu, "Growth mode evolution of hafnium oxide by atomic layer deposition," J. Vac. Sci. Technol. A Vacuum, Surfaces, Film. **32**, 01A109 (2014).

80. U. Koch, C. Hoessbacher, J. Niegemann, C. Hafner, and J. Leuthold, "Digital Plasmonic Absorption Modulator Exploiting Epsilon-Near-Zero in Transparent Conducting Oxides,"

IEEE Photonics J. **8**, 1–13 (2016).

81. P. Seidler, "Optimized process for fabrication of free-standing silicon nanophotonic devices," J. Vac. Sci. Technol. B, Nanotechnol. Microelectron. Mater. Process. Meas. Phenom. **35**, 031209 (2017).

82. V. Mere, R. Kallega, and S. K. Selvaraja, "Efficient and tunable strip-to-slot fundamental mode coupling," Opt. Express **26**, 438 (2018).

83. A. Aray and S. Ghavami Sabouri, "Plasmonic Bragg microcavity as an efficient electro-optic modulator," Opt. Express **28**, 20523 (2020).

84. J. Baek, J.-B. You, and K. Yu, "Free-carrier electro-refraction modulation based on a silicon slot waveguide with ITO," Opt. Express **23**, 15863 (2015).

85. H. Shu, B. Shen, Q. Deng, M. Jin, X. Wang, and Z. Zhou, "A Design Guideline for Mode (DE) Multiplexer Based on Integrated Tapered Asymmetric Directional Coupler," IEEE Photonics J. **11**, 1 (2019).

86. J. W. Elam, D. A. Baker, A. B. F. Martinson, M. J. Pellin, and J. T. Hupp, "Atomic Layer Deposition of Indium Tin Oxide Thin Films Using Nonhalogenated Precursors," J. Phys. Chem. C **112**, 1938–1945 (2008).

87. R. Amin, J. B. Khurgin, and V. J. Sorger, "Waveguide-based electro-absorption modulator performance: comparative analysis," Opt. Express **26**, 15445 (2018).

88. B. C. Mallick, C.-T. Hsieh, K.-M. Yin, Y. A. Gandomi, and K.-T. Huang, "Review—On Atomic Layer Deposition: Current Progress and Future Challenges," ECS J. Solid State

Sci. Technol. **8**, N55–N78 (2019).

89. S. M. George, "Atomic layer deposition: An overview," Chem. Rev. **110**, 111–131 (2010).

90. "Fiji G2 PE-ALD User's Manual," (2015).

91. R. W. Johnson, A. Hultqvist, and S. F. Bent, "A brief review of atomic layer deposition: From fundamentals to applications," Mater. Today **17**, 236–246 (2014).

92. H. H. Sønsteby, A. Yanguas-Gil, and J. W. Elam, "Consistency and reproducibility in atomic layer deposition," J. Vac. Sci. Technol. A **38**, 020804 (2020).

93. L. A. Dobrzański, M. Szindler, and M. M. Szindler, "Surface morphology and optical properties of Al2O3 thin films deposited by ALD method," Arch. Mater. Sci. Eng. **73**, 18–24 (2015).

94. D. Fomra, K. Ding, V. Avrutin, Ü. Özgür, and N. Kinsey, "Al:ZnO as a platform for near-zero-index photonics: enhancing the doping efficiency of atomic layer deposition," Opt. Mater. Express **10**, 3060 (2020).

95. J. A. Woollam, "Easy-to-Use Acquisition / Analysis Software for Spectroscopic Ellipsometry," (n.d.).

96. J. A. Woollam, B. D. Johs, C. M. Herzinger, J. N. Hilfiker, R. A. Synowicki, and C. L. Bungay, "Overview of variable-angle spectroscopic ellipsometry (VASE): I. Basic theory and typical applications," Opt. Metrol. A Crit. Rev. **10294**, 1029402 (1999).

97. B. Johs and J. S. Hale, "Dielectric function representation by B-splines," Phys. Status Solidi Appl. Mater. Sci. **205**, 715–719 (2008).

98. R. Secondo, D. Fomra, N. Izyumskaya, V. Avrutin, J. N. Hilfiker, A. Martin, Ü. Özgür, and N. Kinsey, "Reliable modeling of ultrathin alternative plasmonic materials using spectroscopic ellipsometry [Invited]," Opt. Mater. Express **9**, 760 (2019).

99. M. M. Rahman, J. G. Kim, D. H. Kim, and T. W. Kim, "Characterization of Al incorporation into HfO2 dielectric by atomic layer deposition," Micromachines **10**, 1–11 (2019).

100. B. Lu, H. Lv, Y. Zhang, Y. Zhang, and C. Liu, "Comparison of HfAlO, HfO2/Al2O3, and HfO2 on n-type GaAs using atomic layer deposition," Superlattices Microstruct. **99**, 54–57 (2016).

101. X. Liu, S. Ramanathan, A. Longdergan, A. Srivastava, E. Lee, T. E. Seidel, J. T. Barton, D. Pang, and R. G. Gordon, "ALD of Hafnium Oxide Thin Films from Tetrakis(ethylmethylamino)hafnium and Ozone," J. Electrochem. Soc. **152**, G213 (2005).

102. Z. Gao and P. Banerjee, "Review Article: Atomic layer deposition of doped ZnO films," J. Vac. Sci. Technol. A **37**, 050802 (2019).

103. E. Engblom, "Effect of oxygen concentration in build chamber during laser metal deposition of Ti-64 wire," Degree Proj. Mater. Des. Eng. (2018).

104. I. I. Kornilov, "Effect of oxygen on titanium and its alloys," Met. Sci. Heat Treat. **15**, 826–829 (1973).

105. J. Graciani, J. Fdez Sanz, T. Asaki, K. Nakamura, and J. A. Rodriguez, "Interaction of oxygen with TiN (001): N↔O exchange and oxidation process," J. Chem. Phys. **126**,

(2007).

106. D. Fomra, R. Secondo, K. Ding, V. Avrutin, N. Izyumskaya, Ü. Özgür, and N. Kinsey, "Plasmonic titanium nitride via atomic layer deposition: A low-temperature route," J. Appl. Phys. **127**, (2020).

107. F. S. Oliveira, R. B. Cipriano, F. T. da Silva, E. C. Romão, and C. A. M. dos Santos, "Simple analytical method for determining electrical resistivity and sheet resistance using the van der Pauw procedure," Sci. Rep. **10**, 1–8 (2020).

108. N. Ngo, H. Niu, P. Bharadwaj, H. Bhatti, and S. Adhikari, "Van der Pauw Resistivity Measurement," 3–6 (2017).

109. J. B. Khurgin, V. J. Sorger, and R. Amin, "Charge and field driven integrated optical modulators: comparative analysis: opinion," Opt. Mater. Express **12**, 1784 (2022).

110. S. Zhu, G. Q. Lo, and D. L. Kwong, "Design of an ultra-compact electro-absorption modulator comprised of a deposited TiN/HfO_2/ITO/Cu stack for CMOS backend integration," Opt. Express **22**, 17930 (2014).

111. Y. Sha, J. Wu, Z. T. Xie, H. Y. Fu, and Q. Li, "Comparison Study of Multi-Slot Designs in Epsilon-Near-Zero Waveguide-Based Electro-Optical Modulators," IEEE Photonics J. **13**, (2021).

112. G. W. Lu, J. Hong, F. Qiu, A. M. Spring, T. Kashino, J. Oshima, M. aki Ozawa, H. Nawata, and S. Yokoyama, "High-temperature-resistant silicon-polymer hybrid modulator operating at up to 200 Gbit s−1 for energy-efficient datacentres and harsh-environment

applications," Nat. Commun. **11**, 1–9 (2020).

113. F. E. Rougieux, D. MacDonald, A. Cuevas, S. Ruffell, J. Schmidt, B. Lim, and A. P. Knights, "Electron and hole mobility reduction and Hall factor in phosphorus-compensated p -type silicon," J. Appl. Phys. **108**, (2010).

114. J. W. Cleary, E. M. Smith, K. D. Leedy, G. Grzybowski, and J. Guo, "Optical and electrical properties of ultra-thin indium tin oxide nanofilms on silicon for infrared photonics," Opt. Mater. Express **8**, 1231 (2018).

115. N. Zhou, J. Li, H. Radamson, L. Li, Q. Jiang, and J. Li, "Deep silicon etching for thermopile structures using a modified Bosch process," J. Micro/Nanolithography, MEMS, MOEMS **18**, 1 (2019).

116. Saint-Gobain, "PDS Products Boron Nitride Product Applications," (n.d.).

117. M. Balasubramanian, L. K. Bera, S. Mathew, N. Balasubramanian, V. Lim, M. S. Joo, and B. J. Cho, "Wet etching characteristics and surface morphology evaluation of MOCVD grown HfO2 film," Thin Solid Films **462–463**, 101–105 (2004).

118. S.-C. Han, J. Y. Kim, J.-K. Kim, Y. J. Jo, J.-S. Kwak, and J.-M. Lee, " Wet-Chemical Etching of IGZO and HfO 2 ," ECS Meet. Abstr. **MA2009-02**, 1929–1929 (2009).

119. T. Nishimura, R. Kuse, K. Tominaga, T. Nabatame, and A. Toriumi, "Wet Etching Characteristics of both As-deposited and Annealed Al2O3 and HfAlOx Films," in *Extended Abstracts of the 2003 International Conference on Solid State Devices and Materials* (The Japan Society of Applied Physics, 2003), pp. 516–517.

120. S.-H. Su, H.-J. Kong, C.-L. Tseng, and G.-Y. Chen, "Wet etching mechanism and crystallization of indium–tin oxide layer for application in light-emitting diodes," Jpn. J. Appl. Phys. **57**, 01AE05 (2018).

121. M. A. Butt, S. N. Khonina, and N. L. Kazanskiy, "Ultrashort inverted tapered silicon ridge-to-slot waveguide coupler at 155 µm and 3392 µm wavelength," Appl. Opt. **59**, 7821 (2020).

Publications

Journal

M. Sojib, Dhruv Fomra, V. Avrutin. U. Ozgur, Nathaniel Kinsey "Optimizing epsilon-near-zero based Plasmon Assisted Modulators Through Surface to Volume Ratio" (Published in Optics Express 2022)

Conferences

- N. Kinsey, A. Ball, D. Fomra, R. Secondo, J. Wu, M. Sojib, S. Saha, V. Avrutin. U. Ozgur, "Nonlinearities when the index vanishes," SPIE Optics & Photonics, San Diego CA, 2022. [Invited]
- D. Fomra A. Ball, J. Wu, R. Secondo, S. Saha, M. Sojib, J. B. Khurgin, H. J. Lezec, and N. Kinsey, "Engineering Extrinsic Nonlinearities in Epsilon-Near-Zero Materials via Surface Lattice Resonance," META 2022, Torremolinos Spain, July 2022. [Invited]
- A. Ball, J. Wu, D. Fomra, R. Secondo, S. Saha, M. Sojib, J. B. Khurgin, H. J. Lezec, and N. Kinsey, "Tailoring Nonlinearities in Epsilon-Near-Zero Materials via Structure and Excitation," Optica Advanced Photonics Congress, Maastricht Netherlands, July 2022. [Invited]
- M. Sojib, Dhruv Fomra, Vitaliy Avrutin, Nathaniel Kinsey "Surface to Volume Ratio as a Design Principle for ENZ-based Plasmon Assisted Electro-Optic Modulators", FiO + LS, OSA, 2021.

- N. Kinsey, D. Fomra, K. Ding, M. Sojib, S. Saha, R. Secondo, A. Ball, V. Avrutin, and Ü. Özgür, "Advancing Functional Materials for Robust and Dynamic Nanophotonics" *MRS Spring Meeting*, Virtual Conference, 2021. [Invited]

Patent

- N. Kinsey, D. Fomra, M. Sojib, V. Avrutin, and Ü. Özgür, "Plasmon Assisted Design Philosophy for Electro-Optics Modulators", Provisional Application no. 63/311,194, Filed Feb. 17, 2022 (Approved).

List of Major Abbreviations

ALD: Atomic Layer Deposition

AZO: Aluminum-doped Zinc Oxide

BBO: Beta Barium Borate

BOE: Buffer Oxide Etch

BSG: Boro-Silicate-Glass

CB and VB: Conduction and Valence Band

CMOS: Complementary Metal Oxide Semiconductor

CVD: Chemical Vapor Deposition

DD, DG: Drift-Diffusion, Density Gradient

DEZ: Diethyl Zinc

DI: De-ionized

EBD: Energy Band Diagram

EOM/EAM: Electro-optic/absorption Modulator

EM: Electro-magnetic

ENZ: Epsilon Near Zero

EOT: Effective Oxide Thickness

ER or MD: Extinction Ratio or Modulation Depth

FEM, FOM: Finite Element Method,: Figure of Merit

fs: femtosecond

Gen-Osc: General Oscillator

GHz: Giga-Hertz

GPC: Growth Per Cycle

IL: Insertion Loss (off-state loss)

IPA: Iso-Propyl-Alcohol

ITO: Indium Tin Oxide

KTP: Potassium Titanyl Phosphate

LED: Light-Emitting Diode

LMI: Light-Matter-Interaction

LT/HT: Low or High transmission

MIS/MOS: Metal-Insulator/Oxide Semiconductor

MIM: Metal-Insulator-Metal

MSE: Mean Square Error

MZI: Mach Zehnder Interferometer

NIR and Mid IR: Near Infra-red and Mid Infra-red

PIC: Photonic Integrated Circuit

pJ/fJ: pico-joule/femto-joule

PL: Propagation Loss

SE: Spectroscopic Ellipsometry

SOI: Si on Insulator

SP: Schrödinger-Poisson

SVR: Surface-to-Volume Ratio

TCO: Transparent Conducting Oxide

TDMAT: Tetrakis (dimethyl-amido) titanium (IV)

TE/TM: Tranverse Electric/Magnetic

TEMAH: Tetrakis (ethylmethylamido) hafnium (IV)

TIR: Total Internal Reflection

TMA: Tri-Methyl-Aluminum

List of Variables and Constants

Symbol	Name	Symbol	Name
A	Capacitor area	n_{eff}	Effective mode index
b_n and b_p	DG coefficients for electron and hole	n	Refractive index
C	Capacitance	n, n_i	Electron or intrinsic carrier concentration
d	Oxide thickness	N_C	Conduction band effective density of states
D	Electric field displacement	N_V	Valence band effective density of states
E	Energy/Electric Field	p, p	Dipole moment, Hole concentration
E_C, E_V	Conduction or Valence band Energy	R	Resistance
E_i	Mid gap energy	$\tilde{r}_p, \tilde{r}_s$	Complex Fresnel reflection coefficient
E_g, E_F	Material band gap, Fermi level	T	Temperature
e, q	Electron charge	$t_{A\text{-}Chem}$	Chemisorption time for precursor A
α	Mode or propagation loss	W_{Slot}	Slot width
$f(E)$	Fermi function	χ	Electron affinity/Susceptibility
$g_c(E)$	Conduction band density of states	Φ_m	Working function
$g_v(E)$	Valence band density of states	δ_P, δ_s	Phase of p and s polarized light
H	Magnetic field	Ψ, Δ	SE experimental data
J_n or J_p	Electron or hole current density	λ	Wavelength
k	Oxide dielectric constant	V	Potential
K_B, K	Boltzmann Constant, Momentum vector	Ɛ, γ	Permittivity, Damping frequency
m^*, m^*_{DG}	Electron or DG effective mass	ρ	Charge density
m_0	Free electron mass	ε_r, ε_∞	Relative or high frequency permittivity
N	Electron Concentration	Ω, ω_p	Angular frequency, Plasma frequency
N_d, N_a	Donor or Acceptor concentration	Β, μ	Propagation constant, Carrier mobility

Vitae

Mohammad Ariful Hoque Sojib was born in October 1989 in Chattogram, the largest port city of Bangladesh. He selected science and passed Secondary School Certificate (SSC) and Higher Secondary Certificate (HSC) public examination in the year 2005 and 2007 respectively. He graduated with a Bachelor of Science in Electrical and Electronic Engineering (EEE) from Chittagong University of Engineering and Technology (CUET) in November 2012. He was a lecturer in Prime University from March 2013 to June 2013 and in Daffodil International University from June 2013 to August 2015. He worked as an Assistant Engineer in Power Grid Company of Bangladesh (PGCB) from September 2015 to December 2018. He is going to graduate with a Master of Science in Electrical and Computer Engineering (ECE) from Virginia Commonwealth University (VCU) in December 2022.